Emergent phenomena and device applications in magnetic van der Waals heterostructures

Tiancheng Song

A dissertation

submitted in partial fulfillment of the

requirements for the degree of

Doctor of Philosophy

University of Washington

2021

Reading Committee:

Xiaodong Xu, Chair

David Cobden

Jiun-Haw Chu

Program Authorized to Offer Degree:

Department of Physics

University of Washington

Abstract

Emergent phenomena and device applications in magnetic van der Waals heterostructures

Tiancheng Song

Chair of the Supervisory Committee:
Professor Xiaodong Xu
Department of Physics

Van der Waals (vdW) heterostructures built by the vertical stacking of various 2D materials provide an ideal platform for the rational design of emergent phenomena and device applications. The recent discovery of atomically thin magnetic vdW materials has created new opportunities to explore 2D magnetism in magnetic vdW heterostructures. In this thesis, we will present an exploration into the 2D magnet chromium triiodide (CrI_3) and its vdW heterostructures. We will first introduce the unique layer-dependent magnetism in CrI_3 enabled by the antiferromagnetic interlayer coupling. We then achieve giant tunneling magnetoresistance by using CrI_3 as a tunnel barrier in vdW spin-filter magnetic tunnel junctions. In a dual-gated structure, a pair of bistable magnetic states in four-layer CrI_3 can be switched reversibly by electrostatic gating, demonstrating a new kind of voltage-controlled vdW spintronic device. We will also unravel the stacking-dependent magnetism in CrI_3, and realize the control of interlayer magnetism and switching of

magnetic states via pressure tunning of layer stacking. Finally, we will discuss the helicity-dependent photocurrent in CrI_3 and its interplay with the underlying exciton states and magnetic order.

TABLE OF CONTENTS

LIST OF FIGURES

ABBREVIATIONS

2D – Two-dimensional

TMD – Transition metal dichalcogenides

hBN – Hexagonal boron nitride

CrI_3 – Chromium triiodide

vdW – van der Waals

BZ – Brillouin Zone

CBM – Conduction band minimum

VBM – Valence band maximum

FM – Ferromagnetic

AFM – Antiferromagnetic

PDMS – Poly-dimethylsiloxane

PC – Polycarbonate

IPA – Isopropyl alcohol

PMMA – Poly (methyl methacrylate)

CCD – Charge-coupled device

EBL – Electron beam lithography

PL – Photoluminescence

SHG – Second harmonic generation

MCB – Magnetic circular birefringence

MCD – Magnetic circular dichroism

RCP – Right-circularly polarized

LCP – Left-circularly polarized

MOKE – Magneto-optical Kerr effect

RMCD – Reflective magnetic circular dichroism

ACKNOWLEDGEMENTS

First, I want to express my sincere gratitude to my advisor, Prof. Xiaodong Xu, who has guided my research over the past five years. I still remember, as a senior undergraduate, struggling to decide which university to go to and which subject to focus on during my Ph.D. After thinking it through for several weeks, I made a decision I will never regret, and still remember the excitement of that day. As my advisor, Xiaodong has always been extraordinarily encouraging, supportive, responsive during each stage of research, which shaped me into a researcher. I have learned a lot from his rigorous approach, super-efficient way of working, and great research enthusiasm for research.

I would like to thank Prof. David Cobden and Prof. Jiun-Haw Chu as my reading committee members. Dave has been very supportive over the past five years. I have really enjoyed the time I spent in his lab using the instruments and discussing physics with him and his great students. Jiun-Haw is always so nice and friendly, and provides us with a great variety of crystals crucial to our work. Dave and Jiun-Haw both have excellent taste in science and sharp intuition in physics, and I can always learn a lot through discussion with them. I would also like to express gratitude to my supervisory committee, Prof. Xiaosong Li, Prof. Anton Andreev, Prof. Silas Bean, and Prof. Subhadeep Gupta. I really enjoyed and learned a lot from the great first-year course courses and the insightful discussions about my research.

I would like to thank all the collaborators who have contributed to the work in this dissertation. Without their incredible efforts, this dissertation would not have been possible. Prof. Di Xiao, Prof. Wang Yao, Prof. Ting Cao, and their teams have always been the theoretical

backbone of my research. They have brilliant ideas and natural explanations to communicate the science clearly. All of these research projects would be impossible without the high-quality crystals provided by Dr. Michael A. McGuire, Dr. Kenji Watanabe, and Dr. Takashi Taniguchi. I also want to thank David Graf for his generous help and support during the experiments in MagLab.

I thank all the Xu group members, past and present, for creating an excellent research environment in the lab. I really appreciate all the help and suggestions every time I was struggling with an experiment. For the first half of my Ph.D., I thank Xinghan Cai, Kyle Seyler, Pasqual Rivera, Gen Clark, Ding Zhong, Bevin Huang, Nathan Wilson, Chenfeng Du, Colin Chow, Chang-Hua Liu for welcoming me into the lab, helping me get started and preserve over the years. I want to especially thank Xinghan for being my mentor, teaching me how to do fabrication and measurements, and also helping me finish my first research project. For the second half of my Ph.D., I thank Zaiyao Fei, Qi Zhang, Dmitry Ovchinnikov, Zhong Lin, Xi Wang, Yingqi Wang, Geoffrey Diederich, Minhao He, John Cenker, Kyle Hwangbo, Eric Anderson, Jiaqi Cai, Jiayi Zhu, Yinong Zhang, Jordan Fonseca, Heonjoon Park, Will Holtzmann, Junbo Han, Fucai Liu, Cheng Zhang for helping me finally get here. I want to especially thank Zaiyao for working together with me on the high-pressure experiment and during so many trips to MagLab. I also want to especially thank Eric for working so closely with me, and it has been always an enjoyable collaboration.

I thank all my friends in Seattle. I enjoy playing badminton, hiking, biking, running, and all the parties with tabletop games and cats. I am glad to have met all of you, and my life in Seattle would not be so happy without the good times we shared.

Lastly, words cannot express my gratitude to my parents and girlfriend, Yinqiu, for their love and support.

DEDICATION

To my family.

Chapter 1. INTRODUCTION

1.1 TWO-DIMENSIONAL MATERIALS

The discovery of graphene has launched a new era of condensed matter physics and materials science, providing a unique platform to explore emergent phenomena and engineer device applications based on two-dimensional (2D) materials and their van der Waals (vdW) heterostructures. Graphene as the first isolated 2D material is a single layer of carbon atoms arranged into a 2D honeycomb lattice. It can be simply produced by nothing more than ordinary office supplies, pencil lead, and adhesive tape[1]. This technique is commonly known as the "Scotch tape method", where a piece of adhesive tape is used to peel graphene flakes off of a chunk of graphite – widely used as the lead in pencils, which is essentially a stack of graphene sheets bonded together by vdW forces (Fig. 1.1a-c). The exfoliated monolayer graphene exhibits unique electronic properties and also high quality[2], which can host massless Dirac fermions, and led to emergent phenomena, such as the integer and fractional quantum Hall effects in monolayer graphene[3–5].

Stimulated by the first isolation of monolayer graphene, researchers have been paying growing attention to the search for other 2D materials, which can potentially host new physics and cover the device functionalities. Luckily, the "Scotch tape method" as a mechanical exfoliation approach, is not only limited to graphite but generally applicable to all the vdW materials, which are formed by layers of covalently bonded atoms that are weakly held together by vdW forces. Consequently, the family of 2D materials has been growing rapidly in the past decade, covering a wide range of electronic and optical properties (Fig. 1.1d). In addition to 2D metals and semi-metals, transition metal dichalcogenides (TMDs), as an example of 2D semiconductors, have a

direct bandgap in the visible range in their monolayer form[6,7]. Monolayer TMDs also exhibit strong excitonic effects, strong light-matter interactions, and spin- and valley-dependent properties, which make them an ideal platform to develop 2D optoelectronic applications and explore spin-valley coupled physics[8–10]. Hexagonal boron nitride (hBN) as an insulator has been commonly used for encapsulation to avoid degradation and make high-quality devices[11,12]. The recent additions to the family of 2D materials can host emergent electronic phenomena, for example, superconductivity in $NbSe_2$ and monolayer WTe_2[13–15], charge density waves in TaS_2[16], the quantum spin Hall effect in monolayer WTe_2[17–19], and ferroelectricity in few-layer WTe_2[20]. 2D materials with long-range magnetic order have also been discovered recently, and uniquely enabled the study of emergent phenomena and device applications in magnetic vdW heterostructures, which will be the focus of this thesis.

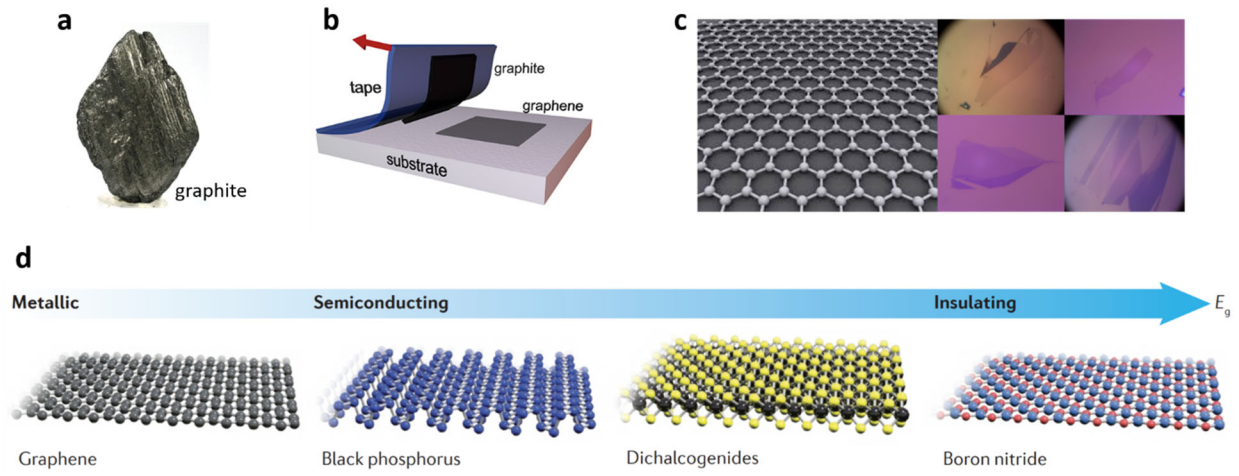

Figure 1.1. Two-dimensional materials. (**a**) Graphite bulk crystal. (**b**) The "Scotch tape method". (**c**) Crystal structure of monolayer graphene and optical microscope images of typical exfoliated graphene flakes on SiO_2/Si substrate. (**d**) A few examples of two-dimensional materials with an increasing bandgap from left to right. Reproduced from reference[21] with permission.

1.2 VAN DER WAALS HETEROSTRUCTURES

In addition to an increasingly diverse "toolbox" of 2D materials, advanced nanofabrication techniques have been developed to vertically assemble different 2D materials into van der Waals heterostructures with atomically sharp interfaces[22,23]. The basic principle is very simple: pick up a monolayer flake, put it on top of another monolayer or few-layer flake, add another 2D flake, and so on, where the constituent layers are held together by vdW forces (Fig. 1.2a). The resulting van der Waals heterostructures have provided an ideal platform for the rational design of emergent phenomena and device applications, mainly thanks to three great advantages.

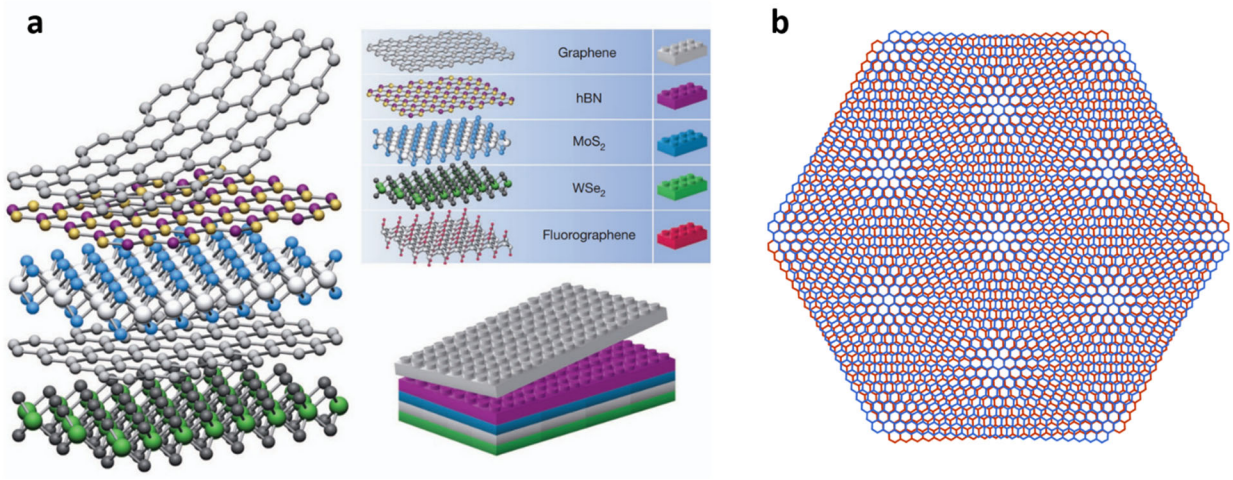

Figure 1.2. Van der Waals heterostructures. (**a**) Assembly of different 2D materials where the constituent layers are held together by van der Waals forces. The resulting van der Waals heterostructure is analogous to the building of LEGO blocks. (**b**) Moiré superlattice of magic-angle twisted bilayer graphene. Reproduced from reference[22] with permission.

The first is that this technique of mechanically assembled stacks can be generally applicable to all the vdW materials, and creates atomically sharp interfaces without the need for lattice matching. As a result, the unique properties of the constituent materials can be combined into a single system for engineering interfaces, exploring proximity effects, and also improving

device quality. The second is that the nanofabrication of multilayer structures facilitates complex but feasible device geometries in vdW heterostructures for diverse electrical and optical measurements. For example, dual gate geometry enables independent control over the doping and electric field of the system, and nanometer-scale transport channels can be well defined by local electrostatic gating. The third is that moiré superlattices can be created by stacking two 2D materials together when there is a relative twist or a mismatched lattice constant (Fig. 1.2b). As an example of heterobilayers, the moiré superlattices can be formed by aligning graphene and hBN, which have led to the observation of Hofstadter's butterfly and the fractal quantum Hall effect[24–26]. More recently, the moiré superlattice of magic-angle twisted bilayer graphene, as an example of homobilayers, was discovered to host exotic strongly correlated phenomena, including superconductivity and correlated insulator states[27,28].

1.3 THESIS OUTLINE

In this thesis, we will explore emergent phenomena and device applications in magnetic van der Waals heterostructures. Our focus is on the 2D magnet chromium triiodide (CrI_3) and its vdW heterostructures. The contents will include 2D magnetism, giant tunneling magnetoresistance effect, electrical control and pressure tunning of 2D magnetism, and spin photovoltaic effect.

In Chapter 2, we will investigate magnetism in 2D magnetic materials. We will first introduce the basic properties of 2D magnet CrI_3 and also discuss the magneto-optic effects we employed as an optical probe to study 2D magnetism, which are magneto-optical Kerr effect and magnetic circular dichroism. We will then demonstrate the first 2D ferromagnetism in monolayer CrI_3, and the unique layered antiferromagnetism in few-layer CrI_3.

In Chapter 3, we will explore the giant tunneling magnetoresistance effect in vdW spin-filter magnetic tunnel junctions. We will first introduce the tunneling magnetoresistance effect in

conventional magnetic tunnel junctions, and discuss the double spin-filtering effect in spin-filter magnetic tunnel junctions. We will then demonstrate tunneling magnetoresistance by using bilayer CrI_3 as a tunnel barrier, which can be dramatically enhanced with increasing CrI_3 layer thickness. We will also present that a pair of bistable magnetic states in four-layer CrI_3 can be switched reversibly by electrostatic gating in a dual-gated structure, demonstrating a new kind of voltage-controlled vdW spintronic devices.

In Chapter 4, we will realize the pressure control of interlayer magnetism in atomically thin CrI_3. We will first discuss the crystal structure of CrI_3 with a focus on layer stacking, and consider the stacking-dependent magnetism. We will then demonstrate the pressure control of interlayer magnetism in bilayer CrI_3, and present the switching of magnetic states via pressure tuning of layer stacking. We will also investigate the coexisting domains of magnetic and layer stacking phases in trilayer CrI_3.

In Chapter 5, we will investigate the spin photovoltaic effect in magnetic vdW heterostructures. We will first introduce the photocurrent response of CrI_3 junction devices, and present the dependence of photocurrent on magnetic states in CrI_3. We will then report the helicity dependence of photocurrent, and discuss the interplay between magnetic order and photon helicity in absorption and photocurrent, demonstrating a proof-of-concept spin-optoelectronics device by engineering magnetic vdW heterostructures.

Chapter 2. MAGNETISM IN TWO-DIMENSIONAL MAGNETIC MATERIALS

In Chapter 2, we will investigate magnetism in 2D magnetic materials. We will first introduce the basic properties of 2D magnet CrI_3 and also discuss the magneto-optic effects we employed as an optical probe to study 2D magnetism, which are magneto-optical Kerr effect and magnetic circular dichroism. We will then demonstrate the first 2D ferromagnetism in monolayer CrI_3, and the unique layered antiferromagnetism in few-layer CrI_3.

2.1 2D MAGNET CHROMIUM TRIIODIDE

Stimulated by the discovery of monolayer graphene, researchers have greatly expanded the "toolbox" of 2D materials, which now covers almost all the functionalities. However, 2D materials with long-range magnetic order, i.e., 2D magnets, were discovered only recently[29,30]. The main challenge is that long-range magnetic order cannot be stabilized in the 2D isotropic Heisenberg model at finite temperatures, due to the enhanced fluctuations in two dimensions, according to the Mermin-Wagner theorem[31]. However, this restriction can be lifted by breaking continuous rotational symmetries through the introduction of magnetic anisotropy. As a result, if a 2D material exhibits strong enough magnetic anisotropy, long-range magnetic order can be stabilized even down to the monolayer limit, which is similar to the presence of magnetic order in the 2D Ising model[32–36].

One promising candidate is 2D material chromium triiodide (CrI_3), which has a strong magnetic anisotropy in the out-of-plane direction, and its bulk crystals already show ferromagnetism below a Curie temperature of 61 K[37]. Figure 2.1a shows the side and top views of the crystal structure of monolayer CrI_3. In the upper panel, the purple and brown atoms represent

the Cr and I atoms, respectively. The Cr^{3+} ions are coordinated to six I^- ions to form edge-sharing octahedra arranged in a hexagonal honeycomb lattice. The arrows indicate the out-of-plane spin orientation. In the bottom panel, to better illustrate the crystal structure, the three I atoms are labeled in the top (orange) and bottom (blue) layers, which form equilateral triangles (solid and dashed red lines, respectively).

The CrI_3 layers are held together by vdW forces, and the layer stacking of bulk CrI_3 crystal exhibits a temperature dependence and a structural transition at about 220 K[37]. At high temperatures (above 220 K), bulk CrI_3 crystal has monoclinic stacking ($C2/m$). It undergoes a structural transition near 210-220 K and becomes rhombohedral stacking ($R\bar{3}$) at low temperatures. However, this structural transition is usually absent in exfoliated few-layer CrI_3. As a result, the layer stacking of exfoliated few-layer CrI_3 remains to be monoclinic at low temperatures, which is different from bulk CrI_3 crystal. This difference of the layer stacking between few-layer CrI_3 flakes and bulk CrI_3 crystal plays an important role in determining the interlayer magnetism. This led to the surprising discovery of the unexpected layer-dependent magnetism when the exfoliated few-layer CrI_3 flakes were studied for the first time[29]. This stacking-dependent interlayer magnetism is also closely related to the pressure control of interlayer magnetism in atomically thin CrI_3, which will be the focus of Chapter 4.

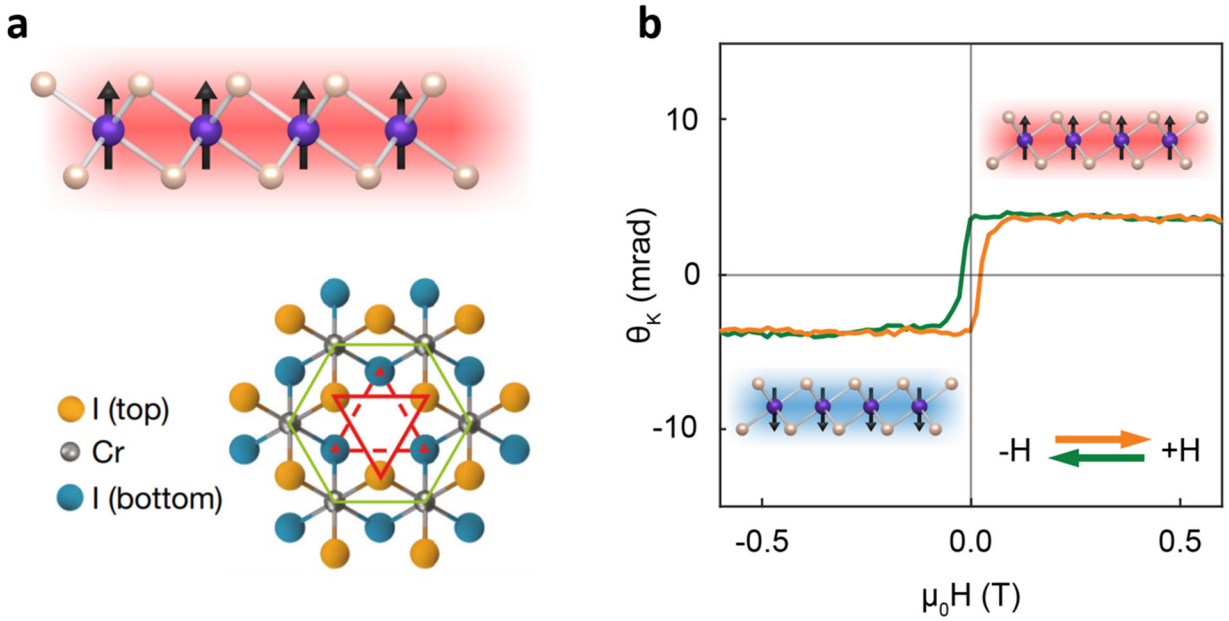

Figure 2.1. Monolayer CrI_3. (**a**) Crystal structure of monolayer CrI_3 with the side (upper) and top (bottom) views. In the upper panel, the purple and brown atoms represent the Cr and I atoms, respectively. The arrows indicate the out-of-plane spin orientation. In the bottom panel, the three I atoms are labeled in the top (orange) and bottom (blue) layers, which form equilateral triangles (solid and dashed red lines, respectively). (**b**) MOKE signal, θ_K, as a function of magnetic field, $\mu_0 H$, measured from a monolayer CrI_3 at 15 K. Green (orange) curve corresponds to decreasing (increasing) magnetic field. Reproduced from reference[29] with permission.

The bulk CrI_3 crystal can be mechanically exfoliated onto SiO_2/Si substrate down to the monolayer limit by using the Scotch tape method. The thickness of CrI_3 flakes can be identified by their optical contrast relative to the substrate using the established optical contrast model of CrI_3[29]. Although the bulk CrI_3 crystal seems to be stable under ambient conditions, the few-layer CrI_3 flakes can degrade immediately after being exfoliated. The main degradation pathway of CrI_3 is found to be the photocatalytic substitution of iodine by water[38]. To overcome this challenge, few-layer CrI_3 flakes need to be exfoliated in an inert gas glove box with water and oxygen concentration <0.5 ppm. To carry out the later optical or electrical measurements, the solution is

to sandwich the CrI_3 flakes between the top and bottom hBN flakes. In the resulting heterostructure sandwich, the encapsulated CrI_3 flake is no longer directly exposed to water in the air and thus remains intact under ambient conditions.

The magnetic order in the exfoliated few-layer CrI_3 can be probed by the magneto-optic effects. In this thesis, we mainly employed the magneto-optical Kerr effect and magnetic circular dichroism as an optical probe of the out-of-plane magnetization in CrI_3, which we will discuss in detail in Section 2.2. Here we start with magneto-optical Kerr effect (MOKE) measurement, which is an optical technique that detects the rotation of reflected linearly polarized light induced by the magnetic circular birefringence of the out-of-plane magnetization. Figure 2.1b shows the MOKE signal, θ_K, as a function of magnetic field, $\mu_0 H$, measured from a monolayer CrI_3 at 15 K. The Kerr rotation shows a clear magnetic hysteresis loop, a hallmark of ferromagnetism, demonstrating the first 2D monolayer with intrinsic magnetic order. Furthermore, the remanent signal at $\mu_0 H = 0$ T is nearly the same as the saturated signal at $\mu_0 H = 0.5$ T, i.e., the spin-flip transition at $\mu_0 H = 0$ T is very sharp, imply Ising ferromagnetism in monolayer CrI_3. A temperature dependence measurement was also carried out to measure the Curie temperature of monolayer CrI_3. The remanent signal and magnetic hysteresis loop decrease as the temperature increases, and go to zero at about 45 K, showing a transition from ferromagnetism to paramagnetism. This suggests that the Curie temperature of monolayer CrI_3 is about 45 K, which is slightly lower than that of bulk CrI_3 crystal[29].

2.2 Magneto-optical Kerr effect and magnetic circular dichroism

In this section, we are going to shift our focus to investigating the optical techniques and magneto-optic effects we employed to probe the magnetic order in the exfoliated few-layer CrI_3.

We first note that the exfoliated flakes of 2D magnetic materials are usually limited to micrometer-scale size, and are atomically thin. This is typically too small to provide a measurable signal for conventional magnetic probes, which are commonly used for millimeter-scale bulk crystals, for example, neutron scattering, X-ray magnetic circular dichroism, vibrating-sample magnetometry, and superconducting quantum interference device (SQUID) magnetometry. Instead, magneto-optic effects provide very powerful methods to identify various types of magnetic orders in 2D flakes with both high sensitivity and submicrometer resolution. In particular, we will focus on magnetic circular birefringence and dichroism in this section. On the other hand, the electrical techniques that can probe magnetic orders will be discussed in detail in Chapter 3.

When a sample is magnetized with an out-of-plane magnetization, M, the material will exhibit both magnetic circular birefringence (MCB) and magnetic circular dichroism (MCD) shown in Fig. 2.2. That is, MCB induces a phase difference between right-circularly polarized (RCP) and left-circularly polarized (LCP) light, while MCD incurs an amplitude difference between RCP and LCP light. Both effects can be derived from the complex optical conductivity of the material, which is directly related to its out-of-plane magnetization. When the linearly polarized incident light, an equal superposition of RCP and LCP light, is reflected off the surface of the magnetized material. The phase difference between RCP and LCP light causes the Kerr rotation of the linear polarization, θ_K, from the polar magneto-optical Kerr effect (MOKE), which is determined by the imaginary part of the complex optical conductivity. The amplitude difference between RCP and LCP light induces the ellipticity of the polarization from reflective magnetic circular dichroism (RMCD), which is determined by the real part of the complex optical conductivity. The resulting MOKE and RMCD signals can serve as an ideal probe of the out-of-plane magnetization. For example, both MOKE and RMCD signals from a monolayer CrI_3 show

a clear magnetic hysteresis loop and a large remanent signal at zero magnetic field. However, we note that extracting quantitative values of the optical conductivity and out-of-plane magnetization from the magnetic layer in a multilayer structure is challenging, due to the complex thin-film interference from multiple reflections at different interfaces.

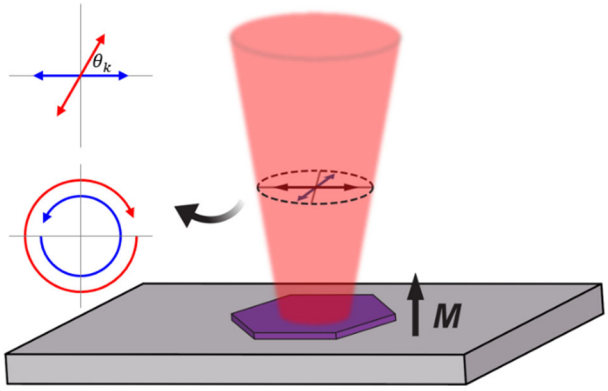

Figure 2.2. Magnetic circular birefringence and dichroism. The linearly polarized incident light is reflected by a sample with an out-of-plane magnetization, where the Kerr rotation and the ellipticity of the polarization are induced.

In practice, both MOKE and RMCD measurements are performed in a closed-cycle helium cryostat with a base temperature of 1.6 K. A power-stabilized 632.8 nm (1.96 eV) HeNe laser excites the sample at normal incidence with fixed power of about 100 nW. Magnetic fields of up to 9 T can be applied in the out-of-plane direction using a superconducting magnet. The incidence light first goes through a linear polarizer, and the intensity and polarization modulation is induced by a mechanical chopper and photoelastic modulator (PEM), respectively. The modulated incident light is then directed through a beam splitter to the sample, and the reflected light is collected by a silicon avalanche photodetector. The output signal is measured by two lock-in amplifiers at the chopper and PEM frequencies, corresponding to the reflection and PEM signals, respectively. The

MOKE and RMCD signals can be then derived from the resulting reflection and PEM signals[39]. The MOKE signal is defined as the polarization rotation angle, and the RMCD signal is defined as $(R_{RCP} - R_{LCP})/(R_{RCP} + R_{LCP})/2$, where R_{RCP} (R_{LCP}) represents refection amplitude for right (left) circularly polarized light.

2.3 Antiferromagnetic interlayer coupling in bilayer CrI_3

Considering both monolayer CrI_3 and bulk CrI_3 crystal exhibit ferromagnetism, one may expect that the exfoliated CrI_3 flakes of any thickness between monolayer and bulk should be all simply ferromagnetic. However, this is not true, and it is very surprising to find that the exfoliated bilayer CrI_3 is actually layered antiferromagnetic (A-type AFM) when it was measured for the first time[29]. This discrepancy is originated from the difference of the layer stacking between few-layer CrI_3 flakes and bulk CrI_3 crystal, which plays an important role in determining the interlayer magnetism, and will be discussed in detail in Chapter 4.

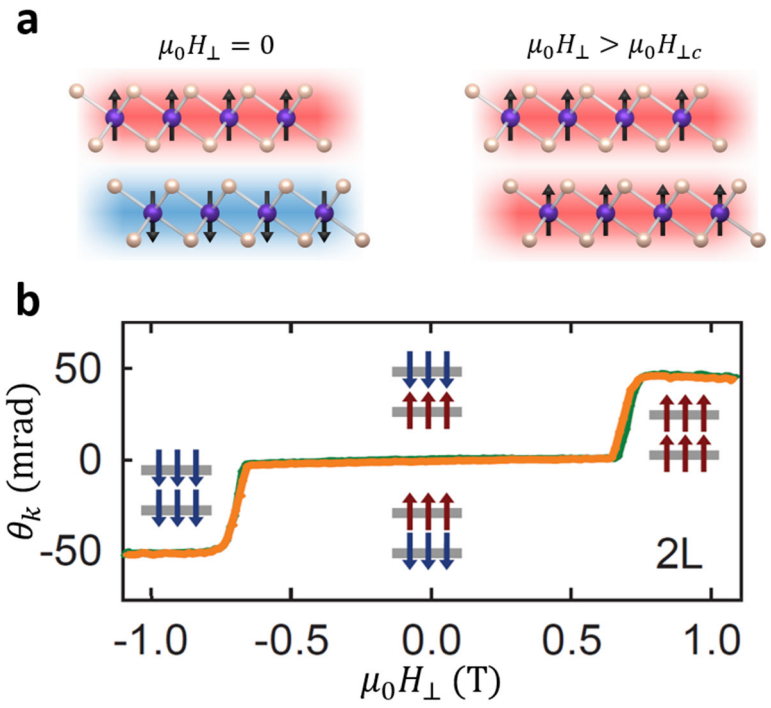

Figure 2. 3. Antiferromagnetic interlayer coupling in bilayer CrI_3. (**a**) Schematic of magnetic states in bilayer CrI_3. (Left) Layered antiferromagnetic ground state at zero magnetic field. (Right) Fully spin-polarized states above the out-of-plane critical magnetic field. (**b**) MOKE signal, θ_K, as a function of magnetic field, $\mu_0 H$, measured from a bilayer CrI_3 at 15 K. Green (orange) curve corresponds to decreasing (increasing) magnetic field. Insets show the corresponding magnetic states. Reproduced from reference[29] with permission.

In bilayer CrI_3, the layered antiferromagnetic (A-type AFM) structure is that the spins align ferromagnetically out of plane within each layer, the same as monolayer CrI_3, but are coupled antiferromagnetically between the two CrI_3 layers, which is shown in Fig. 2.3a (left). As a result, the opposite magnetizations in the two CrI_3 layers result in vanishing net magnetization, and thus a nearly zero MOKE signal at zero magnetic field (Fig. 2.3b). The magnetic ground state is either the ↑↓ or ↑↓ state, where the arrows indicate the out-of-plane magnetizations in the top and bottom layers, respectively. Since the antiferromagnetic interlayer coupling is relatively weak, the

magnetizations of the two CrI_3 layers can be fully aligned in the same direction by applying an out-of-plane magnetic field as shown in Fig. 2.3a (right). The spin-flip transitions happen at about ±0.7 T (the out-of-plane critical magnetic field), corresponding to the abrupt increase in the MOKE signal. The resulting fully spin-polarized states are the ↑↑ and ↓↓ states, which corresponds to the two large plateaus of MOKE signal with opposite signs on the two sides (Fig. 2.3b).

2.4 Layered antiferromagnetism in few-layer CrI_3

Now we know that monolayer CrI_3 is ferromagnetic and bilayer CrI_3 is layered antiferromagnetic, a natural question is arising now: what is the magnetic order in a thicker CrI_3? Figure 2.4a shows the normalized MOKE and RMCD signals of mono- to four-layer CrI_3 as a function of magnetic field. We first note that each monolayer of CrI_3 should be ferromagnetic, while the interlayer coupling is antiferromagnetic between adjacent CrI_3 layers, as demonstrated in the monolayer and bilayer CrI_3 cases. For the trilayer and four-layer CrI_3 cases, similar layer-by-layer switching behavior is observed as a function of magnetic field in the MOKE signals. Moreover, the number of magnetic states (or magnetization plateaus in the MOKE signal) also increases as the CrI_3 layer thickness increases, and we get a conclusion that there are N+1 magnetic states for an N-layer CrI_3 (up to 4).

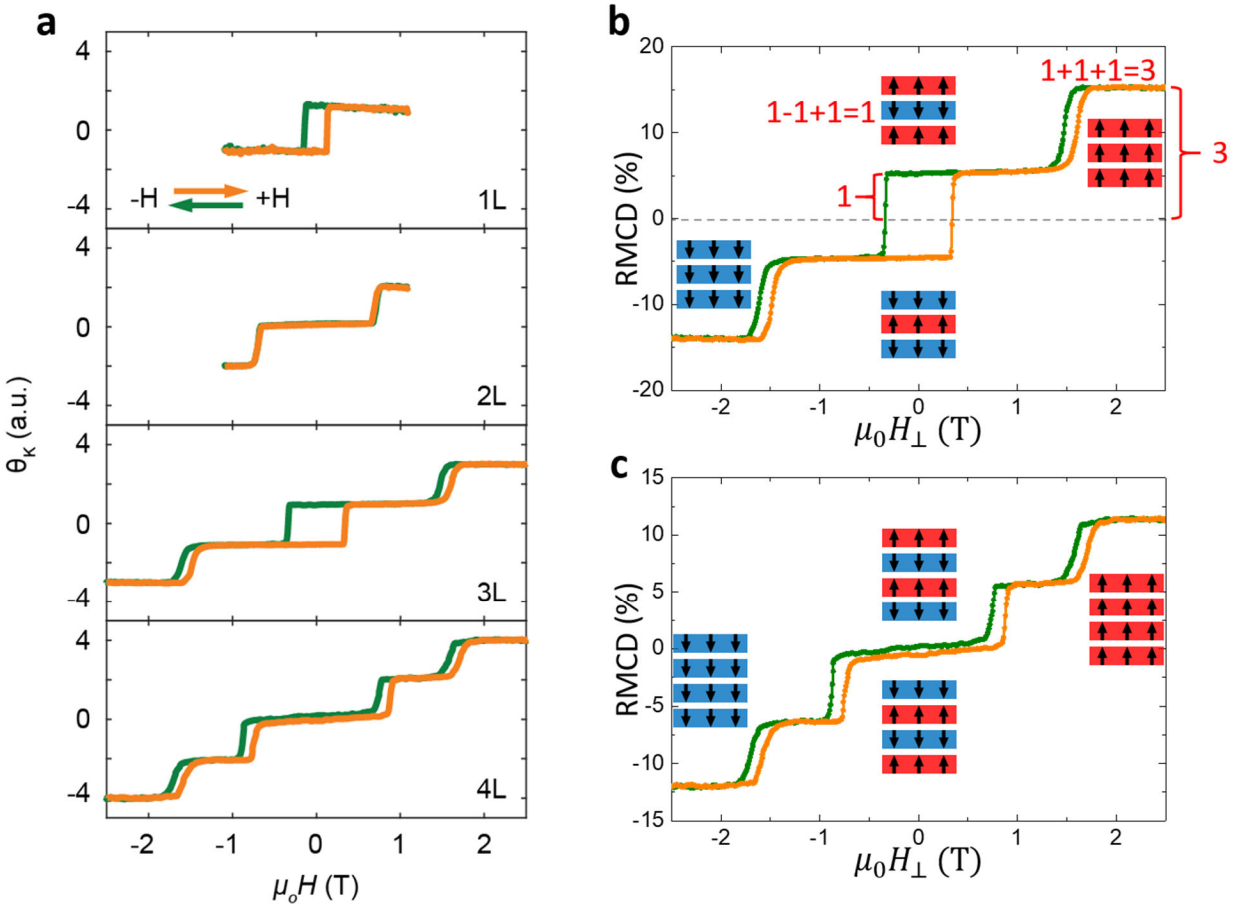

Figure 2. 4. Layered antiferromagnetism in few-layer CrI_3. (**a**) Normalized MOKE and RMCD signals of mono- to four-layer CrI_3 as a function of magnetic field. Green (orange) curve corresponds to decreasing (increasing) magnetic field. (**b**) RMCD signal of trilayer CrI_3 as a function of magnetic field. Insets show the corresponding magnetic states of trilayer CrI_3. The ratio between the RMCD signals of the four magnetic states is close to -3:-1:1:3. (**c**) RMCD signal of four-layer CrI_3 as a function of magnetic field. Insets show the corresponding magnetic states of four-layer CrI_3. Reproduced from reference[29,40] with permission.

We now investigate the trilayer CrI_3 case. Since there are three ferromagnetic layers in trilayer CrI_3 and they are antiferromagnetically coupled, the magnetic ground at zero magnetic field should be either the ↑↓↑ or ↓↑↓ state. As shown in Fig. 2.4b, these two magnetic states match well with the two plateaus of relatively small RMCD signal with opposite signs and the

magnetic hysteresis loop centered at zero magnetic field. Similar to the bilayer CrI_3 case, the magnetizations of the three CrI_3 layers can be fully aligned in the same direction by applying an out-of-plane magnetic field, and the resulting fully spin-polarized states should the ↑↑↑ and ↓↓↓ states. These two magnetic states match well with the two plateaus of relatively large RMCD signal with opposite signs on the two sides.

The RMCD signal can also serve approximately as a quantitative probe of the relative net magnetization for different magnetic states. If we assume the saturation magnetization of monolayer CrI_3 is M_s, the net magnetizations of the ↑↓↑, ↓↑↓, ↑↑↑ and ↓↓↓ states will be ± 1 M_s and ± 3 M_s, respectively. These net magnetizations agree well with the ratio between the observed RMCD signals of the four magnetic states, which is close to -3:-1:1:3. However, we note that the ratio between the RMCD signals can have a deviation from the relative net magnetizations of the magnetic states, due to the complex thin-film interference in a multilayer structure and the difference of the electronic structure for different magnetic states. Furthermore, we find the spin-flip transition from the ↑↓↑ state to the ↑↑↑ state happens at about 1.5 T, which is about twice the critical magnetic field of bilayer CrI_3. This can be explained as follows. The spin-flip transitions in few-layer CrI_3 happen when the magnetic field is swept at a critical value that the Zeeman energy overcomes the antiferromagnetic interlayer coupling. Since the middle layer of trilayer CrI_3 is antiferromagnetically coupled to the top and bottom layers, trilayer CrI_3 has two antiferromagnetic interfaces, while bilayer CrI_3 only has one antiferromagnetic interface. As a result, the ratio between the critical magnetic fields of trilayer CrI_3 and bilayer CrI_3 is about 2:1.

We next investigate the four-layer CrI_3 case. Since four-layer CrI_3 has four ferromagnetic layers that are antiferromagnetically coupled, the magnetic ground at zero magnetic field should be either the ↑↓↑↓ or ↓↑↓↑ state, corresponding to nearly zero RMCD signal at zero magnetic

field, as shown in Fig. 2.4c. The fact that the RMCD signal is not exactly zero can be attributed to the asymmetry of the CrI_3 layers caused by the fabrication process. Similar to the bilayer and trilayer CrI_3 cases, the magnetizations of the four CrI_3 layers can be fully aligned in the same direction by applying an out-of-plane magnetic field, and the resulting fully spin-polarized states are the ↑↑↑↑ and ↓↓↓↓ states, corresponding to the two plateaus of relatively large RMCD signal with opposite signs on the two sides.

We find that the RMCD signal of four-layer CrI_3 also shows additional intermediate plateaus. With the assumption that the saturation magnetization of monolayer CrI_3 is M_s, the net magnetizations of the ↑↓↑↓, ↓↑↓↑, ↑↑↑↑ and ↓↓↓↓ states will be $\pm 0\ M_s$ and $\pm 4\ M_s$, respectively. Since the intermediate plateaus are at about half the values in the fully spin-polarized states, the corresponding magnetic states should have half the net magnetization of the fully spin-polarized states, which are $\pm 2\ M_s$. Considering the magnetic state should have one layer polarized opposite to the other three, there are four possible magnetic states for the intermediate plateau at positive magnetic field, {↑↓↑↑, ↑↑↓↑, ↓↑↑↑, ↑↑↑↓}, and the four time-reversal copies, {↓↑↓↓, ↓↓↑↓, ↑↓↓↓, ↓↓↓↑}, are for the intermediate plateau at negative magnetic field. However, these possible magnetic states should be indistinguishable in the RMCD signal because of the same net magnetization. To identify the specific magnetic states corresponding to the intermediate plateaus will require a means to distinguish the magnetization of individual layers. One possible way is to measure electron tunneling, where the tunneling current is likely to be sensitive to the position of the one layer with the minority magnetization due to the spin-filtering effect, which will be discussed in detail in Chapter 3.

2.5 MONTE CARLO SIMULATIONS OF LAYERED ANTIFERROMAGNETISM

The magnetic order in CrI_3 in the few-layer limit is layered antiferromagnetic with out-of-plane magnetic anisotropy. This has also been observed in metallic and all-oxide synthetic magnetic multilayer films[41–43], and can be described by the Ising model[44], where the spins in each layer have ferromagnetic intralayer coupling, while the interlayer coupling is antiferromagnetic. The Monte Carlo simulations performed for this Ising model are in good agreement with the RMCD signals and the magnetizations of bilayer, trilayer, and four-layer CrI_3.

We simulated the magnetic order in few-layer CrI_3 by choosing the Ising model based on the CrI_3 crystal structure, using the Monte Carlo method with classical Ising spins ($S = \pm 1$). The Ising model consists of *N* ferromagnetic layers, where each layer is a $L \times L$ honeycomb lattice with one spin at each lattice site, corresponding to each Cr atom site. The intralayer nearest-neighbor coupling is ferromagnetic, corresponding to a positive exchange coupling (J_{intra}). The antiferromagnetic interlayer coupling is implemented by a negative exchange coupling (J_{inter}) between the nearest-neighbor sites in adjacent layers. The Hamiltonian of the Ising model is defined as

$$\mathcal{H} = \sum_{n=1}^{N} (-\frac{1}{2} J_{intra} \sum_{<i,j>} S_{n,i} S_{n,j} - \frac{1}{2} J_{inter} \sum_{i} S_{n,i} S_{n\pm1,i} - H \sum_{i} S_{n,i}),$$

where $S_{n,i}$ is the spin on the i site of the n layer, and H is the external magnetic field.

The magnetization as a function of magnetic field was simulated using the Metropolis Monte Carlo algorithm by flipping the individual spin on each site one-by-one. We simulated a 50×50 honeycomb lattice with periodic boundary conditions. We set $J_{intra} = -J_{inter} = 1$, and express the external magnetic field (H) in the unit of J_{inter}. We chose to simulate at a selected

temperature ($T \approx 0.5\,T_c$) to allow the spins to fluctuate and avoid trapping in a local energy-minimum state. $2000 \times N \times L \times L$ Monte Carlo steps were performed to make sure the system reached a quasi-equilibrium state at each magnetic field, then the net magnetization was calculated.

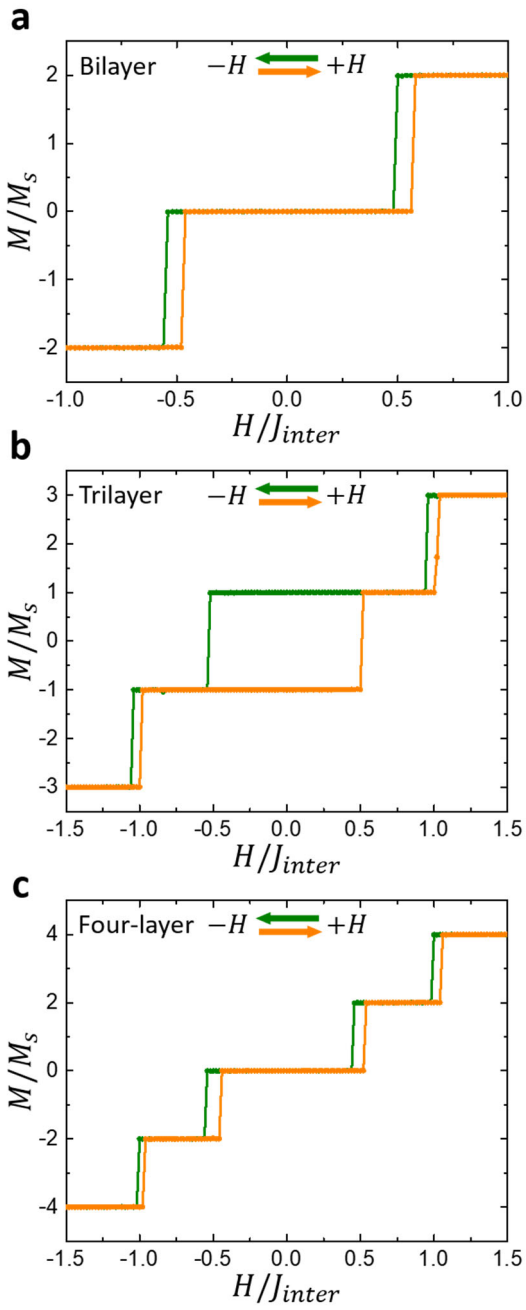

Figure 2. 5. Monte Carlo simulations of symmetric few-layer CrI_3. All the layers of bilayer CrI_3 (**a**), trilayer CrI_3 (**b**), and four-layer CrI_3 (**c**) are assigned the same spin value $S = \pm 1$. Green

(orange) curve corresponds to decreasing (increasing) magnetic field. M_S is the saturation magnetization of monolayer CrI_3. Reproduced from reference[40] with permission.

The simulated magnetizations of bilayer, trilayer, and four-layer CrI_3 as a function of magnetic field are shown in Fig. 2.5, a, b, and c, respectively, which are in good agreement with the RMCD signals and the magnetizations, except for the finite non-zero RMCD signals at zero magnetic field in the bilayer and four-layer CrI_3. This is because, in the simulations, we assumed that the spins of each layer are identical, and have the same spin value $S = \pm 1$. However, in the experiment, the symmetry between the top and bottom layers of CrI_3 can be broken during the fabrication process, such as the asymmetry induced by the top and bottom few-layer graphene contacts and hBN flakes. To simulate an asymmetric bilayer CrI_3, we slightly changed the spin values of the top and bottom CrI_3 layers to break this symmetry. Figure 2.6a shows the simulated magnetization of an asymmetric bilayer CrI_3 with the spin values $S = \pm 1.05$ and $S = \pm 0.95$ for the top and bottom layers, respectively. Similar simulated magnetization of an asymmetric four-layer CrI_3 is shown in Fig. 2.6b. The finite non-zero magnetizations of the asymmetric bilayer and four-layer CrI_3 agree well with the finite non-zero RMCD signals, supporting the assumption of symmetry breaking in CrI_3.

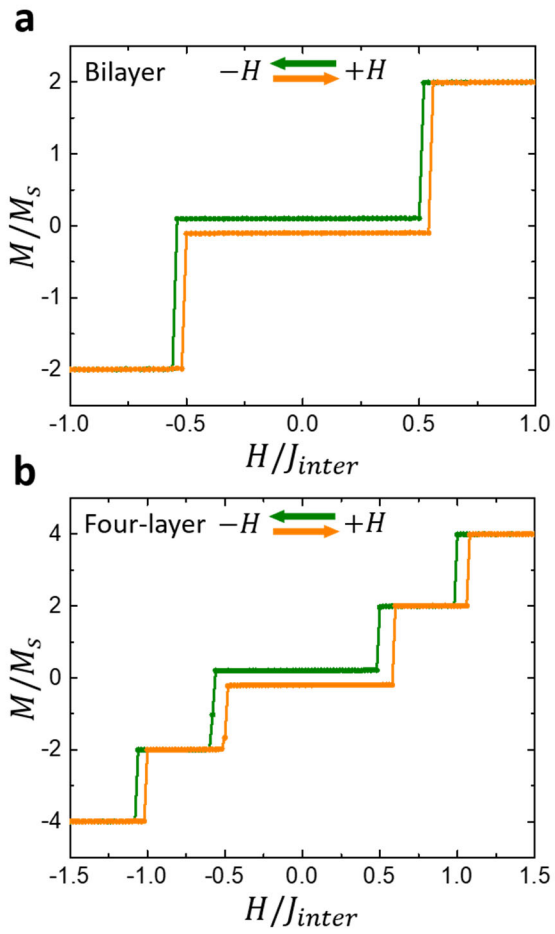

Figure 2. 6. Monte Carlo simulations of asymmetric bilayer and four-layer CrI_3. (**a**) Bilayer CrI_3 is assigned the spin values $S = \pm 1.05$ and $S = \pm 0.95$ for the top and bottom layers, respectively. (**b**) Four-layer CrI_3 is assigned with the spin values $S = \pm 1.1$, $S = \pm 1$, $S = \pm 1$, and $S = \pm 0.9$ for the four layers from top to bottom, respectively. In both the bilayer and the four-layer CrI_3, the different spin amplitudes between each layer – equivalent to breaking the up-down symmetry – results in the appearance of the spontaneous magnetization at zero magnetic field. Reproduced from reference[40] with permission.

Chapter 3. GIANT TUNNELING MAGNETORESISTANCE IN VAN DER WAALS MAGNETIC TUNNEL JUNCTIONS

In Chapter 3, we will explore the giant tunneling magnetoresistance effect in vdW spin-filter magnetic tunnel junctions. We will first introduce the tunneling magnetoresistance effect in conventional magnetic tunnel junctions, and discuss the double spin-filtering effect in spin-filter magnetic tunnel junctions. We will then demonstrate tunneling magnetoresistance by using bilayer CrI_3 as a tunnel barrier, which can be dramatically enhanced with increasing CrI_3 layer thickness. We will also present that a pair of bistable magnetic states in four-layer CrI_3 can be switched reversibly by electrostatic gating in a dual-gated structure, demonstrating a new kind of voltage-controlled vdW spintronic devices.

3.1 MAGNETIC TUNEL JUNCTION

Magnetic multilayer devices that exploit magnetoresistance are the backbone of magnetic sensing and data storage technologies. The conventional device geometry consists of two magnetic layers separated by a thin non-magnetic spacer layer as shown in Fig. 3.1a. This spacer layer can be either a non-magnetic metal or an insulator as a tunnel barrier, where the giant magnetoresistance (GMR) or tunnel magnetoresistance (TMR) effect can be realized. Figure 3.1b shows that the electrical resistance can be controlled as the magnetization direction of the two ferromagnetic layers is switched individually by an external magnetic field. The resistance is relatively large or small when the two magnetizations are in antiparallel or parallel alignment, respectively. To achieve the antiparallel and parallel magnetic states by applying an external magnetic field, one of the two magnetizations needs to be fixed or stationary. This can be done in mainly two ways. (1) Induce a different coercive field by making one ferromagnetic layer much

thicker than the other, which thus requires a stronger external magnetic field to flip it. (2) Bring one ferromagnetic layer in contact with an antiferromagnetic layer to induce an effective field, so that the ferromagnetic layer is pinned by the exchange bias. In both cases, one layer becomes the pin layer, and the other one is the free layer as shown in Fig. 3.1b.

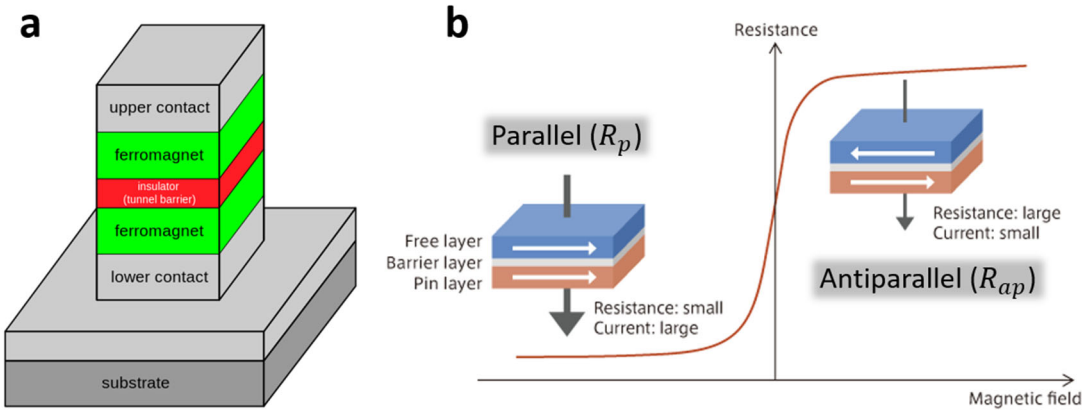

Figure 3. 1. Tunneling magnetoresistance effect in magnetic tunnel junctions. (**a**) Schematic of magnetic tunnel junction which consists of two magnetic layers separated by an insulator as a tunnel barrier. (**b**) The electrical resistance of the magnetic tunnel junction is relatively large or small when the two magnetizations are in antiparallel or parallel alignment, respectively, which can be controlled by an external magnetic field.

For the GMR effect that occurs in spin valves, the spacer layer is a non-magnetic metal, and the effect is based on the dependence of electron scattering on spin orientation[45–47]. This was first discovered in the Fe/Cr/Fe multilayer system, and the 2007 Nobel Prize in Physics was awarded to Albert Fert and Peter Grünberg for the discovery of GMR. For the TMR effect that occurs in magnetic tunnel junctions (MTJs), the spacer layer is an insulator as a tunnel barrier. The TMR effect was originally discovered in 1975 but did not attract much attention at that time[48]. Large TMR ratio was later observed at room temperate in 1995, simulating broad extensive research into MTJs[49,50]. Most of the early studies of MTJs used an aluminum oxide insulator layer

as the tunnel barrier, which is amorphous and thus heavily disordered. A relatively large TMR effect can be achieved, and the TMR ratio is mostly determined by the spin density of states of the two ferromagnetic electrodes, which can be well described by the Julliere formula. In 2004, a significant enhancement of TMR ratio was obtained in the Fe/MgO/FeCo system, which originates from the symmetry filtering in the crystalline tunnel barrier with lattice matching[51,52], and the TMR ratio demonstrated experimentally has continued to increase rapidly[53].

3.2 SPIN-FILTERING EFFECT

Spin filter, on the other hand, can realize a giant TMR effect by taking an alternative approach[54], which utilizes a magnetic tunnel barrier to manipulate the spins of the tunneling electrons through the spin-filtering effect. When unpolarized electrons tunnel through a magnetic tunnel barrier, the spin-up and spin-down electrons are selectively filtered by the spin-dependent tunneling probability, which originates from the distinct tunnel barrier heights for the majority and minority spin channels. As shown in Fig. 3.2a, after tunneling through a magnetic tunnel barrier as a spin filter, the unpolarized electrons from a non-magnetic electrode will become highly spin-polarized.

The giant TMR effect can be produced by the double spin-filtering effect in a spin-filter magnetic tunnel junction. Different from the conventional MTJs based on the magnetism in the two ferromagnetic electrodes, the spin-filter MTJs utilize the magnetism of the magnetic tunnel barriers, which consist of NM/SF/SF/NM or NM/SF/spacer layer/SF/NM. Here, NM represents the non-magnetic electrode, and SF represents the spin filter. Figure 3.2b shows that when the magnetizations of the two spin filters are in antiparallel alignment, the tunneling current is small because the spin-conserving tunneling of an electron through the two layers in sequence is suppressed. This suppression is removed, and the tunneling current becomes large when the

magnetizations of the two spin filters are aligned in parallel as shown in Fig. 3.2c. Switching the two spin filters between antiparallel and parallel states can produce a large TMR effect, which was first observed demonstrated in the Al/EuS/Al_2O_3/EuS/Al system[55,56].

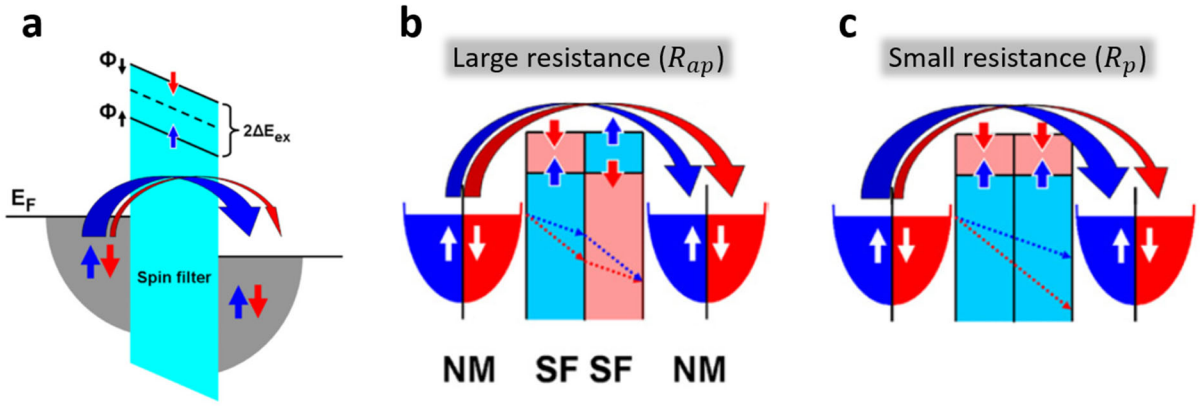

Figure 3. 2. Double spin-filtering effect in spin-filter magnetic tunnel junctions. (**a**) Spin-filtering effect in a magnetic tunnel barrier. (**b**) The resistance is large when the two spin filters are in antiparallel alignment. (**c**) The resistance is small when the two spin filters are aligned in parallel. Reproduced from reference[56] with permission.

3.3 Bilayer CrI_3 spin-filter magnetic tunnel junction

The unique layered antiferromagnetism we have discussed in detail in Chapter 2 makes few-layer CrI_3 desirable for realizing atomically thin magnetic multilayer devices based on the spin-flitering effect. As shown in Fig. 3.3, when the magnetizations of the two layers in a bilayer CrI_3 are switched between antiparallel (left) and parallel states (middle and right), giant TMR effect can be produced by the double spin-filtering effect, where each CrI_3 layer serves as a spin filter. Compared with the conventional magnetic multilayer devices which require different choices of metallic or insulating, magnetic or non-magnetic layers, the layered antiferromagnetic structure of bilayer CrI_3 avoids the need for fabricating separate spin filters with the spacer layer

and the requirement for lattice matching. This guarantees sharp atomic interfaces between spin filters, which is crucial for achieving a giant TMR effect.

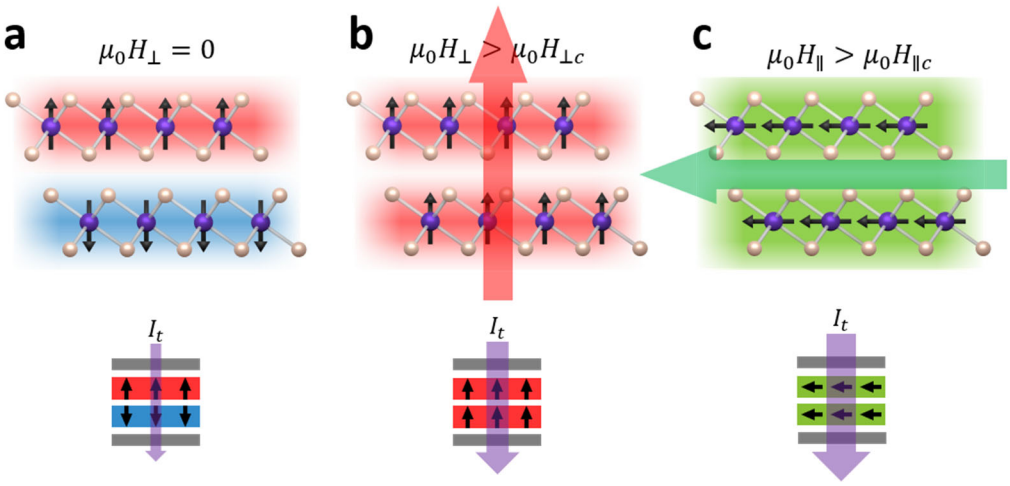

Figure 3. 3. Magnetic states in bilayer CrI_3. (**a**) Layered antiferromagnetic state which suppresses the tunneling current at zero magnetic field due to the double spin-filtering effect. (**b**) Fully spin-polarized state with out-of-plane magnetizations where the suppression is removed. (**c**) Fully spin-polarized state with the magnetizations aligned in the in-plane direction where the suppression is also removed. Reproduced from reference[40] with permission.

To study the giant TMR effect in vdW heterostructures, we explore the spin-filter MTJs based on atomically thin CrI_3[40,57–59]. Figure 3.4a shows the essential structure of the spin-filter MTJ, which consists of two few-layer graphene contacts separated by a thin CrI_3 layer as the tunnel barrier. The spin-filter MTJ is further encapsulated between two hBN flakes to avoid degradation. As shown in Fig. 3.4a, a DC bias voltage (V) is applied to the top graphene contact while the bottom graphene contact is grounded. The resulting tunneling current (I_t) is amplified and acquired by a current preamplifier. Figure 3.4b shows an optical microscope image of a typical bilayer CrI_3 device, which is obtained by stacking exfoliated 2D materials using a dry transfer process in a glovebox. The tunneling junction area is less than ~1 μm^2 to avoid effects caused by lateral

magnetic domain structures[29,60]. We note that all the measurements discussed in this Chapter were carried out at a temperature of 2 K, unless otherwise specified.

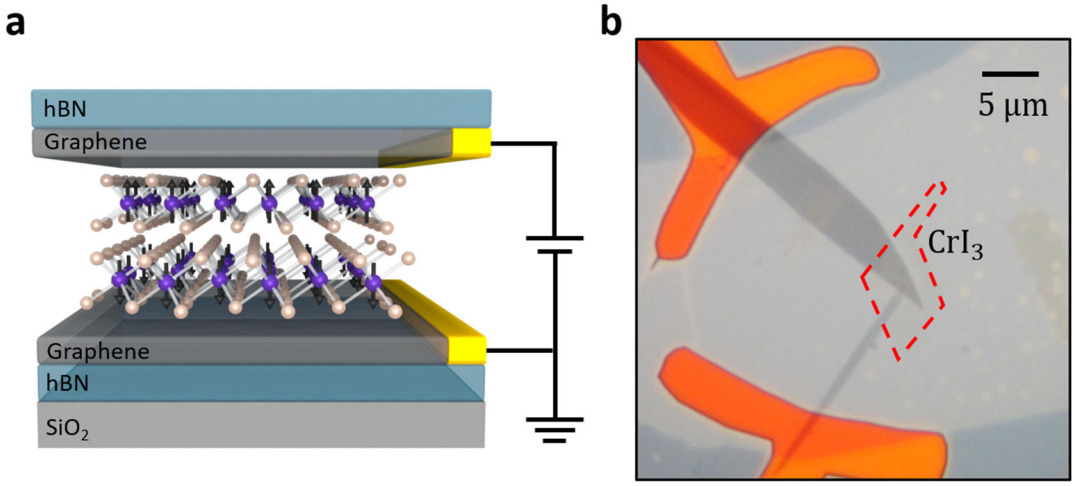

Figure 3. 4. Bilayer CrI_3 spin-filter magnetic tunnel junction. (**a**) Schematic of spin-filter magnetic tunnel junction with bilayer CrI_3 functioning as the spin filters sandwiched between two few-layer graphene contacts. (**b**) Optical microscope image of a typical bilayer CrI_3 device. The red dashed line shows the position of the bilayer CrI_3. Reproduced from reference[40] with permission.

We have made and investigated devices with bilayer, trilayer, and four-layer CrI_3 for this study. We begin with the case of bilayer CrI_3 for simplicity, and the trilayer and four-layer CrI_3 cases will be discussed in detail in Section 3.4. Figure 3.5a shows the tunneling current (I_t) as a function of the applied DC bias voltage (V) measured at selected magnetic fields ($\mu_0 H$). Different from the tunneling devices using non-magnetic hBN or TMDs as the tunnel barrier[61–63], the I_t-V curve exhibits a strong magnetic field dependence. As shown in Fig. 3.5a, the tunneling current is much smaller at 0 T (purple trace) than it is in the presence of an out-of-plane field (red trace) or an in-plane field (green trace). This magnetic field dependence of the tunneling current implies a spin-dependent tunneling probability related to the magnetic structure of bilayer CrI_3.

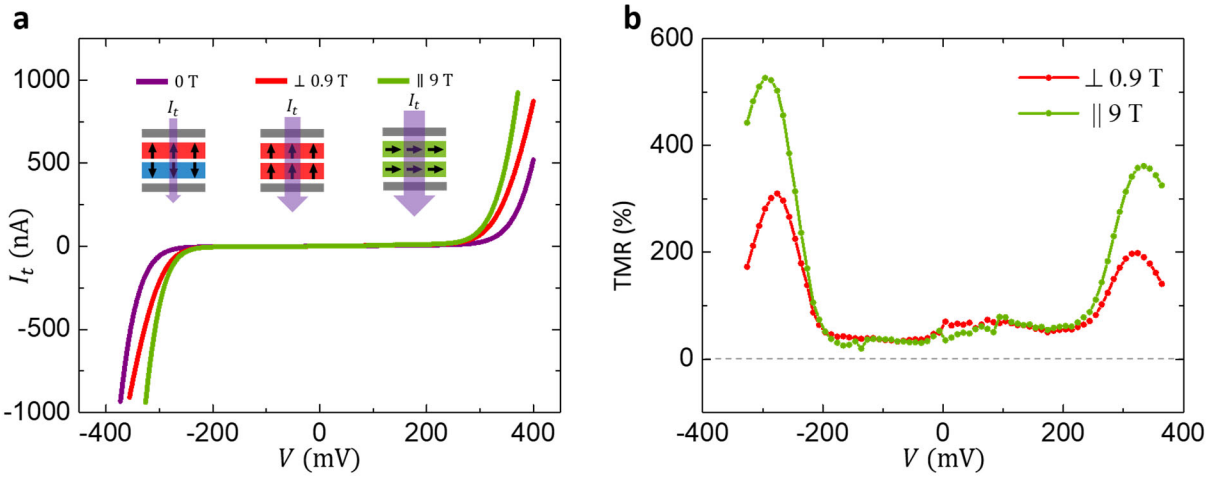

Figure 3. 5. Tunneling current of bilayer CrI_3 spin-filter magnetic tunnel junction. (**a**) Tunneling current as a function of bias voltage measured from the bilayer CrI_3 spin-filter MTJ at selected out-of-plane and in-plane magnetic fields. Insets show the schematic of the magnetic states for each I_t-V curve. (**b**) TMR ratio as a function of bias voltage for out-of-plane and in-plane magnetic fields, calculated from the I_t-V curves in (a). Reproduced from reference[40] with permission.

To investigate the connection between the magnetic states of bilayer CrI_3 and the observed magnetoresistance, we next measure the tunneling current as a function of out-of-plane magnetic field measured at a particular bias voltage (-290 mV). The green and orange curves in Fig. 3.6b correspond to decreasing and increasing magnetic fields, respectively. The tunneling current exhibits plateaus with mainly two values, about -36 nA and -155 nA. The small current plateau is observed at low magnetic fields, and there is a sharp jump to the large current plateau when the magnetic field exceeds a critical value. We also employ reflective magnetic circular dichroism (RMCD) measurement to probe the out-of-plane magnetization of the bilayer CrI_3 near the tunneling area. Figure 3.6a shows the RMCD signal as a function of magnetic field measured under the same experimental conditions. The RMCD signal is small at low magnetic fields, corresponding to the layered antiferromagnetic ground state (either ↑↓ or ↑↓), where the arrows

indicate the out-of-plane magnetizations in the top and bottom layers, respectively. As the magnitude of the magnetic field exceeds a critical value, the RMCD signal becomes large corresponding to the fully spin-polarized states (↑↑ and ↓↓), consistent with the layered antiferromagnetism of bilayer CrI_3 we have discussed in detail in Chapter 2.

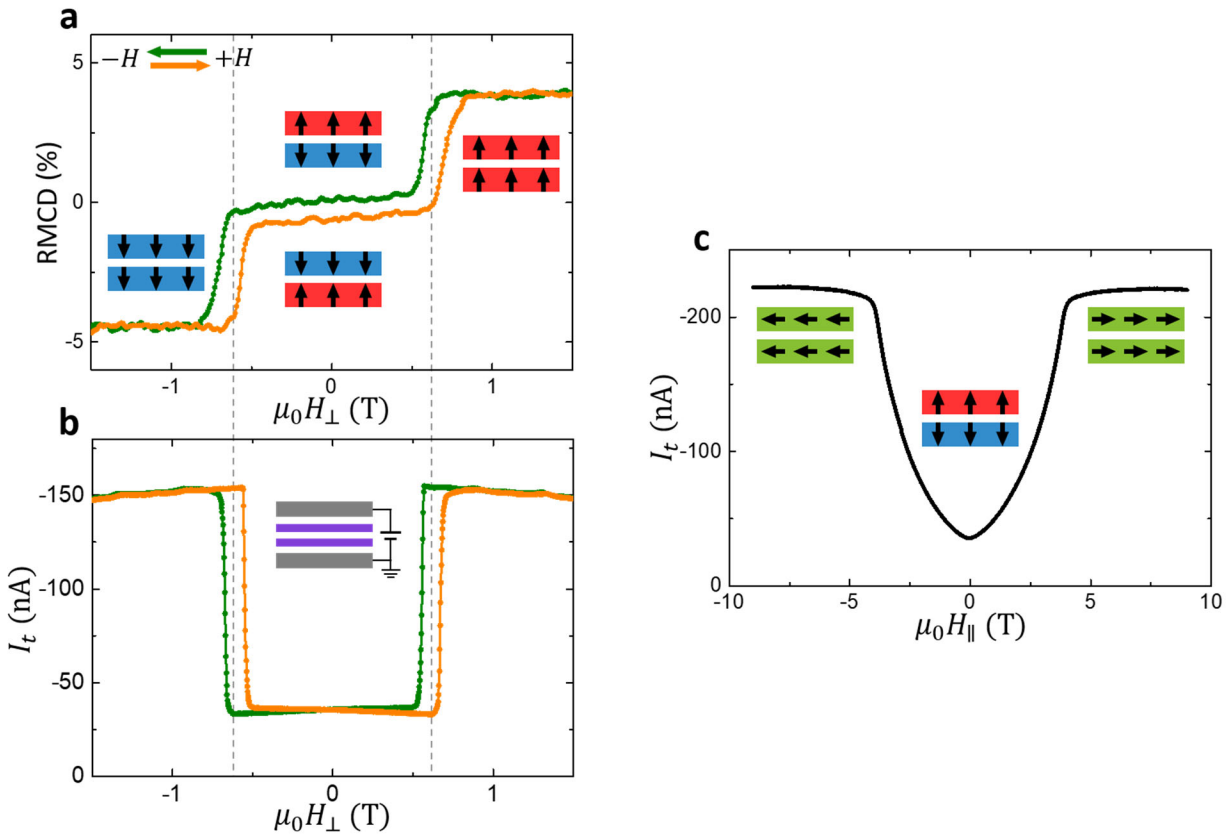

Figure 3. 6. TMR effect in bilayer CrI_3 spin-filter magnetic tunnel junction. (**a**) RMCD signal as a function of out-of-plane magnetic field measured at zero bias voltage. Green (orange) curve corresponds to decreasing (increasing) magnetic field. Insets show the corresponding magnetic states. (**b**) Tunneling current as a function of out-of-plane magnetic field measured at a selected bias voltage (-290 mV). Inset shows the measurement geometry. (**c**) Tunneling current as a function of in-plane magnetic field measured at the same bias voltage (-290 mV). Insets show the corresponding magnetic states. Reproduced from reference[40] with permission.

The direct comparison of the tunneling current and RMCD signals provides a natural explanation of the large TMR effect. For either the ↑↓ or ↑↓ state at low magnetic fields, the tunneling current is small because spin-conserving tunneling of an electron through the two layers in sequence is suppressed. The sharp jump in the tunneling current occurs when the magnetic field drives the bilayer into the ↑↑ and ↓↓ states, and this suppression is removed. This can be understood as the double spin-filtering effect, which produces the large TMR effect observed in bilayer CrI_3 spin-filter MTJ.

We quantify the TMR ratio by $(R_{ap} - R_p)/R_p$, where R_{ap} and R_p are the DC resistances measured at a given bias with anti-parallel and parallel spin alignment in bilayer CrI_3, respectively. Figure 3.5b shows the TMR ratio as a function of bias voltage for out-of-plane and in-plane magnetic fields calculated from the I_t-V curves in Fig. 3.5a. The peak TMR ratio achieved is about 310% and 530% for out-of-plane and in-plane magnetic fields, respectively.

The fact that the TMR ratio for in-plane magnetization is larger than for out-of-plane magnetization implies anisotropic magnetoresistance, which is a common feature in ferromagnets[64] and is a sign of anisotropic spin-orbit coupling stemming from the layered structure of CrI_3. The TMR ratio is peaked at a certain bias and also asymmetric between positive and negative bias voltage. These observations are similar to the spin-filter MTJs based on EuS thin films, where the asymmetry is caused by the different thickness and coercive fields of the two EuS spin-filters[55]. Similarly, the asymmetric TMR ratio implies that the device lacks up-down symmetry, which can be possibly broken during the fabrication process, such as the asymmetry induced by the top and bottom few-layer graphene contacts and hBN flakes. This broken symmetry can manifest the finite non-zero RMCD signals at zero magnetic field in Fig. 3.6a, which has been discussed in detail in Section 2.5.

To further investigate magnetic anisotropy, we measure the tunneling current as a function of in-plane magnetic field measured. As shown in Fig. 3.6c, the tunneling current is smallest at zero magnetic field, and smoothly increases with the magnitude of the in-plane magnetic field. This behavior can be naturally interpreted as a spin-canting effect. When the magnitude of the in-plane magnetic field exceeds about 4 T, the magnetizations are completely aligned in the in-plane direction, and thus the tunneling current saturates. The magnetic anisotropy field can be estimated to be ~3.8 T[40], which is much larger than the out-of-plane critical magnetic field of about ±0.6 T as shown in Fig. 3.6a. These observations, therefore, demonstrate a large out-of-plane magnetic anisotropy in bilayer CrI_3.

3.4 GIANT TUNNELING MAGNETORESISTANCE IN FEW-LAYER CrI_3 MAGNETIC TUNNEL JUNCTIONS

We next investigate the trilayer and four-layer CrI_3 cases. Figures 3.7a and b show the RMCD signal and tunneling current, respectively, as a function of out-of-plane magnetic field measured from a trilayer CrI_3 spin-filter MTJ device. There are mainly four plateaus in the RMCD signal (-14%, -5%, 5%, and 15%), and the ratio between them is close to -3:-1:1:3. Based on the layered antiferromagnetism of trilayer CrI_3 we have discussed in detail in Chapter 2, we can identify the magnetic ground state of the trilayer CrI_3 as either ↑↓↑ or ↓↑↓ at zero magnetic field. As a result, we observe that the RMCD signal at zero magnetic field is about 1/3 of the saturated magnetization of the fully spin-polarized states (↑↑↑ and ↓↓↓).

Resembling the bilayer case, the ↑↓↑ and ↓↑↓ states function as three oppositely aligned spin filters in series, which suppress the tunneling current and correspond to the small current plateau at low magnetic fields. Applying high enough magnetic fields drive the trilayer into the fully spin-polarized states (↑↑↑ and ↓↓↓), which enhance the electron tunneling and correspond

to the large current plateaus at high magnetic fields, as shown in Fig. 3.7b. Similarly, Fig. 3.7c shows the TMR ratio as a function of bias voltage for out-of-plane and in-plane magnetic fields calculated from the I_t-V curves in the inset. The peak TMR ratio achieved is about 2,000% and 3,200% for out-of-plane and in-plane magnetic fields, respectively, revealing a drastically enhanced TMR effect compared to the bilayer devices.

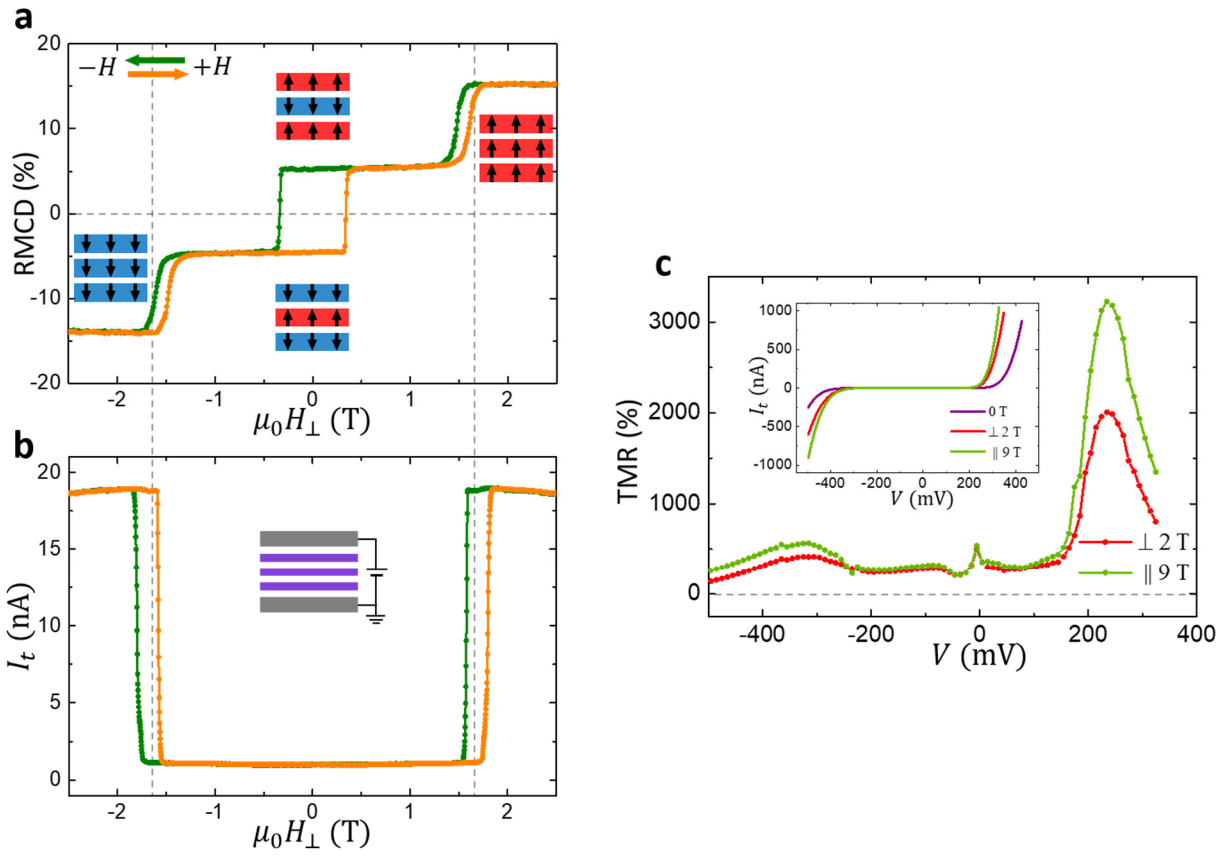

Figure 3. 7. Large TMR effect in trilayer CrI_3 spin-filter magnetic tunnel junction. (**a**) RMCD signal as a function of out-of-plane magnetic field measured at zero bias voltage. Green (orange) curve corresponds to decreasing (increasing) magnetic field. Insets show the corresponding magnetic states. (**b**) Tunneling current as a function of out-of-plane magnetic field measured at a selected bias voltage. Inset shows the measurement geometry. (**c**) TMR ratio as a function of bias voltage for out-of-plane and in-plane magnetic fields, calculated from the I_t-V curves in the inset. Reproduced from reference[40] with permission.

Increasing the CrI_3 thickness beyond three layers can unlock more complicated magnetic states, so we investigate the four-layer CrI_3 case. Figures 3.8a and b show the RMCD signal and tunneling current, respectively, as a function of out-of-plane magnetic field measured from a four-layer CrI_3 spin-filter MTJ device. There are multiple plateaus in both RMCD signal and tunneling current, signifying several magnetic states with distinct effects on the electron tunneling. According to the layered antiferromagnetism of four-layer CrI_3 we have discussed in detail in Chapter 2, the small RMCD signal at low magnetic fields (below ~0.8 T) corresponds to the magnetic ground state of four-layer CrI_3 (either ↑↓↑↓ or ↓↑↓↑). We observe finite non-zero RMCD signals at zero magnetic field, which is very similar to the bilayer case. This can be explained as a result of the broken up-down symmetry, which has been discussed in detail in Section 2.5. As expected for the electron tunneling, these fully antiferromagnetic states are very effective at suppressing the tunneling current since these magnetic states function as four oppositely aligned spin filters in series, which lead to the very small current plateau at low magnetic fields as shown in Fig. 3.8b.

Applying high enough magnetic fields drive the four-layer into the fully spin-polarized states (↑↑↑↑ and ↓↓↓↓), which enhance the electron tunneling and correspond to the large current plateaus and also the large RMCD signal plateaus at high magnetic fields, as shown in Fig. 3.8a and b. Similarly, Fig. 3.8c shows the TMR ratio as a function of bias voltage for out-of-plane and in-plane magnetic fields calculated from the I_t-V curves in the inset. The peak TMR ratio achieved is about 8,600% and 19,000% for out-of-plane and in-plane magnetic fields, respectively, representing a further enhancement of the TMR effect compared to the bilayer and trilayer cases.

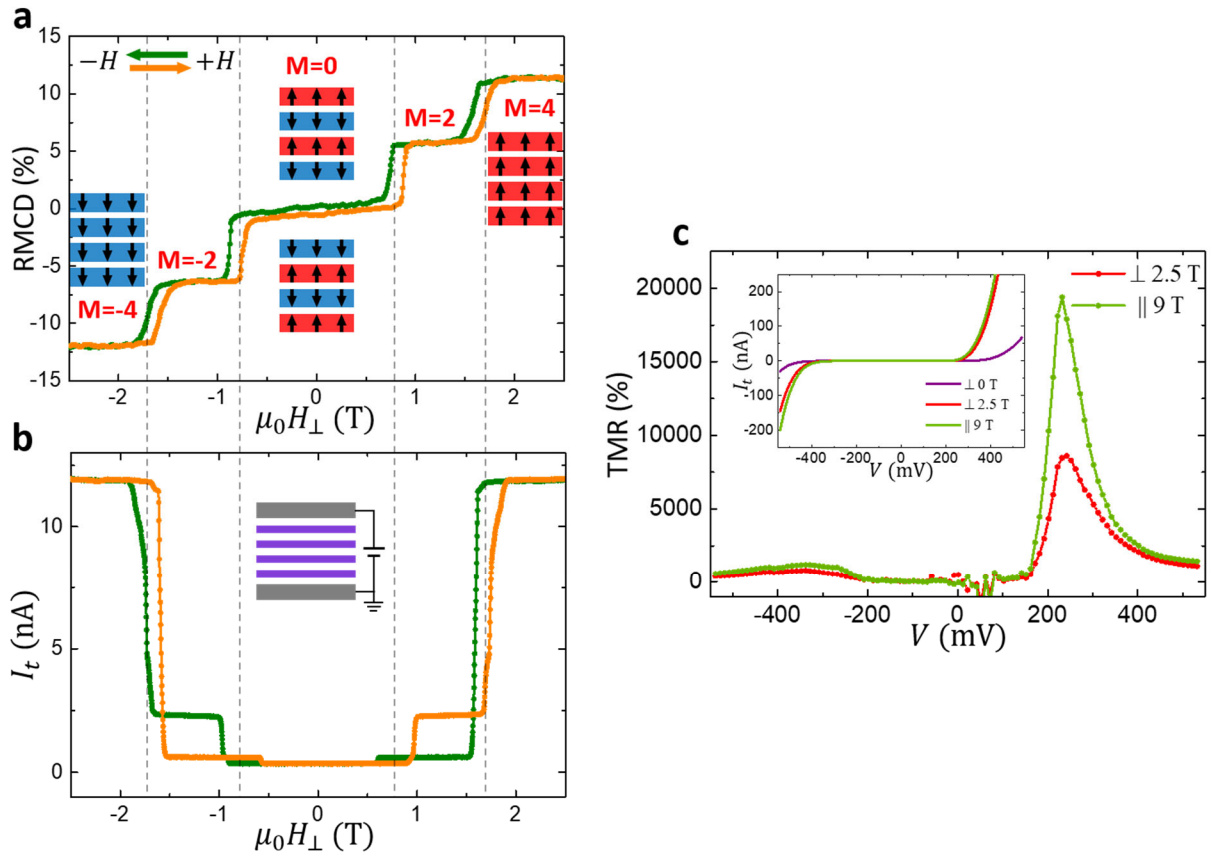

Figure 3. 8. Giant TMR effect in four-layer CrI_3 spin-filter magnetic tunnel junction. (**a**) RMCD signal as a function of out-of-plane magnetic field measured at zero bias voltage. Green (orange) curve corresponds to decreasing (increasing) magnetic field. Insets show the corresponding magnetic states. The relative net magnetizations for different magnetic states are labeled. (**b**) Tunneling current as a function of out-of-plane magnetic field measured at a selected bias voltage. Inset shows the measurement geometry. (**c**) TMR ratio as a function of bias voltage for out-of-plane and in-plane magnetic fields, calculated from the I_t-V curves in the inset. Reproduced from reference[40] with permission.

Distinct from the bilayer and trilayer case, the RMCD signal of four-layer CrI_3 also shows additional intermediate plateaus at about half the RMCD signal of the fully spin-polarized states. As we have discussed in detail in Section 2.4, these observations imply that the corresponding magnetic states have half the net magnetization of the fully spin-polarized states. If we assume that

the saturation magnetization of monolayer CrI_3 is M_s, the net magnetizations of the ↑↓↑↓, ↓↑↓↑, ↑↑↑↑ and ↓↓↓↓ states will be ±0 M_s and ±4 M_s, respectively, which have been labeled in Fig. 3.8a. For the intermediate plateaus, the net magnetizations of the corresponding magnetic states should be ±2 M_s, which should have one layer polarized opposite to the other three. As a result, there are four possible magnetic states for the intermediate plateau at positive magnetic field, {↑↓↑↑, ↑↑↓↑, ↓↑↑↑, ↑↑↑↓}, and the four time-reversal copies, {↓↑↓↓, ↓↓↑↓, ↑↓↓↓, ↓↓↓↑}, are for the intermediate plateau at negative magnetic field, as shown in Fig. 3.9.

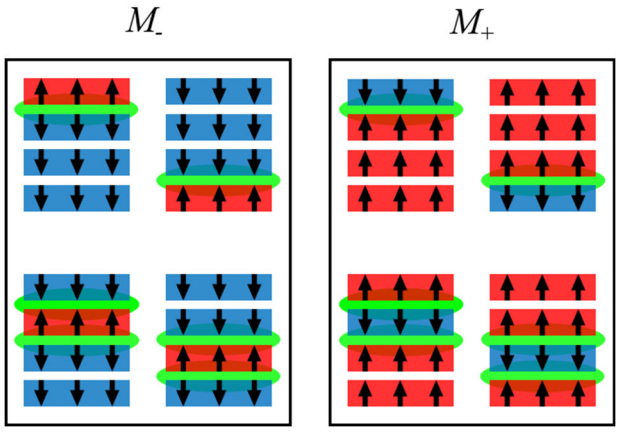

Figure 3. 9. Schematic of possible magnetic states corresponding to the intermediate plateaus at negative and positive magnetic fields. Green lines show the current blocking interfaces. Reproduced from reference[40] with permission.

Although these possible magnetic states should be indistinguishable in the RMCD signal due to the same net magnetization, the tunneling current is likely to be sensitive to the position of the one layer with the minority magnetization. First, the ↓↑↑↑ and ↑↑↑↓ states have only one current blocking interface, whereas the ↑↓↑↑ and ↑↑↓↑ states have two current blocking interfaces, which are shown by the green lines between adjacent layers with opposite magnetizations in Fig. 3.9. Second, the tunneling current direction may also introduce distinct spin-filtering effects either between the ↑↓↑↑ and ↑↑↓↑ states or between the ↓↑↑↑ and ↑↑↑↓

states. As shown in Fig. 3.8b, the tunneling current indeed exhibits multiple plateaus at the intermediate magnetic field range for decreasing and increasing magnetic fields. Furthermore, Fig. 3.10 shows that two additional four-layer CrI_3 spin-filter MTJ devices exhibit distinct behaviors, which have three and one intermediate plateaus, rather than two in Fig. 3.8b. This observed sample dependence suggests that these intermediate magnetic states are sensitive to the environment of the CrI_3 flake, which can be potentially controlled by external stimuli, for example, electrostatic gating. This can realize the electrical control of magnetic states in a voltage-controlled MTJ, which we will discuss in detail in Section 3.5.

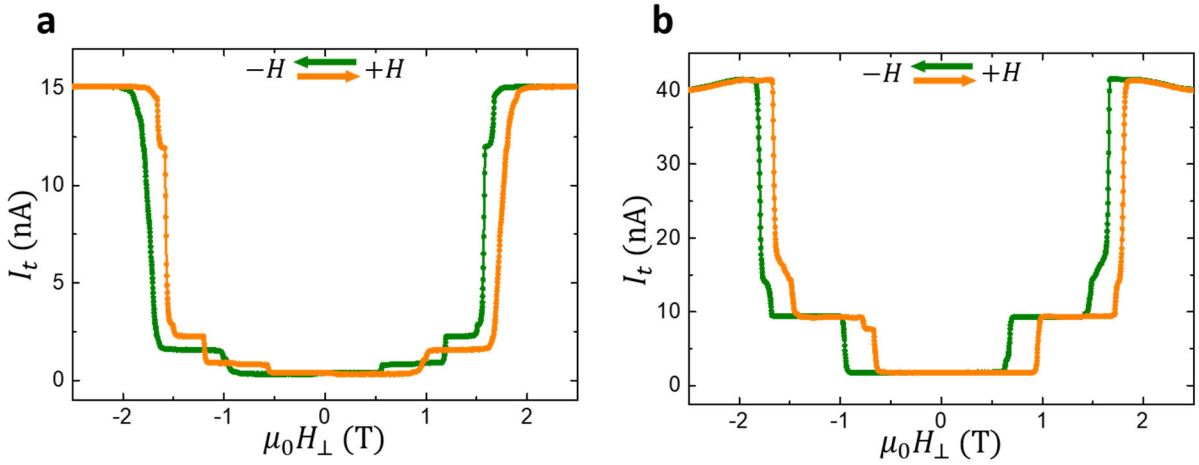

Figure 3. 10. Two additional four-layer CrI_3 spin-filter magnetic tunnel junction devices exhibit three (**a**) and one (**b**) intermediate plateaus. Reproduced from reference[40] with permission.

3.5 Electrical Control of Magnetic States in Four-Layer CrI_3 Magnetic Tunnel Junctions

Electrical manipulation of magnetism is central to spintronics, and voltage-controlled switching between bistable magnetic states can be employed in energy-efficient magnetic memory and logic technologies[65–71]. In this regard, 2D magnets, such as CrI_3, have several advantages to serve as a building block for exploring spintronics in vdW heterostructures. First, the extreme

thinness of few-layer CrI_3 enhances the probability that the 2D magnetism will be amenable to electrical control[72–75]. Second, as we have discussed in detail in this Chapter, the layered antiferromagnetism of CrI_3 naturally functions as a series of spin filters, and their relative alignment can be controlled by a moderate magnetic field. Moreover, as shown in Section 3.4, multiple intermediate magnetic states have been revealed by the electron tunneling in the four-layer CrI_3 spin-filter MTJ devices. This can be potentially controlled by electrostatic gating and realizes the electrical control of magnetic states in a voltage-controlled MTJ[76].

We explore this possibility using a spin-filter MTJ with four-layer CrI_3 tunnel barrier between monolayer graphene contacts, as shown schematically in Fig. 3.11a. This spin-filter MTJ is further encapsulated between two hBN flakes with a graphite top gate (applied voltage V_{tg}) and SiO_2/Si substrate used as a bottom gate (applied voltage V_{bg}). The monolayer graphene contacts combine a low density of states with high carrier mobility, allowing much stronger electrostatic gating effects than using conventional metal electrodes in a vertical junction structure. Figure 3.11b shows an optical microscope image of the dual-gated four-layer CrI_3 spin-filter MTJ device.

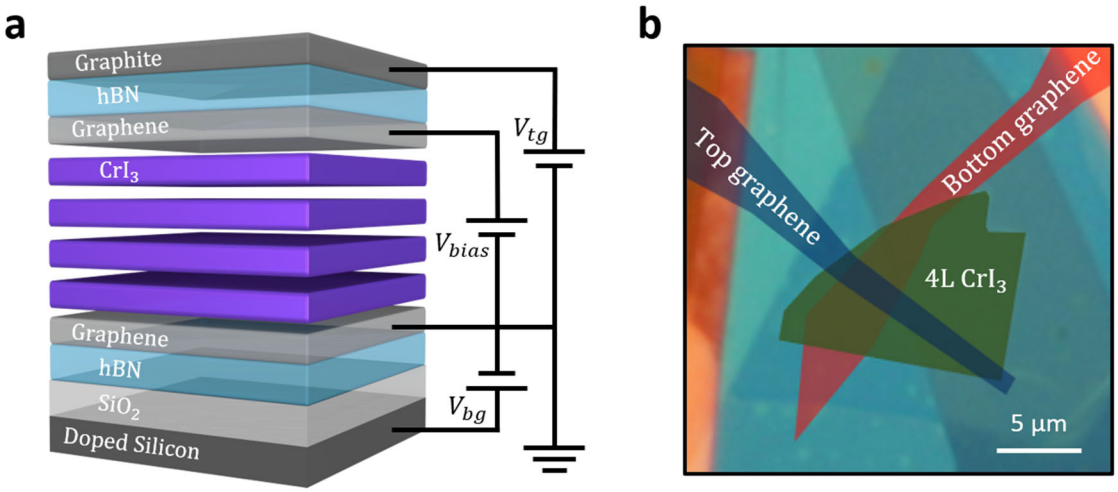

Figure 3. 11. Four-layer CrI_3 spin-filter magnetic tunnel junction. (**a**) Schematic of the dual-gated four-layer CrI_3 spin-filter magnetic tunnel junction device including two monolayer graphene contacts and top and bottom gates. (**b**) False-color optical microscope image of the dual-gated

four-layer CrI_3 spin-filter magnetic tunnel junction device. Reproduced from reference[76] with permission.

We first measure the dual-gated four-layer CrI_3 spin-filter MTJ device at zero top and bottom gate voltages. Figures 3.12a and b show the RMCD signal and tunneling current, respectively, as a function of out-of-plane magnetic field, which exhibit the typical four-layer CrI_3 behaviors, consistent with the previous three four-layer CrI_3 devices we have discussed in detail in Section 3.4. The magnetic ground state (either ↑↓↑↓ or ↓↑↓↑) and the fully spin-polarized states (↑↑↑↑ and ↓↓↓↓) are identified at low magnetic fields (<0.7 T) and high magnetic fields (>2 T). Since the behavior is essentially symmetric for the positive and negative magnetic fields, we focus on the positive magnetic fields in the following discussion. As we have discussed in detail in Section 3.4, at positive intermediate magnetic fields (between 0.9 T and 1.7 T), there are four possible magnetic states for the intermediate RMCD signal plateau, {↑↓↑↑, ↑↑↓↑, ↓↑↑↑, ↑↑↑↓}. Among these magnetic states, the first two have two antiparallel interfaces, while the last two have only one such interface. Since antiparallel interfaces are favored by the antiferromagnetic interlayer coupling, the first two should have lower energy than the last two at intermediate magnetic fields. Therefore, we expect the intermediate magnetic state to be either ↑↓↑↑ or ↑↑↓↑, not ↓↑↑↑ and ↑↑↑↓, and these two magnetic states should be degenerate and indistinguishable if the two internal layers are equivalent, which is the case for symmetric four-layer CrI_3.

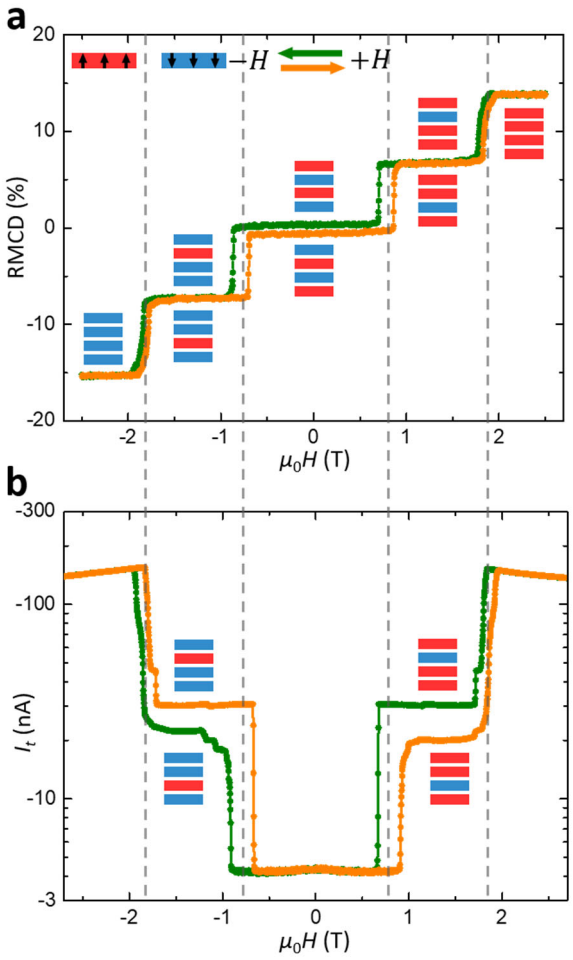

Figure 3. 12. Multiple magnetic states in four-layer CrI_3 spin-filter magnetic tunnel junction. (**a**) RMCD signal as a function of out-of-plane magnetic field measured at zero bias and gate voltages. Green (orange) curve corresponds to decreasing (increasing) magnetic field. Insets show the corresponding magnetic states. (**b**) Tunneling current as a function of out-of-plane magnetic field measured at a selected bias voltage and zero top and bottom gate voltages. Insets show the identified magnetic states for the larger and smaller current plateaus. Reproduced from reference[76] with permission.

If a bias voltage is applied either across the CrI_3 junction or between the top and bottom gates, the induced electric field can lift the symmetry between the ↑↓↑↑ and ↑↑↓↑ states, and these two states may thus respond differently to the bias voltage, which is expected to yield distinct

electron tunneling. Figure 3.12b shows the tunneling current as a function of out-of-plane magnetic field measured at a selected bias voltage (-240 mV) and zero top and bottom gate voltages. By comparing with the RMCD signal, we find that there are two distinct plateaus in the tunneling current at intermediate magnetic fields, which corresponds to only one plateau in the RMCD signal, resembling one of the previous three four-layer CrI_3 devices we have discussed in detail in Section 3.4. These two current plateaus should correspond to the ↑↓↑↑ and ↑↑↓↑ states, revealing that the tunneling current is indeed sensitive to the position of the one layer with the minority magnetization, which is possibly due to the multiple spin-filtering effects. By modeling the system as a set of coupled magnetic quantum wells[40,76], we can calculate and compare the tunneling current for the ↑↓↑↑ and ↑↑↓↑ states, and thus identify the magnetic states of the larger and smaller current plateaus, as shown in Fig. 3.12b. We also conclude that the magnetic state is bistable, which remains in either one of the two intermediate magnetic states when the magnetic field is fixed at the intermediate magnetic field range.

The main goal of this Section is to realize the electrical control of these bistable magnetic states by applying a gate voltage. Figures 3.13a and c show the tunneling current as a function of out-of-plane magnetic field measured at V_{tg} = -2.4 V and +2.4 V, respectively, for the same selected bias voltage (-240 mV). In contrast to the two bistable intermediate current plateaus at zero gate voltage in Fig. 3.12b, only one larger (smaller) current plateau is observed at V_{tg} = -2.4 V (+2.4 V), and the corresponding intermediate magnetic states are similarly identified and indicated by the insets[76]. These observations suggest that the applied positive and negative gate voltages cause the ↑↓↑↑ and ↑↑↓↑ states to be preferred, respectively, demonstrating the electrical control of the two bistable magnetic states.

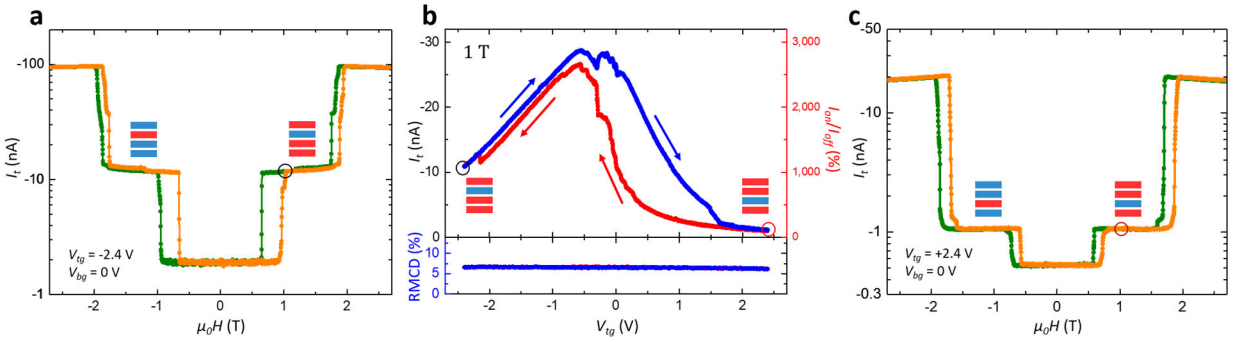

Figure 3. 13. Reversible switching of the bistable magnetic states. (**a**) and (**c**) Tunneling current (V = -240 mV) as a function of out-of-plane magnetic field measured at two representative gate voltages. The identified intermediate magnetic states are indicated by the insets. Green (orange) curve corresponds to decreasing (increasing) magnetic field. (**b**) Tunneling current and the extracted current on/off ratio as a function of the top gate voltage swept from +2.4 V to -2.4 V (red curve) and back to +2.4 V (blue curve) measured at 1 T. The black and red open circles denote the two ends of the top gate voltage sweep, corresponding to the same states circled in (a) and (c), respectively. The bottom panel shows almost no change in RMCD signal during the top gate voltage sweep, consistent with the same magnetization of the bistable magnetic states. Reproduced from reference[76] with permission.

Remarkably, reversible switching between the two magnetic states can be achieved purely by sweeping the gate voltage. Figure 3.13b shows the tunneling current as a function of the top gate voltage swept from +2.4 V to -2.4 V and back to +2.4 V measured at 1 T, revealing the reversible switching between the two bistable magnetic states which are identified and indicated by the black and red open circles in Fig. 3.13a and c. Meanwhile, the bottom panel of Fig. 3.13b shows almost no change in RMCD signal during the top gate voltage sweep, which is expected since the two intermediate magnetic states have the same net magnetization. The general changes in the tunneling current with increasing the magnitude of the top gate voltage are possibly associated with the doping effects on the monolayer graphene contacts. Moreover, the tunneling

current exhibits a pronounced hysteresis loop and small wiggles during the top gate voltage sweep, which can be attributed to the transition between the two bistable magnetic states and the associated domain effects. The difference of the tunneling current for the two bistable magnetic states during the top gate voltage sweep can be as large as a factor of ten, which is revealed by the extracted current on/off ratio in Fig. 3.13b.

In conclusion, we investigate a pair of bistable magnetic states in four-layer CrI_3 which can be switched reversibly by sweeping gate voltage in a dual-gated spin-filter magnetic tunnel junction device, demonstrating a new kind of voltage-controlled vdW spintronic devices.

Chapter 4. PRESSURE CONTROL OF INTERLAYER MAGNETISM IN ATOMICALLY THIN CrI_3

In Chapter 4, we will realize the pressure control of interlayer magnetism in atomically thin CrI_3. We will first discuss the crystal structure of CrI_3 with a focus on layer stacking, and consider the stacking-dependent magnetism. We will then demonstrate the pressure control of interlayer magnetism in bilayer CrI_3, and present the switching of magnetic states via pressure tuning of layer stacking. We will also investigate the coexisting domains of magnetic and layer stacking phases in trilayer CrI_3.

4.1 STACKING-DEPENDENT INTERLAYER MAGNETISM IN ATOMICALLY THIN CrI_3

In a vdW material, a relative lateral shift or a change in interlayer spacing between two adjacent layers can cause a drastic modulation of its physical properties. In particular, for 2D magnets, the interlayer atomic registry strongly modifies the interlayer exchange interactions, which can lead to a change in the magnitude and sign of the interlayer exchange coupling. Here, we take atomically thin CrI_3 as an excellent example to explore the physical origin of its interlayer magnetism. Figure 4.1 shows two isolated free monolayer CrI_3, which are not coupled with each other. When the two layers are brought together, they will be held together by vdW forces, where the vdW gap and the antiferromagnetic interlayer exchange coupling are formed. The main mechanism for the interlayer exchange interactions is the super-superexchange coupling, which can be described by the virtual electron hopping between the Cr *d* orbitals through the *p* orbitals of the two I atoms between the vdW gap[77–80]. The virtual electron hopping in this interlayer exchange coupling mechanism depends on the interlayer atomic registry which is determined by

the layer stacking, and thus possibly leads to the stacking-dependent interlayer magnetism in 2D magnets[81–84].

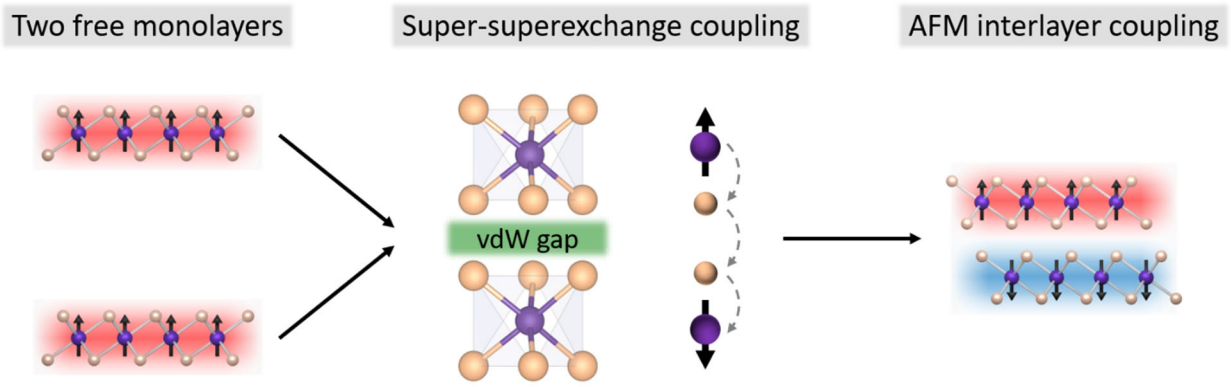

Figure 4. 1. Interlayer super-superexchange coupling in bilayer CrI_3.

For atomically thin CrI_3, the layer stacking and the corresponding interlayer coupling have been predicted by calculating the stacking energy and the interlayer exchange energy, respectively[77–80]. Figure 4.2a shows the two stable layer stacking in bilayer CrI_3, rhombohedral (AB) and monoclinic (AB'), which are at the global minimum and a local minimum for stacking energy, respectively, and are nearly degenerate. The corresponding interlayer coupling can be determined by calculating the interlayer exchange energy as a function of layer shift, as shown in Fig. 4.2b and c. The rhombohedral and monoclinic stacking is predicted to favor ferromagnetic and antiferromagnetic interlayer coupling, respectively, and thus leads to the distinct magnetic ground states in Fig. 4.2a, revealing the possible stacking-dependent interlayer magnetism in CrI_3.

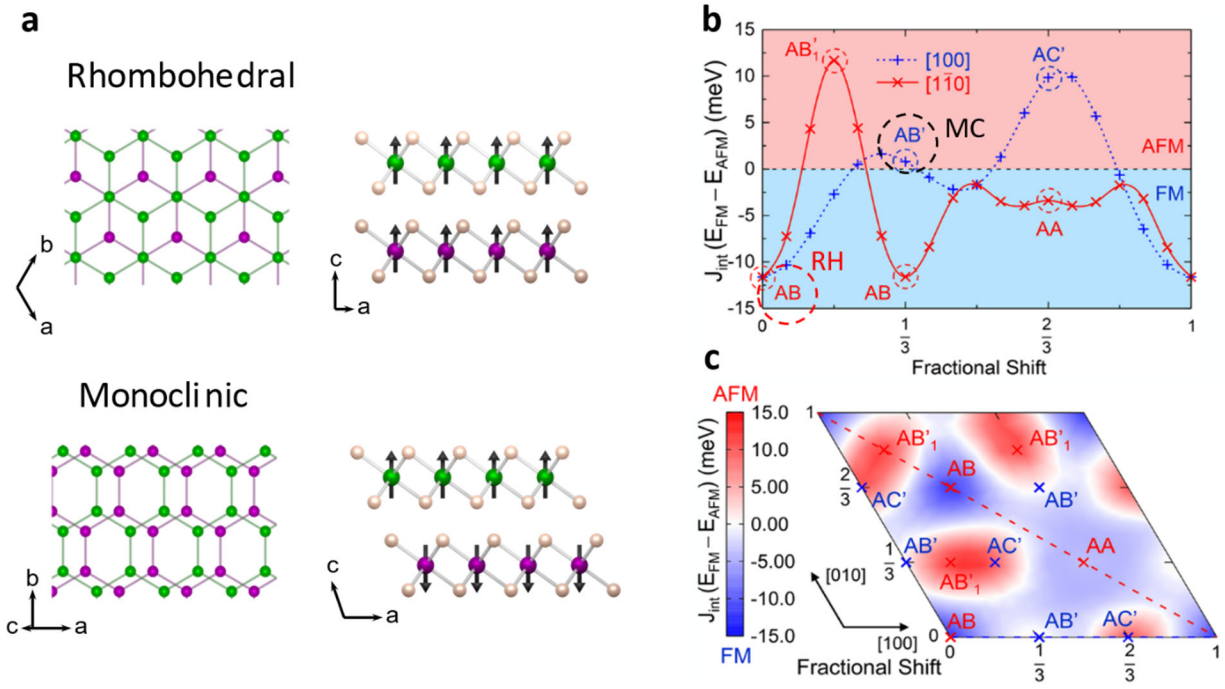

Figure 4. 2. Stacking-dependent interlayer magnetism in bilayer CrI_3. (**a**) Schematic of rhombohedral and monoclinic stacking with the top (left) and side view (right) indicating the ferromagnetic and antiferromagnetic interlayer coupling, respectively. The green (purple) atoms represent the Cr atoms in the top (bottom) layer while the brown ones represent the I atoms. Here, a, b and c represent the CrI_3 crystal axes. (**b**) Interlayer exchange energy as a function of lateral shift. The red and black open circles denote the rhombohedral and monoclinic stacking, corresponding to the ferromagnetic and antiferromagnetic interlayer coupling, respectively. (**c**) Full map of lateral shifts for the interlayer exchange energy. Reproduced from reference[79,81] with permission.

This stacking-dependent interlayer magnetism can explain the discrepancy of interlayer magnetism between the exfoliated CrI_3 and bulk CrI_3 crystal we mentioned in Chapter 2, which exhibits antiferromagnetic interlayer coupling in atomically thin CrI_3 but simply ferromagnetism in bulk CrI_3 crystal. We first take a closer look at the layer stacking of bulk CrI_3 crystal. At high temperatures (above 220 K), the layer stacking of bulk CrI_3 crystal is monoclinic ($C2/m$), which undergoes a structural transition near 210-220 K and becomes rhombohedral ($R\bar{3}$) at low

temperatures[37]. As a result, the ferromagnetism observed in bulk CrI_3 crystal should correspond to the rhombohedral stacking at low temperatures, consistent with the theoretical predictions. However, this structural transition is usually absent in exfoliated few-layer CrI_3, and thus the exfoliated CrI_3 is essentially pinned in the layer stacking at high temperatures and remains to be monoclinic stacking at low temperatures, which has been demonstrated by the recent second harmonic generation measurements[85]. Therefore, the unexpected layered antiferromagnetism observed in atomically thin CrI_3 should correspond to the monoclinic stacking pinned at low temperatures, which is also in good agreement with the theoretical predictions and explains the discrepancy of interlayer magnetism between the exfoliated CrI_3 and bulk CrI_3 crystal.

These observations demonstrate the stacking-dependent interlayer magnetism in CrI_3 and highlight the opportunities to control the magnetic order in CrI_3 by tuning the layer stacking, for example, reducing the interlayer spacing by applying pressure or inducing a relative lateral shift between the two CrI_3 layers as shown in Fig. 4.3.

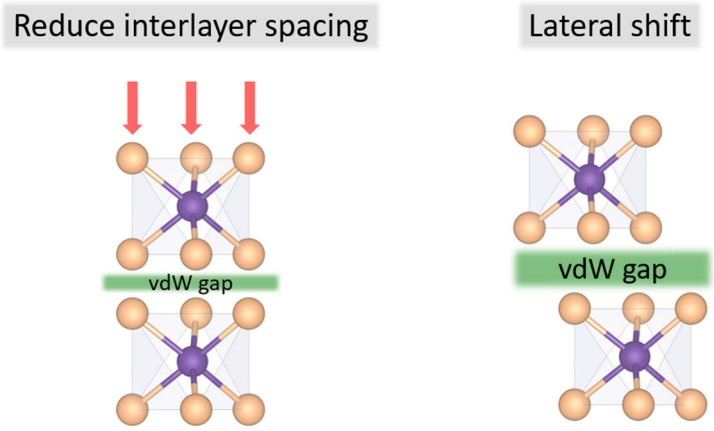

Figure 4. 3. Tuning the layer stacking in bilayer CrI_3 by applying pressure to reduce the interlayer spacing or inducing a relative lateral shift between the two CrI_3 layers.

4.2 PRESSURE CONTROL OF INTERLAYER MAGNETISM

Hydrostatic pressure can be used to continuously control the interlayer coupling by tuning the interlayer spacing in vdW crystals. This has recently been shown to modify the band structure in graphene/hBN moiré superlattices[86] and transition metal dichalcogenides[87,88], as well as the superconductivity and correlated insulating states in twisted bilayer graphene[89]. Hydrostatic pressure has also been applied to several bulk 2D magnet crystals, successfully altering the critical temperature[90–93]. Considering the stacking-dependent interlayer magnetism in CrI_3, applying hydrostatic pressure can potentially tune the magnetic order in CrI_3 by reducing the interlayer spacing or inducing a relative lateral shift.

Motivated by this idea, we employ a piston-cylinder pressure cell to apply hydrostatic pressure. Figure 4.4a shows a schematic of our experimental setup. In this measurement, we start with the same bilayer CrI_3 spin-filter MTJ device, which consists of a bilayer CrI_3 sandwiched by the top and bottom few-layer graphene contacts. The spin-filter MTJ is further encapsulated between two hBN flakes to avoid degradation. The device is then held in a piston-cylinder pressure cell for applying hydrostatic pressure up to 2.7 GPa. The magnetic order in the bilayer CrI_3 can be probed in situ by measuring the tunneling current as we have discussed in detail in Chapter 3. Here, we note that the pressure of 1 GPa is equivalent to a 10-ton elephant standing on an area of only 1 cm^2, which is really high pressure as shown in Fig. 4.4b. In contrast to the bilayer CrI_3 spin-filter MTJ under ambient conditions in Fig. 4.4c, applying such high pressure can dramatically reduce the interlayer spacing between the two CrI_3 layers as shown in Fig. 4.4d. We note that all the measurements discussed in this Chapter were carried out at a temperature of 2 K with magnetic field in the out-of-plane direction, unless otherwise specified.

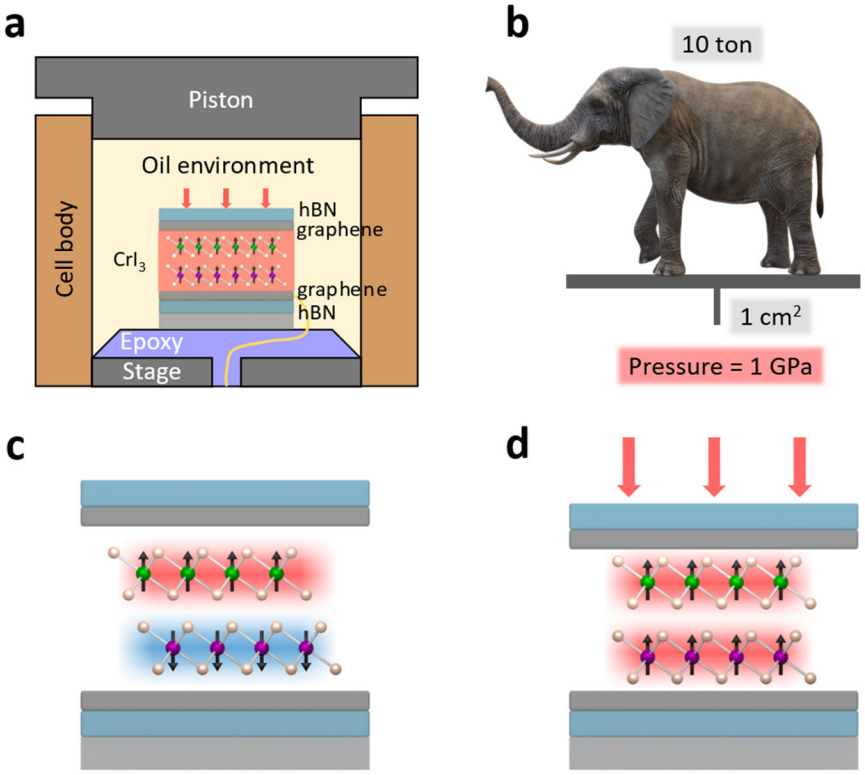

Figure 4. 4. Pressure study of bilayer CrI_3 spin-filter magnetic tunnel junction. (**a**) Schematic of the pressure experimental setup. The bilayer CrI_3 spin-filter MTJ device is held in a piston-cylinder pressure cell for applying hydrostatic pressure. The yellow line embedded in epoxy represents electrical leads. The force applied to the piston exerts hydrostatic pressure on the device through oil (red arrows). (**b**) The pressure of 1 GPa is equivalent to a 10-ton elephant standing on an area of only 1 cm^2, representing high pressure. (**c**) Schematic of bilayer CrI_3 spin-filter magnetic tunnel junction under ambient conditions. (**d**) Applying high pressure can dramatically reduce the interlayer spacing between the two CrI_3 layers. Reproduced from reference[81] with permission.

We start our measurements with the tunneling current measured from the bilayer CrI_3 spin-filter MTJ device. Figure 4.5 shows the tunneling current as a function of magnetic field under ambient conditions and at selected hydrostatic pressure. Under ambient conditions (0 GPa), the tunneling current exhibited the typical bilayer CrI_3 behaviors of the layered antiferromagnetism. At low magnetic fields (below ~0.6 T), the layered antiferromagnetic ground state (↑↓ or ↑↓)

serves as two spin filters in antiparallel alignment which suppresses the tunneling current and corresponds to the small current plateau. When the magnetic field exceeds the critical magnetic field of bilayer CrI_3, the spin-flip transition happens, corresponding to the sharp jump in the tunneling current. At high magnetic fields (above ~0.8 T), the large current plateaus correspond to the fully spin-polarized states (↑↑ and ↓↓).

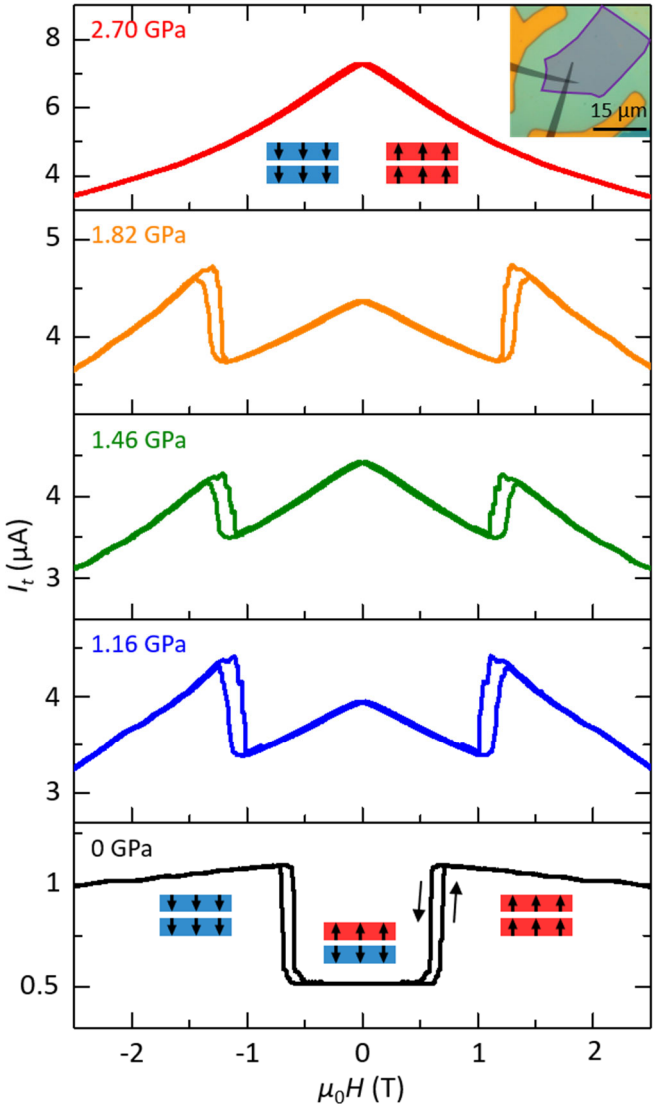

Figure 4. 5. Tunneling current as a function of magnetic field under ambient conditions and at selected hydrostatic pressure measured at the same bias voltage (50 mV). Insets show the corresponding magnetic states and the optical microscope image of the bilayer CrI_3 spin-filter MTJ

device. The purple and gray shadows show the bilayer CrI_3 flake and few-layer graphene contacts. The yellow and green regions are gold electrodes and hBN flakes. Reproduced from reference[81] with permission.

As the pressure is increased, we observe that the sharp jumps in the tunneling current gradually expand to the two sides as shown in Fig. 4.5. This reveals that the critical magnetic field for the spin-flip transition rises dramatically to above 1.3 T, which is more than twice the value at zero pressure. Such an enhancement of the critical magnetic field can be explained by the reduced interlayer spacing, which increases the wavefunction overlap and thus the strength of the interlayer exchange interactions. As a result, it requires higher external magnetic field to overcome the stronger antiferromagnetic interlayer coupling, corresponding to a higher critical magnetic field. The tunneling current also increases substantially with pressure owing to the reducing interlayer spacing, which favors the electron tunneling through the tunnel barrier. We also note that the steady background in the tunneling current decreases as magnetic field increases, which can be attributed to the positive magnetoresistance in the few-layer graphene contacts[94]. This magnetoresistance background becomes more noticeable as the tunneling magnetoresistance of the CrI_3 is reduced at higher pressure.

4.3 SWITCHING MAGNETIC STATES VIA PRESSURE TUNNING OF LAYER STACKING

Interestingly, the sharp jumps in the tunneling current are absent at the highest pressure of 2.7 GPa, and only the magnetoresistance background from the few-layer graphene contacts remains. We note that this is not because the critical magnetic field moves out of the applied magnetic field range. This observation implies that the interlayer coupling of the bilayer CrI_3 has switched from antiferromagnetic at low pressure to ferromagnetic at high pressure.

To support this hypothesis, we perform RMCD measurement to probe the interlayer magnetism of the bilayer CrI_3 under ambient conditions after the device is removed from the pressure cell where it underwent high pressure. Figure 4.6a shows the RMCD signal as a function of magnetic field measured from the bilayer CrI_3 after pressure, which exhibits a single pronounced magnetic hysteresis loop centered at zero magnetic field, the characteristic of ferromagnetism. This is distinct from the typical bilayer CrI_3 behaviors of the layered antiferromagnetism as shown in Fig. 4.6b, revealing that the interlayer coupling of the bilayer CrI_3, and thus the magnetic ground state, has been switched to ferromagnetic. We note that the bilayer CrI_3 remains to be ferromagnetic under ambient conditions after the device is removed from the pressure cell, which indicates that this switching is possibly a result of an irreversible structural transition in the bilayer CrI_3 induced by applying high pressure.

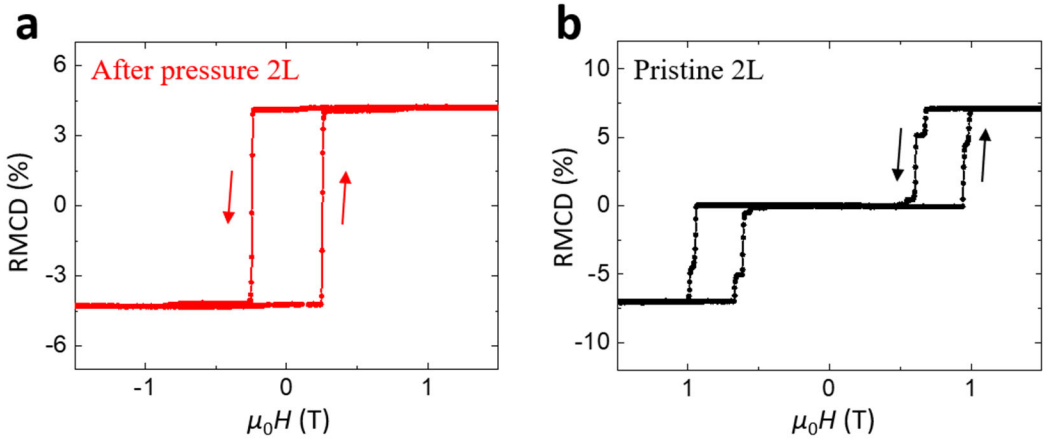

Figure 4. 6. Switching interlayer magnetism in bilayer CrI_3. (**a**) RMCD as a function of magnetic field measured from the bilayer CrI_3 under ambient conditions after the device is removed from the pressure cell where it underwent high pressure. The arrows indicate the sweep direction of the magnetic field. (**b**) RMCD signal as a function of magnetic field measured from a pristine bilayer CrI_3 under ambient conditions, which exhibits the typical bilayer CrI_3 behaviors of the layered antiferromagnetism. The arrows indicate the sweep direction of the magnetic field. Reproduced from reference[81] with permission.

To investigate the possible structural transition in the bilayer CrI_3, we further employ polarization-resolved Raman spectroscopy measurement to identify the crystal structure. We first measure bulk CrI_3 crystal as a reference since the layer stacking of bulk CrI_3 crystal has been identified[37,95–97]. Figures 4.7c and f show the polarization dependence of Raman spectra in the cross-polarization channel measured from a bulk CrI_3 crystal at 270 K and 80 K, which correspond to monoclinic and rhombohedral stacking, respectively. The rhombohedral stacking gives rise to a two-fold degenerate E_g mode, which corresponds to the peak near 105 cm^{-1} in Fig. 4.7f. For the monoclinic stacking, this mode splits into non-degenerate A_g and B_g modes due to a lower symmetry, which leads to the four-fold polarization dependence of this peak observed in Fig. 4.7c. We next utilize this technique to identify the layer stacking of the bilayer CrI_3 after pressure and a pristine CrI_3. Figures 4.7a and d show the polarization dependence of Raman spectra in the cross-polarization channel measured from a pristine bilayer CrI_3 and the bilayer CrI_3 after pressure at 80 K. Figure 4.7a shows that the peak displays a four-fold polarization dependence, which is similar to the bulk CrI_3 crystal at 270 K and thus confirms the layer stacking is monoclinic in a pristine bilayer[85]. In contrast, the four-fold polarization dependence of the peak is absent in the bilayer CrI_3 after pressure, which resembles the bulk CrI_3 crystal at 80 K and reveals that the layer stacking of the bilayer CrI_3 has been switched from monoclinic to rhombohedral by applying high pressure. We also check the Raman spectra at 270 K as shown in Fig. 4.7b and e, which show the same polarization dependence, showing the layer stacking remains the same for different temperatures. These observations demonstrate the stacking-dependent interlayer magnetism in CrI_3 and attribute the switching of interlayer magnetic order to the pressure-induced structural transition.

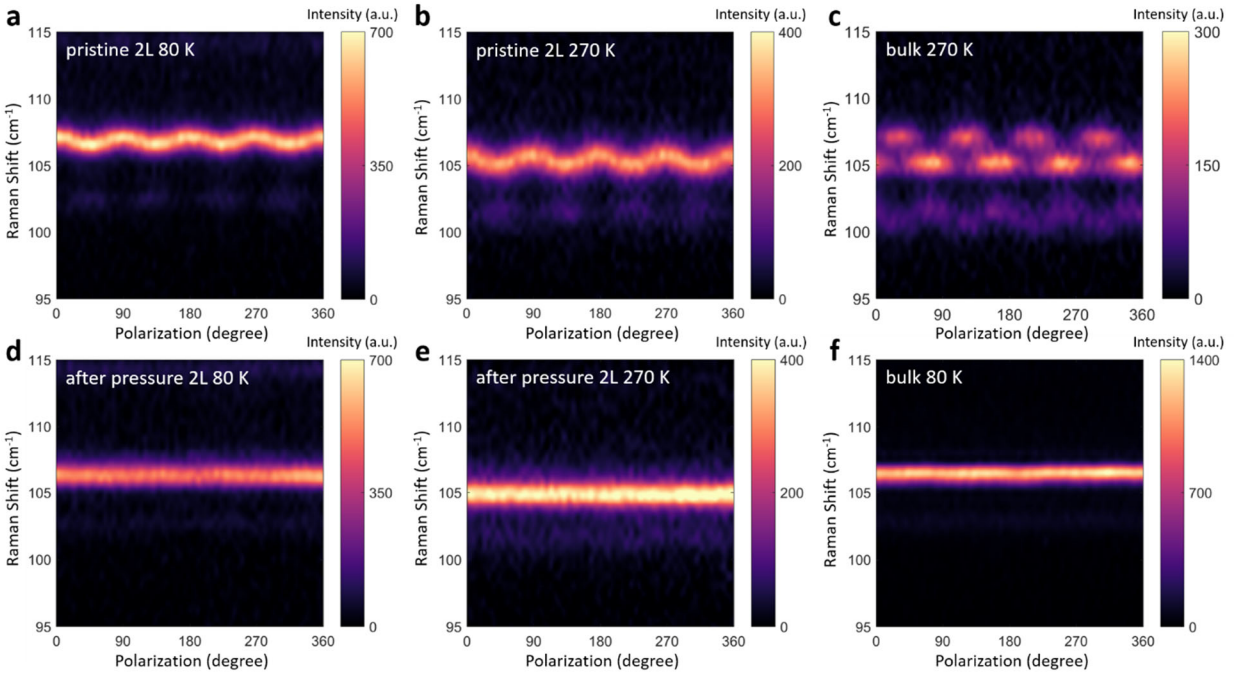

Figure 4. 7. Polarization dependence of Raman spectra for bilayer CrI_3 and bulk CrI_3 crystal. (**a**) and (**d**) Polarization dependence of Raman spectra in the cross-polarization channel measured from a pristine bilayer CrI_3 and the bilayer CrI_3 after pressure at 80 K. The four-fold polarization dependence of the peak near 105 cm^{-1} indicates the monoclinic stacking. The absence of the four-fold polarization dependence indicates the rhombohedral stacking. (**b**) and (**e**) The same measurements at 270 K. (**c**) and (**f**) Polarization dependence of Raman spectra in the cross-polarization channel measured from a bulk CrI_3 crystal at 270 K and 80 K, respectively. Reproduced from reference[81] with permission.

4.4 Magnetic and layer stacking phases in trilayer CrI_3

Having demonstrated the pressure control of interlayer magnetism in bilayer CrI_3, we now consider trilayer CrI_3 case. We fabricate a trilayer CrI_3 spin-filter MTJ device, and similarly measure the tunneling current under ambient conditions and at selected hydrostatic pressure. Figure 4.8 shows the tunneling current as a function of magnetic field measured from the trilayer CrI_3 spin-filter MTJ device. Under ambient conditions (0 GPa), the tunneling current exhibited the

typical trilayer CrI_3 behaviors of the layered antiferromagnetism, as shown in Fig. 4.8a. At low magnetic fields, the magnetic ground state (either ↑↓↑ or ↓↑↓) serves as three spin filters in antiparallel alignment which suppresses the tunneling current and corresponds to the small current plateau. When the magnetic field exceeds the critical magnetic field of trilayer CrI_3, the spin-flip transition happens at ~1.6 T, corresponding to the sharp jump in the tunneling current. At high magnetic fields, the large current plateaus correspond to the fully spin-polarized states (↑↑↑ and ↓↓↓). At a moderate applied pressure of 1.2 Gpa (Fig. 4.8b), the tunneling current behaviors are similar to those at zero pressure, but the critical magnetic field for the spin-flip transition is increased. At the highest pressure of 2.45 GPa (Fig. 4.8c), the critical magnetic field reaches as high as 3.7 T, which is more than twice the value at zero pressure.

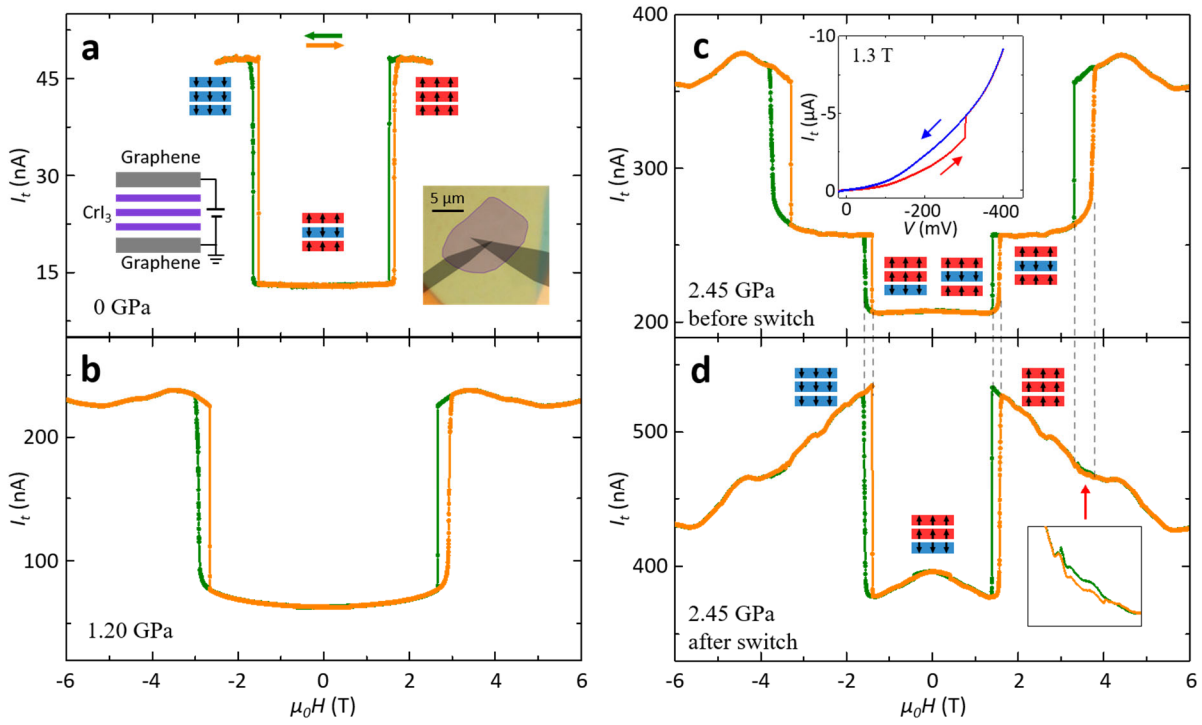

Figure 4. 8. Pressure control of interlayer magnetism in trilayer CrI_3 spin-filter magnetic tunnel junction. (**a**), (**b**) and (**c**) Tunneling current as a function of magnetic field under ambient conditions (a, 0 GPa) and at selected hydrostatic pressure (b, 1.2 GPa) (c, 2.45 GPa) measured at

the same bias voltage (70 mV). Green (orange) curve corresponds to decreasing (increasing) magnetic field. Insets in (a) show the corresponding magnetic states, the measurement geometry (bottom left), and the optical microscope image of the trilayer CrI_3 spin-filter MTJ device (bottom right). The purple and gray shadows show the trilayer CrI_3 flake and few-layer graphene contacts. Insets in (c) show the corresponding magnetic states and the tunneling current measured while sweeping the bias voltage up (red) and down (blue). The sudden jump implies an irreversible change in the device. (**d**) Tunneling current as a function of magnetic field at the highest pressure of 2.45 GPa after the sudden jump. Insets in (d) show the corresponding magnetic states and the zoom-in view of the region indicated by the red arrow. Reproduced from reference[81] with permission.

At high pressure, however, additional features appear which have not been observed in trilayer CrI_3. Figure 4.8c shows the initial tunneling current as a function of magnetic field measured at 2.45 GPa. In addition to the usual small and large current plateaus at low and high magnetic fields, we observe a new intermediate spin-flip transition at ~1.7 T, suggesting another degree of freedom is involved. We then measure the tunneling current as a function of the bias voltage at 1.3 T, as shown in the inset in Fig. 4.8c. When the bias voltage is increased to ~-300 mV (red trace), we observe a sudden jump in the tunneling current to a larger current state. When the bias voltage is then swept back to zero (blue trace), the tunneling current remains in the large current state, indicating an irreversible change in the device. Figure 4.8d shows the tunneling current as a function of magnetic field after the sudden jump measured at 2.45 GPa. Surprisingly, the lower magnetic field transition happens at the same intermediate magnetic field (~1.7 T), but the higher magnetic field transition has disappeared, and the tunneling current at low magnetic fields is more than twice the value before the sudden jump. These observations imply that the sudden jump in the tunneling current is possibly a result of an irreversible structural transition in

the trilayer CrI_3, for example, a change in the layer stacking, resembling the bilayer case we have discussed in detail in Section 4.3.

These observations can be explained naturally as follows. Before the sudden jump, at low magnetic fields, the trilayer CrI_3 contains coexisting domains of two different layered antiferromagnetic phases (AFM I and AFM II), which are associated with the layer stacking domains. The AFM I phase corresponds to the magnetic phase in a pristine trilayer CrI_3, which has two antiferromagnetic interfaces, and thus the magnetic ground state is either ↑↓↑ or ↓↑↓. The AFM II phase is a new magnetic phase, which has one antiferromagnetic and one ferromagnetic interface, and thus the magnetic ground state is either ↑↑↓ or ↓↓↑ (and also possibly either ↓↑↑ or ↑↓↓). This new magnetic phase is possibly a result of a change in the layer stacking from monoclinic to rhombohedral, which only happened at one of the two interfaces and switched the interlayer coupling at this interface from antiferromagnetic to ferromagnetic. In either the AFM I or AFM II phase, as the magnetic field is increased to the critical magnetic field, the Zeeman energy overcomes the antiferromagnetic coupling, which leads to the spin-flip transition. Since the AFM II phase has only one antiferromagnetic interface, it is switched to the fully spin-polarized state at lower magnetic field of 1.7 T, resulting in the new intermediate spin-flip transition. Since the AFM I phase has two antiferromagnetic interfaces, it is switched to the fully spin-polarized state at higher magnetic field of 3.7 T, which is about twice the value for the AFM II phase, corresponding to the spin-flip transition of a pristine trilayer CrI_3 at high pressure. After the sudden jump, the disappearance of the spin-flip transition at 3.7 T implies that the AFM I phase in this domain has been switched to the AFM II phase. We note that the zoom-in view of Fig. 4.8d reveals there remains a tiny magnetic hysteresis loop at 3.7 T, indicating that a small domain of the AFM I phase is still present in this trilayer CrI_3.

To further support this explanation, we employ scanning RMCD microscopy measurement to identify the multiple magnetic phases in the trilayer CrI_3 under ambient conditions after the device is removed from the pressure cell. Figure 4.9a shows the spatial map of the RMCD signal measured at 2 T, which reveals the trilayer CrI_3 region, as well as bilayer CrI_3 and thin bulk CrI_3 regions in the device. Figures 4.9b, c and d show the RMCD signal as a function of magnetic field measured at the three selected positions P, Q, and R. At position P (Fig. 4.9b), the RMCD signal exhibits the typical trilayer CrI_3 behaviors of the layered antiferromagnetism, which is identified as the AFM I phase. At position Q (Fig. 4.9c), near the tunnel junction region, the RMCD signal shows that the spin-flip transition happens at ~0.8 T, which is about half the value for a pristine trilayer CrI_3, which should correspond to the AFM II phase. At position R (Fig. 4.9d), the RMCD signal exhibits a single pronounced magnetic hysteresis loop centered at zero magnetic field, the characteristic of ferromagnetism, which implies that both interfaces in the trilayer CrI_3 are ferromagnetic.

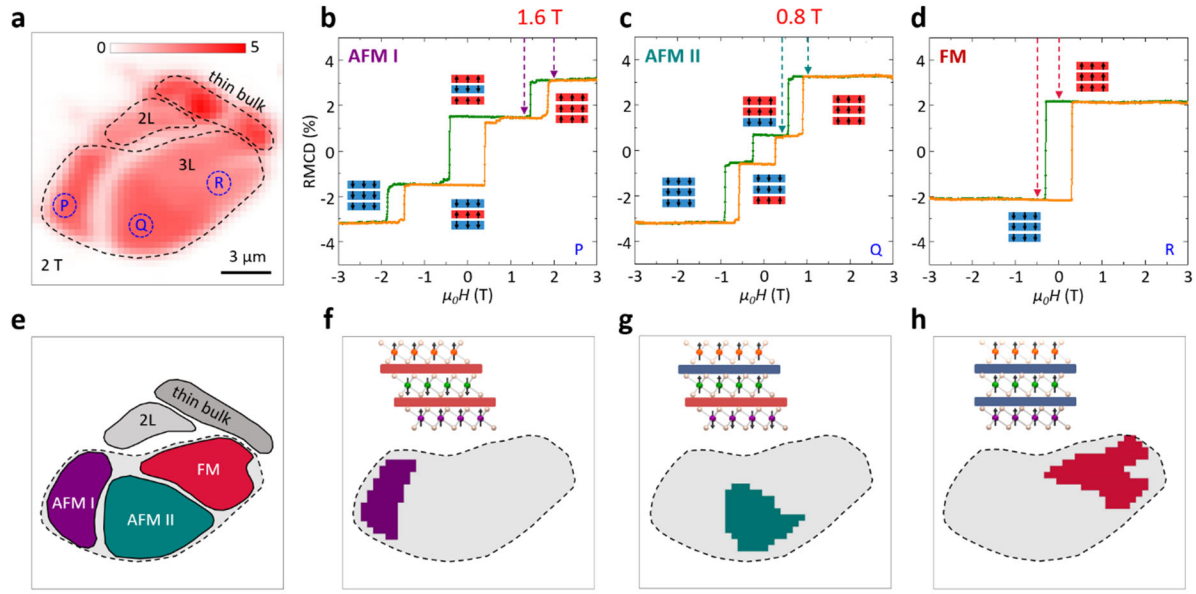

Figure 4. 9. Magnetic and layer stacking phases in trilayer CrI_3. (**a**) Spatial map of RMCD signal at 2 T measured from the trilayer CrI_3 under ambient conditions after the device is removed from

the pressure cell. The trilayer CrI_3, bilayer CrI_3, and thin bulk CrI_3 regions are labeled. (**b**), (**c**) and (**d**) RMCD signal as a function of magnetic field measured at the three selected positions P, Q, and R indicated in (a), which exhibit AFM I, AFM II, and FM phases, respectively. Green (orange) curve corresponds to decreasing (increasing) magnetic field. Insets show the corresponding magnetic states. (**e**) Full map of the multiple magnetic phases. (**b**), (**c**) and (**d**) Maps of the magnetic domains identified by calculating the difference of the RMCD maps at two selected magnetic fields for the AFM I, AFM II, and FM phases. Insets show the corresponding layer stacking and magnetic states. AFM I: two antiferromagnetic interfaces. AFM II: one antiferromagnetic interface and one ferromagnetic interface. FM: two ferromagnetic interfaces. Reproduced from reference[81] with permission.

Furthermore, the different spin-flip transitions can be used to identify the domains of different magnetic phases. For example, when the magnetic field is swept down from 2 to 1.3 T indicated by the purple arrows, only the AFM I phase has a spin-flip transition, which gives a change in the RMCD signal of ~1.3%. Figure 4.9f shows that the AFM I domain can therefore be identified by mapping the RMCD signals at these two magnetic fields and calculating the difference of the two RMCD maps. Similarly, the AFM II and the fully ferromagnetic (FM) domains can be identified by calculating the difference of the two RMCD maps at 1 T and 0.4 T (green arrows), and at 0 T and -0.5 T (red arrows), which are shown in Fig. 4.9g and h, respectively. Figure 4.9e shows the full map of the multiple magnetic phases by putting Fig. 4.9f, g, and h together, revealing the existence of three different magnetic phases in the trilayer CrI_3.

Resembling the bilayer CrI_3 case, the multiple magnetic phases can be attributed to the multiple layer stacking phases, where monoclinic and rhombohedral stacking correspond to antiferromagnetic and ferromagnetic interlayer coupling, respectively. This is supported by the polarization dependence of Raman spectra measured at the three selected positions P, Q, and R, as shown in Fig. 4.10a, b, and c, respectively. The AFM II domain exhibits the four-fold polarization

dependence for the peak near 105 cm^{-1}, which indicates two monoclinic stacking interfaces. The AFM I domain shows a weaker four-fold polarization dependence, which corresponds to one monoclinic stacking interface and one rhombohedral stacking interface. The absence of the four-fold polarization dependence in the FM domain reveals two rhombohedral stacking interfaces. In conclusion, we demonstrate the coexisting domains of magnetic and layer stacking phases in trilayer CrI_3.

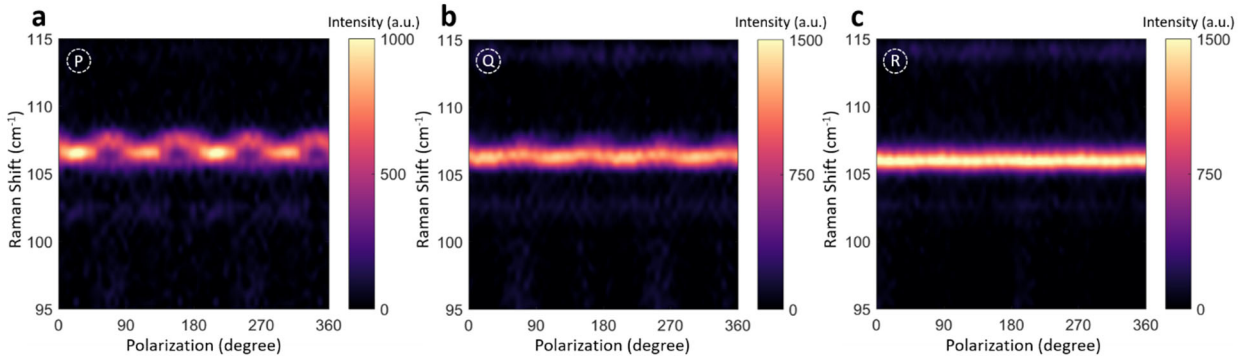

Figure 4. 10. Polarization dependence of Raman spectra for the trilayer CrI_3. (**a**), (**b**) and (**c**) Polarization dependence of Raman spectra in the cross-polarization channel measured at the three selected positions P, Q, and R indicated in Fig. 4.9a, respectively, at 80 K. The four-fold polarization dependence of the peak near 105 cm^{-1} indicates the monoclinic stacking. The absence of the four-fold polarization dependence indicates the rhombohedral stacking. Reproduced from reference[81] with permission.

Chapter 5. SPIN PHOTOVOLTAIC EFFECT IN MAGNETIC VAN DER WAALS HETEROSTRUCTURES

In Chapter 5, we will investigate the spin photovoltaic effect in magnetic vdW heterostructures. We will first introduce the photocurrent response of CrI_3 junction devices, and present the dependence of photocurrent on magnetic states in CrI_3. We will then report the helicity dependence of photocurrent, and discuss the interplay between magnetic order and photon helicity in absorption and photocurrent, demonstrating a proof-of-concept spin-optoelectronics device by engineering magnetic vdW heterostructures.

5.1 PHOTOVOLTAIC EFFECT IN CrI_3 JUNCTION DEVICE

Manipulating the spin degree of freedom in electronic systems for novel functionalities lies at the core of developing spintronics[98]. With optical illumination, in addition to optoelectronics, the generation and control of the spin degree of freedom can open up emerging opportunities for spin-optoelectronics, which enables the exploration of emergent spin photovoltaic effects and spin photocurrents. In different magnetic systems, spin photovoltaic effects can be achieved by different mechanisms. For example, a spin voltage arises from spin-dependent excitation at the interface of a nonmagnetic metal in close proximity to a magnetic insulator[99]. In magnetic multilayer devices, such as spin valves and magnetic p-n junctions, spin injection and accumulation can be induced by the spin-dependent injection process of the photogenerated carriers at the interfaces with ferromagnetic contacts[100–103]. Alternatively, in non-magnetic materials, circularly polarized light can generate spin photocurrents via the circular photogalvanic effect[104–107]. Among these systems, two-dimensional (2D) materials, in particular transition metal dichalcogenides (TMDs), have established themselves as a promising system for spin-

optoelectronics due to their spin-valley dependent properties and enhanced photoresponsivity from strong excitonic effects[9,10,106–112].

The recent discovery of 2D magnets provides new opportunities for investigating the spin photovoltaic effect based on atomically thin vdW materials with intrinsic magnetic order. Among these magnets, CrI_3, the focus of this thesis, is an ideal candidate because of its layered antiferromagnetism as we have discussed in detail in Chapter 2. The multiple magnetic states in few-layer CrI_3 can potentially enable multiple states of the resulting spin photocurrent, which is defined as a photocurrent controlled by the spin degree of freedom. Moreover, strong magneto-optical and excitonic effects are also reported in atomically thin CrI_3[113,114], which makes it an ideal platform to explore spin-optoelectronic effects in the atomically thin limit[115,116].

We start our spin photovoltaic effect study by investigating the photocurrent response of CrI_3 junction devices. Figure 5.1a shows the vertical junction vdW heterostructure we fabricate for efficient photodetection. Here, we show the four-layer CrI_3 device as an example. Such a structure is essentially the same as the magnetic tunnel junction devices we have discussed in detail in Chapter 3. As shown in Fig. 5.1b, without laser excitation, the *I-V* curve (black curve) measured from the four-layer CrI_3 device behaves like a typical tunnel junction. The tunneling current is suppressed in the low bias voltage regime and dominated by Fowler-Nordheim tunneling in the high bias voltage regime[40,57–59].

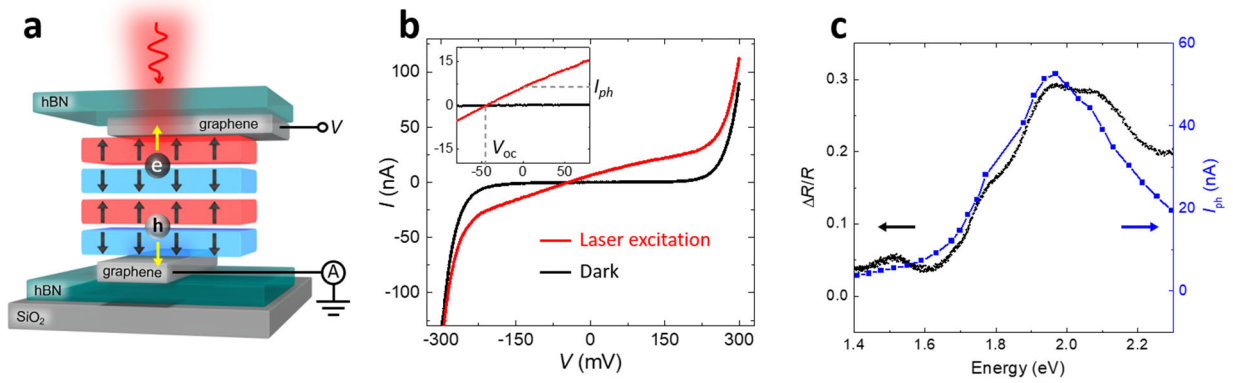

Figure 5. 1. Photovoltaic effect in CrI_3 junction device. (**a**) Schematic of the four-layer CrI_3 device in the magnetic ground state (↑↓↑↓), with the top and bottom graphene contacts and hBN encapsulation. (**b**) Tunneling current as a function of bias voltage measured from the four-layer CrI_3 device under dark conditions (black curve) and with 1 μW of 1.96 eV laser excitation (red curve). Inset shows the zoom-in view of the generated photocurrent at zero bias voltage (I_{ph}) and the open-circuit voltage (V_{oc}). (**c**) Differential reflectance ($\Delta R/R$, black dots) and overlaid zero-bias photocurrent (I_{ph}, blue squares) as a function of photon energy. The differential reflectance is measured from a trilayer CrI_3 flake on sapphire substrate at -2 T. The zero-bias photocurrent is measured from the trilayer CrI_3 device with an optical power of 10 μW. Reproduced from reference[116] with permission.

In contrast to the dark condition case, a substantial enhancement of the current is induced by the laser excitation in the low bias voltage regime, as shown in Fig. 5.1b. The *I*-*V* curve (red curve) is obtained with 1.96 eV (632.8 nm) laser excitation focused to the laser spot size of ~1 μm at normal incidence, with an optical power of 1 μW. This carrier collection process is highly efficient in the vertical junction device geometry for atomically thin CrI_3, which can reduce the carrier diffusion length to generate photocurrent. The inset in Fig. 5.1b shows that a net photocurrent (I_{ph}) is also generated at zero bias voltage. This zero-bias photocurrent can be attributed to the asymmetric potential of the junction device, which could originate from the potential difference between the top and bottom graphene/CrI_3 interfaces, as we have discussed in

detail in Chapters 2 and 3. When the bias voltage is applied between the top and bottom graphene contacts, an electric field is induced across the junction, which can modulate the magnitude and reverse the direction of the photocurrent. When the applied bias voltage compensates the asymmetric potential so that the net current is zero, the system is equivalent to an open circuit, which allows us to measure the photogenerated open-circuit voltage (V_{oc}). Therefore, the *I*-*V* curve reveals the zero-bias photocurrent (I_{ph}) and open-circuit voltage (V_{oc}), which are characteristics of the photovoltaic effect. We note that all the measurements discussed in this Chapter were carried out at a temperature of 2 K with magnetic field in the out-of-plane direction and linearly polarized laser excitation, unless otherwise specified.

Since the photovoltaic response is associated with the strong excitonic effect in CrI_3, we investigate the photon energy dependence of the zero-bias photocurrent, as shown in Fig. 5.1c. We find that the zero-bias photocurrent increases sharply when the photon energy exceeds 1.7 eV. To carry out a direct comparison of the zero-bias photocurrent and absorption, we also employ the differential reflectance ($\Delta R/R$) measurement of a trilayer CrI_3 flake on sapphire substrate, as shown in Fig. 5.1c. Here, the absorption of the atomically thin CrI_3 flake is proportional to the differential reflectance[113], and can be determined as $\frac{1}{4}(n^2-1)\Delta R/R$. By comparing the zero-bias photocurrent and absorption, we can attribute the strong photovoltaic response to the optical excitation of ligand-to-metal charge-transfer exciton states in CrI_3[113,114]. However, we do not observe zero-bias photocurrent enhancement corresponding to the excitation of the lower energy exciton state at 1.5 eV. This is possibly due to its larger binding energy and more localized nature than the charge transfer exciton states[114]. We also note that the photoresponsivity of this system can reach 10 mA W^{-1}, which is already comparable to that achieved in the devices based on TMD semiconductors under similar conditions[108,109,116], demonstrating a strong photoresponsivity.

We further investigate the spatial distribution of the zero-bias photocurrent by employing scanning photocurrent microscopy. Figure 5.2a shows the optical microscope image of the trilayer CrI_3 device, which has a relatively large junction area. In comparison, the zero-bias photocurrent map (Fig. 5.2b) shows the zero-bias photocurrent measured while scanning the laser spot. We also employ scanning RMCD microscopy measurement to map out the trilayer CrI_3 flake, which is shown in Fig. 5.2c. By comparing the zero-bias photocurrent map with the optical microscope image and the RMCD map, the photoactive region can be identified, which is the junction region where the top and bottom graphene contacts overlap. We note that the absence of the zero-bias photocurrent contribution beyond the overlap region implies the limited lateral diffusion length of the photoexcited carriers, possibly due to the relatively localized nature of the exciton states in CrI_3.

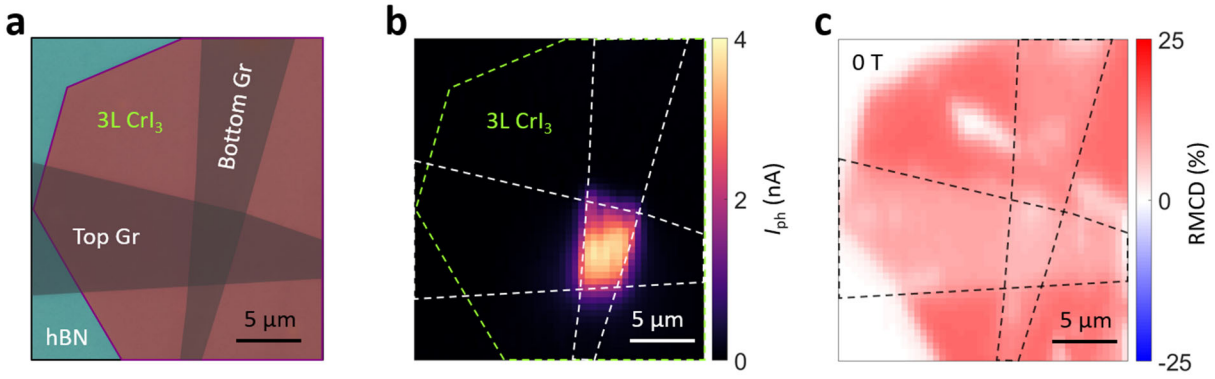

Figure 5. 2. Spatial distribution of zero-bias photocurrent in CrI_3 junction device. (**a**) Optical microscope image of the trilayer CrI_3 device. The overlap region between the top and bottom graphene contacts is the junction region. (**b**) Spatial map of zero-bias photocurrent measured from the same device at 0 T with an optical power of 1 μW. (**c**) Spatial map of RMCD signal measured from the same device at 0 T. Reproduced from reference[116] with permission.

5.2 Dependence of photocurrent on magnetic states

We have investigated the basic photovoltaic effect in CrI_3 junction devices in Section 5.1, which has not yet involved the spin degree of freedom and the multiple magnetic states in few-layer CrI_3. We next explore the spin photocurrent dependence on the magnetic order in few-layer CrI_3, and first take the four-layer CrI_3 device as an example. Figure 5.3a shows the zero-bias photocurrent as a function of magnetic field measured the four-layer CrI_3 device with an optical power of 1 μW. When the magnetic field is increased, the zero-bias photocurrent exhibits multiple plateaus and sharp jumps, and can be compared with the RMCD signal measured from the same device, as shown in Fig. 5.3b. The corresponding magnetic states can thus be identified as we have discussed in detail in Chapter 2. Here, we only show and discuss the positive magnetic field side for simplicity. We find that the multiple zero-bias photocurrent plateaus are associated with the identified magnetic states of four-layer CrI_3. The small and large zero-bias photocurrent plateaus at low and high magnetic fields can be assigned to the magnetic ground state (either ↑↓↑↓ or ↓↑↓↑) and the fully spin-polarized states (↑↑↑↑ and ↓↓↓↓), respectively.

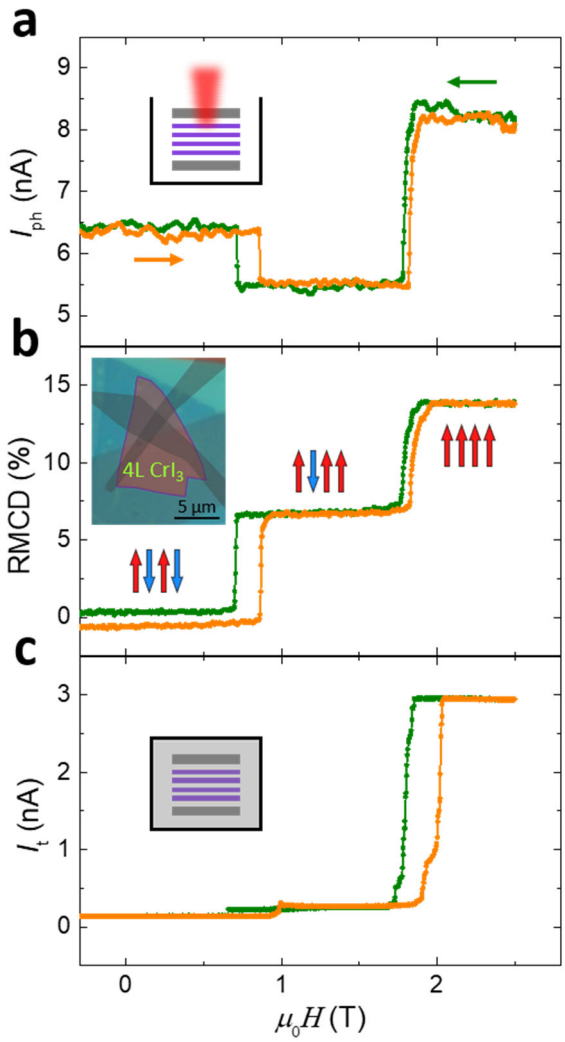

Figure 5. 3. Photocurrent dependence on magnetic order in four-layer CrI_3. (**a**) Zero-bias photocurrent as a function of magnetic field measured the four-layer CrI_3 device with an optical power of 1 μW. Green (orange) curve corresponds to decreasing (increasing) magnetic field. Inset shows the schematic of the device with laser excitation. (**b**) RMCD signal as a function of magnetic field measured from the same device. Insets show the corresponding magnetic states and the optical microscope image of the four-layer CrI_3 device. (**c**) Tunneling current as a function of magnetic field measured from the same device at a selected bias voltage (80 mV) under dark conditions. Inset shows the schematic of the device under dark conditions. Reproduced from reference[116] with permission.

In contrast, the intermediate magnetic state (either ↑↓↑↑ or ↑↑↓↑) results in a smaller zero-bias photocurrent than the magnetic ground state. This reveals a non-monotonic photocurrent response to the magnetic states, which is distinct from the monotonic enhancement of the tunneling current due to the spin-filtering effect we have discussed in detail in Chapter 2. To carry out a direct comparison of the zero-bias photocurrent and tunneling current, we also measure the tunneling current as a function of magnetic field from the same device at a selected bias voltage (80 mV) under dark conditions, which is shown in Fig. 5.3c. Distinct from the zero-bias photocurrent, the tunneling current increases monotonically and dramatically as the magnetizations in each layer are aligned from the magnetic ground state (either ↑↓↑↓ or ↓↑↓↑) to the fully spin-polarized states (↑↑↑↑ and ↓↓↓↓). We find that the tunneling current varies by two orders of magnitude for different magnetic states, while there is only a two-fold difference in the zero-bias photocurrent. These observations can be explained as follows. For the tunneling current under dark conditions, the tunneling electron energy is below the CrI_3 conduction bands. For the zero-bias photocurrent, the optical excitation generates the photoexcited carriers in the CrI_3 conduction bands, which are then extracted by the top and bottom graphene electrodes. Since the magnetic states determine the layer distribution of the wavefunction of the photoexcited carriers in the four-layer CrI_3, the extraction efficiencies at the top and bottom electrodes can be affected[108,109,117,118], which accounts for the non-monotonic magnetic state dependence of the zero-bias photocurrent. However, we also note that the determination of the precise magnetic-state-dependent band alignment between graphene and CrI_3 will require future theoretical and experimental efforts.

In analogy to the giant magnetoresistance and tunnel magnetoresistance effect in magnetic multilayer devices, and considering the CrI_3 spin-filter MTJ devices which have been realized and

discussed in detail in Chapter 2, the photocurrent response of the CrI_3 junction devices can also exhibit a novel photo-magnetocurrent effect[100]. Figure 5.4a shows the photocurrent as a function of bias voltage for the magnetic ground state (↑↓↑↓ at 0 T, black curve) and the fully spin-polarized state (↑↑↑↑ at 2.5 T, red curve), respectively. For the short-circuit (zero bias voltage) condition, the fully spin-polarized state gives a larger zero-bias photocurrent, whereas the magnetic ground state gives a larger open-circuit voltage magnitude. To quantify this observed magnetic state dependence, we define the photo-magnetocurrent ratio as $MC_{ph} = (I_{ph}^{p} - I_{ph}^{ap}) / I_{ph}^{ap}$, where I_{ph}^{p} and I_{ph}^{ap} correspond to the photocurrents for the fully spin-polarized state (parallel) and the magnetic ground state (antiparallel). Figure 5.4b shows the absolute value of MC_{ph} as a function of bias voltage, which is extracted from the I_{ph}-V curves in Fig. 5.4a. Remarkably, a giant photo-magnetocurrent effect is observed in a range of bias voltage indicated by the red shading. We attribute this observation to the magnetic-state-dependent open-circuit voltage, where at certain bias voltage I_{ph}^{ap} goes to zero while I_{ph}^{p} is still finite. This leads to a giant MC_{ph} ratio tending to infinity and demonstrates the proof-of-concept photo-magnetocurrent effect.

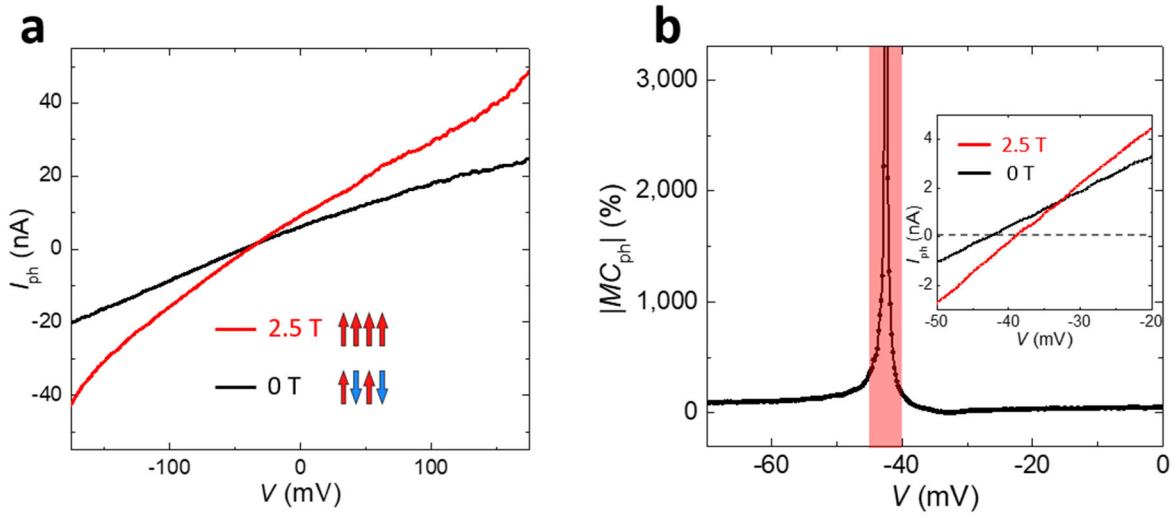

Figure 5. 4. Photo-magnetocurrent effect in four-layer CrI_3 junction device. (**a**) Photocurrent as a function of bias voltage measured from the four-layer CrI_3 device for the magnetic ground state

(↑↓↑↓ at 0 T, black curve) and the fully spin-polarized state (↑↑↑↑ at 2.5 T, red curve). (**b**) Magnitude of the photo-magnetocurrent ratio as a function of bias voltage, which is extracted from the I_{ph}-V curves in (a). The red shading indicates the bias voltage range where $|MC_{ph}|$ tends to infinity. Inset shows the zoom-in view of the I_{ph}-V curves in (a). Reproduced from reference[116] with permission.

We further investigate the excitation power dependence to potentially realize the optical control of the photo-magnetocurrent effect. Figure 5.5a and b show the excitation power dependence of the photocurrent as a function of bias voltage measured from the trilayer CrI_3 device for the magnetic ground state (↑↓↑ at 0 T) and the fully spin-polarized state (↑↑↑ at 2.5 T), respectively, which exhibit high sensitivity to the excitation power. Figure 5.5d shows the open-circuit voltage as a function of excitation power extracted from the I_{ph}-V curves in Fig. 5.5a and b, revealing that the open-circuit voltage is highly tunable by the excitation power. The magnitude of the photo-magnetocurrent ratio as a function of bias voltage and excitation power is also extracted from the I_{ph}-V curves in Fig. 5.5a and b, which is shown in Fig. 5.5c. Similarly, we observe a giant photo-magnetocurrent effect, consistent with the four-layer CrI_3 device in Fig. 5.4b, and the bias voltage range is also highly tunable by the excitation power. These observations demonstrate the optical control of the photo-magnetocurrent effect with high sensitivity to the excitation power. Realizing such a giant and tunable photo-magnetocurrent effect is important for potential applications, such as optically driven magnetic sensing and data storage technologies.

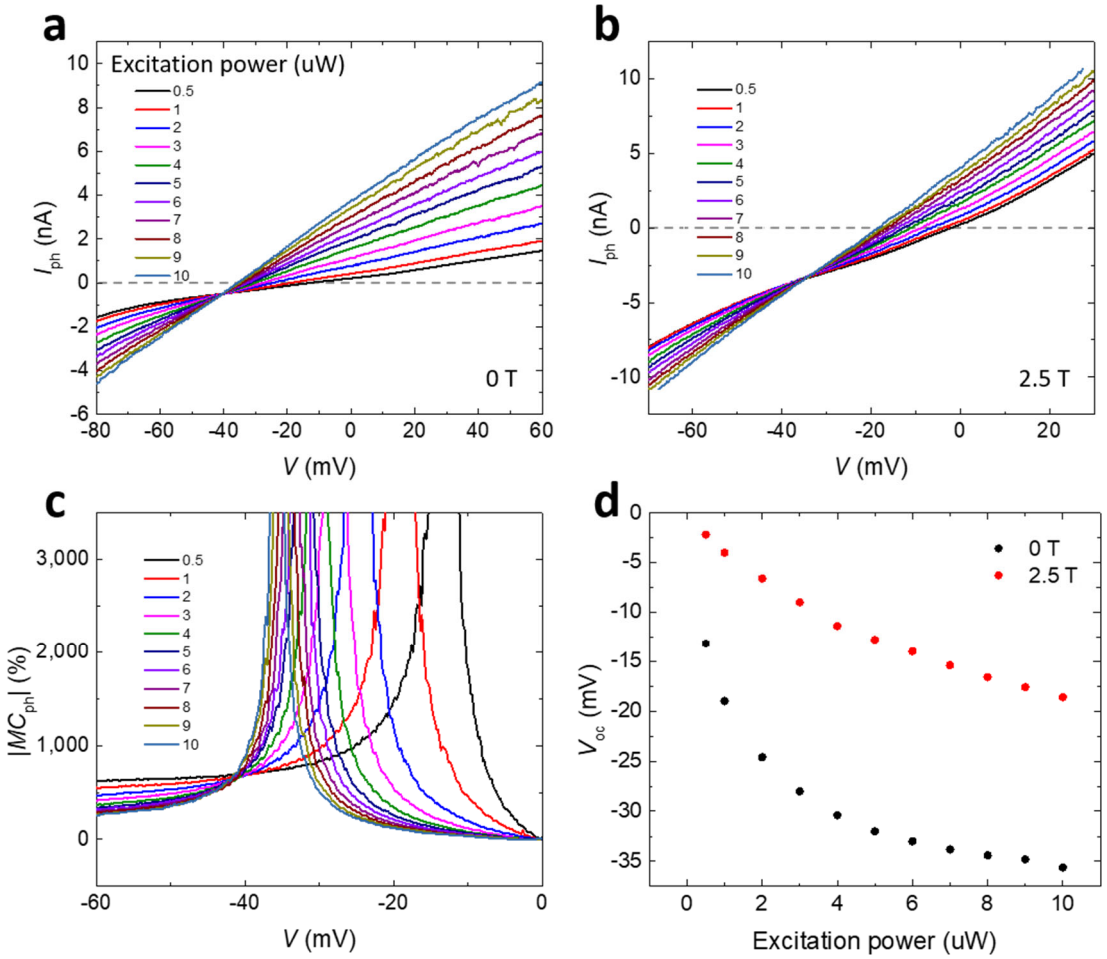

Figure 5. 5. Excitation power dependence of photo-magnetocurrent effect. (**a**) and (**b**) Excitation power dependence of the photocurrent as a function of bias voltage measured from the trilayer CrI_3 device for the magnetic ground state (↑↓↑ at 0 T, a) and the fully spin-polarized state (↑↑↑ at 2.5 T, b). (**c**) Magnitude of the photo-magnetocurrent ratio as a function of bias voltage and excitation power, which is extracted from the I_{ph}-V curves in (a) and (b). (**d**) Open-circuit voltage as a function of excitation power extracted from the I_{ph}-V curves in (a) and (b) for the magnetic ground state (↑↓↑ at 0 T, black dots) and the fully spin-polarized state (↑↑↑ at 2.5 T, red dots). Reproduced from reference[116] with permission.

5.3 HELICITY DEPENDENCE OF PHOTOCURRENT

The presence of magnetic order can break the time-reversal symmetry of the system, which will potentially enable a photon helicity dependence of the spin photocurrent. Here, we take the trilayer CrI_3 device as an example, and we note that the zero-bias photocurrent is measured with 10 μW of 1.96 eV laser excitation. We first focus on the two fully spin-polarized states (↑↑↑ and ↓↓↓), which are identified at 2 T and -2 T. To change the photon helicity, we use a motorized precision rotation mount to rotate an achromatic quarter-wave plate relative to the linear polarized incident laser excitation. Figure 5.6a shows that the zero-bias photocurrent exhibits a clear circular polarization dependence as the photon helicity is switched between σ^+ and σ^- by rotating the quarter-wave plate. We find that the ↑↑↑ state (red dots) exhibits a larger zero-bias photocurrent for the photon helicity σ^- (135°) than σ^+ (45°). In comparison, the ↓↓↓ state (black dots) exhibits the exact opposite photon helicity dependence. These observations are consistent with the time-reversal operation that connects the two fully spin-polarized states (↑↑↑ and ↓↓↓).

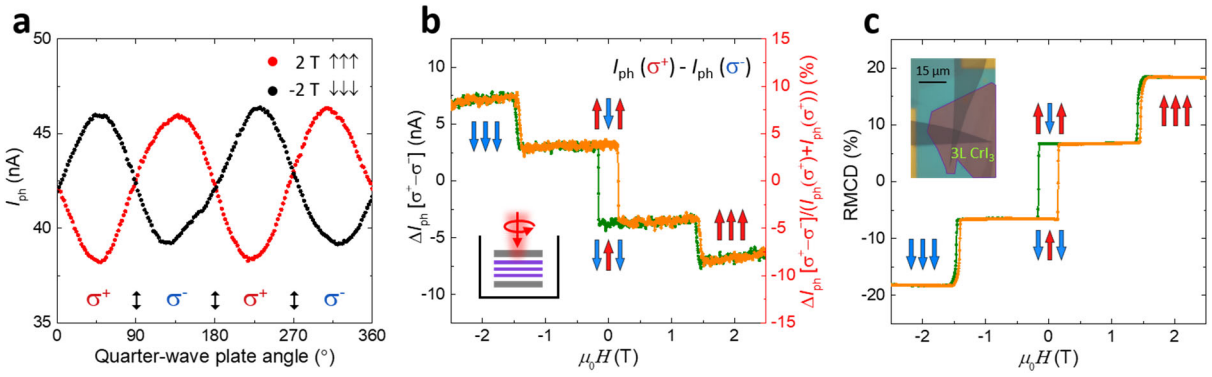

Figure 5. 6. Helicity dependence of zero-bias photocurrent in trilayer CrI_3. (**a**) Zero-bias photocurrent as a function of the quarter-wave plate angle for the ↑↑↑ state (2 T, red dots) and the ↓↓↓ state (-2 T, black dots) measured from the trilayer CrI_3 device with an optical power of 10 μW. Vertical arrows represent the linear polarized incident laser excitation. (**b**) The change in zero-bias photocurrent (ΔI_{ph} [σ^+-σ^-] = $I_{ph}(\sigma^+)$ - $I_{ph}(\sigma^-)$) as a function of magnetic field measured

from the same device with an optical power of 10 μW. The degree of helicity is defined as ΔI_{ph} $[\sigma^+-\sigma^-]/(I_{ph}(\sigma^+) + I_{ph}(\sigma^-))$, which is shown on the right axis. Green (orange) curve corresponds to decreasing (increasing) magnetic field. Insets show the corresponding magnetic states and the schematic of the device with circularly polarized laser excitation. (**c**) RMCD signal as a function of magnetic field measured from the same device. Insets show the corresponding magnetic states and the optical microscope image of the trilayer CrI_3 device. Reproduced from reference[116] with permission.

To quantify this observed photon helicity dependence of the spin photocurrent, we define the difference of the zero-bias photocurrent between the σ^+ and σ^- laser excitation as ΔI_{ph} $[\sigma^+-\sigma^-]$ = $I_{ph}(\sigma^+)$ - $I_{ph}(\sigma^-)$. We can also define the degree of helicity as ΔI_{ph} $[\sigma^+-\sigma^-]/(I_{ph}(\sigma^+) + I_{ph}(\sigma^-))$. To further investigate the interplay between the photon helicity dependence of the spin photocurrent and the underlying magnetic order, we measure the change in zero-bias photocurrent (ΔI_{ph} $[\sigma^+-\sigma^-]$) as a function of magnetic field, as shown in Fig. 5.6b. We also calculate the degree of helicity from the zero-bias photocurrent, which is shown on the right axis. Four distinct plateaus are observed in the change in zero-bias photocurrent, which is very similar to the RMCD signal as a function of magnetic field measured from the same device (Fig. 5.6c). The direct comparison of the change in zero-bias photocurrent and the RMCD signal can assign the corresponding magnetic states to the four plateaus of the change in zero-bias photocurrent, as shown in Fig. 5.6 b and c. The magnetic hysteresis loop of the change in zero-bias photocurrent centered at zero magnetic field can be attributed to the switching between the two magnetic ground states of trilayer CrI_3 (↑↓↑ and ↓↑↓).

5.4 INTERPLAY BETWEEN MAGNETIC ORDER AND PHOTON HELICITY IN ABSORPTION AND PHOTOCURRENT

The observations in Section 5.3 reveal that the photon helicity dependence of the spin photocurrent is closely associated with the underlying magnetic order through the circular polarization dependence of absorption, which possibly originates from the magnetic-order-coupled charge-transfer exciton states in CrI_3. Here, we note that the reflective magnetic circular dichroism (RMCD) signal in Fig. 5.6c essentially captures the circular polarization dependence of reflection, which should also exhibit a similar circular polarization of absorption. To directly measure the circular polarization of absorption, we employ the circular polarization-resolved differential reflectance ($\Delta R/R$) measurement of a trilayer CrI_3 flake on sapphire substrate. All the four magnetic states of trilayer CrI_3 at selected magnetic fields {↑↑↑ (2 T), ↓↓↓ (-2 T), ↑↓↑ (0 T), ↓↑↓ (0 T)} are shown in Fig. 5.7. Distinct from the absorption measurement in Fig. 5.1c, we find that the σ^+/σ^- (red/blue dots) absorption peaks split in both energy and intensity, and show strong magnetic state dependence. These observations are consistent with the magnetic-order-coupled charge-transfer exciton states in CrI_3 calculated by the many-body perturbation theory[114]. The splitting between the σ^+ and σ^- absorption peaks reveals the optical selection rules of the charge-transfer transitions between the spin-polarized valence and conduction bands[114,119].

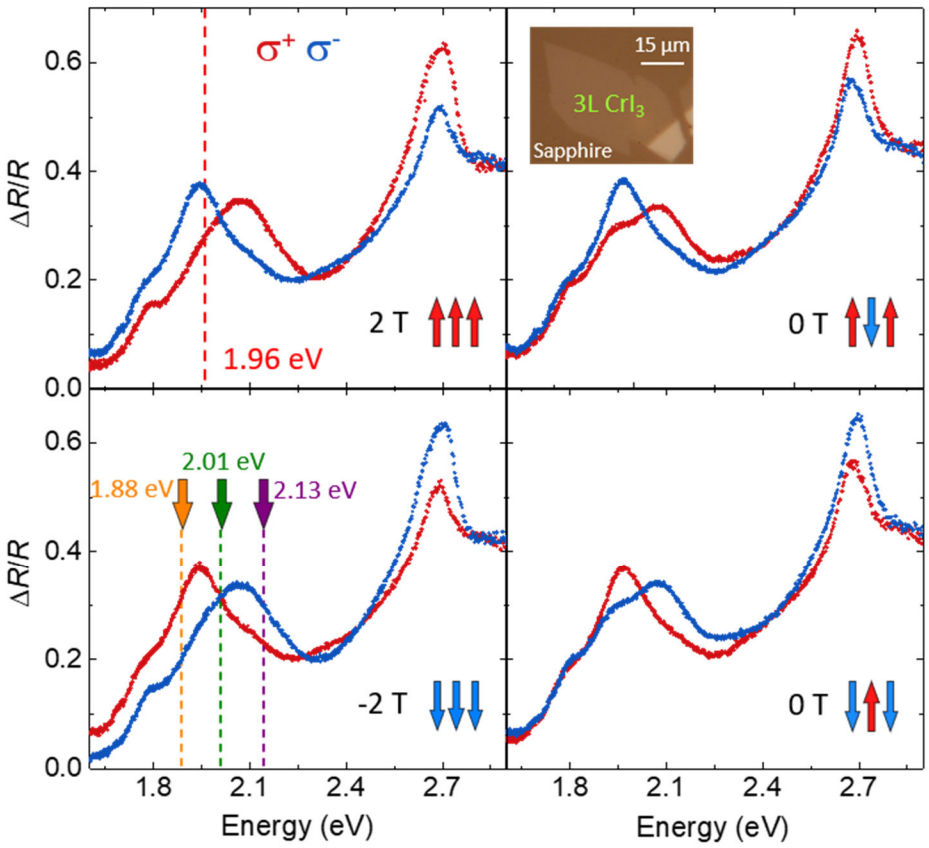

Figure 5. 7. Circular polarization-resolved differential reflectance ($\Delta R/R$) spectra measured from a trilayer CrI_3 flake on sapphire substrate for all the four magnetic states of trilayer CrI_3 at selected magnetic fields {↑↑↑ (2 T), ↓↓↓ (-2 T), ↑↓↑ (0 T), ↓↑↓ (0 T)}. Red and blue dots correspond to the σ^+ and σ^- photon helicity, respectively. Insets show the corresponding magnetic states and the optical microscope image of the trilayer CrI_3 flake on sapphire substrate. Reproduced from reference[116] with permission.

The observed magnetic-order-coupled charge-transfer exciton states in CrI_3 can potentially explain the photon helicity dependence of the spin photocurrent we have shown in Section 5.3. As shown in Fig. 5.7, for the ↑↑↑ state, the 1.96 eV (632.8 nm) laser excitation indicated by the red dashed line is near the resonance of the charge-transfer exciton state for the σ^- photon helicity, while the resonance for the σ^+ photon helicity corresponds to a different charge-

transfer exciton state at ~2.07 eV, which is about 110 meV higher. The stronger absorption at 1.96 eV for the σ^- than σ^+ photon helicity can lead to the larger zero-bias photocurrent for the σ^- than σ^+ laser excitation at 1.96 eV, as shown in Fig. 5.6a. For the ↓↓↓ state, the absorption peaks are switched for the σ^- than σ^+ photon helicity in comparison to the ↑↑↑ state, which also agrees well with the opposite photon helicity dependence of the spin photocurrent for the ↓↓↓ state (Fig. 5.6a). Furthermore, we also observe notable but opposite splitting between the σ^+ and σ^- absorption peaks for the two magnetic ground states of trilayer CrI_3 at zero magnetic field (↑↓↑ and ↓↑↓), which can be attributed to the opposite net magnetizations of the two magnetic states. All these observations reveal that the charge-transfer exciton states in CrI_3 are coupled to the underlying magnetic order, which is the physical origin of the photon helicity dependence of the spin photocurrent.

We can further utilize the circularly polarized optical selection rules of the charge-transfer exciton states to control the photon helicity dependence of the spin photocurrent by tuning the photon energy. As indicated by the dashed lines in Fig. 5.7, we select three photon energies, which correspond to stronger σ^+ absorption than σ^- (1.88 eV), nearly equal absorption (2.01 eV), and weaker σ^+ absorption than σ^- (2.13 eV), respectively, for the ↓↓↓ state. Figure 5.8 shows the photon helicity dependence of the zero-bias photocurrent measured with the three selected photon energies. We find that, for the ↓↓↓ state, the σ^+ laser excitation at 1.88 eV gives a larger zero-bias photocurrent than the σ^- laser excitation, and this photon helicity dependence is reversed for the laser excitation at 2.13 eV, which are in good agreement with the photon helicity dependence of absorption. For the laser excitation at 2.01 eV, the photon helicity dependence of the zero-bias photocurrent nearly vanishes, consistent with the observed nearly equal absorption for the σ^+ and σ^- laser excitation.

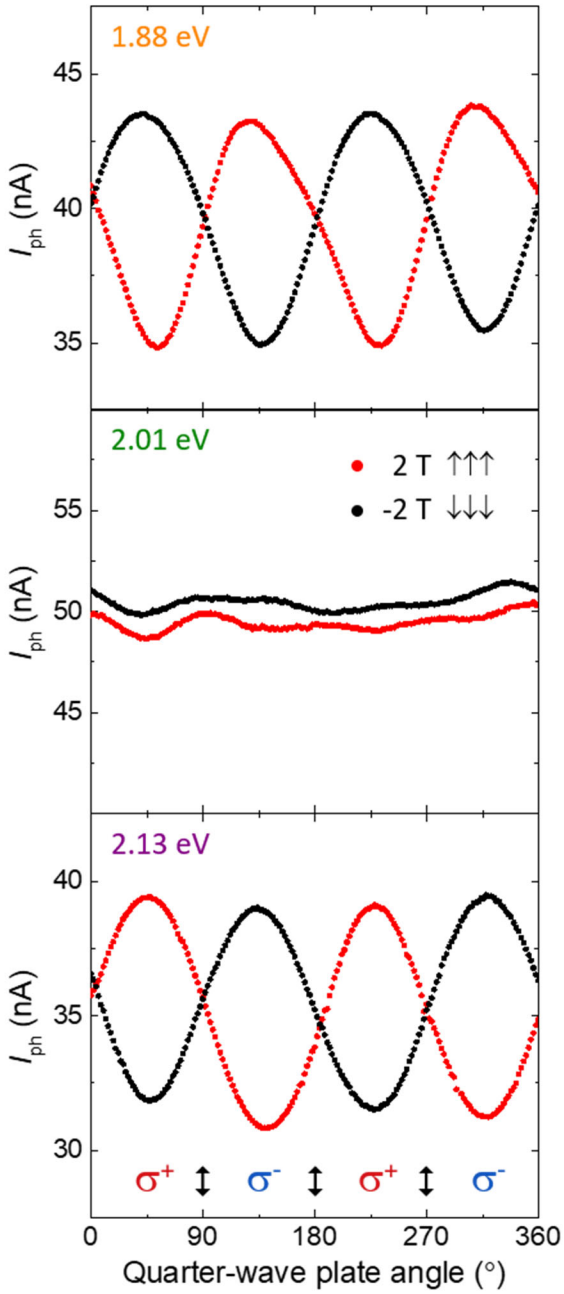

Figure 5. 8. Zero-bias photocurrent as a function of the quarter-wave plate angle for the ↑↑↑ state (2 T, red dots) and the ↓↓↓ state (-2 T, black dots) measured from the trilayer CrI_3 device with an optical power of 10 μW for the three selected photon energies indicated by the dashed lines in Fig. 5.7. Reproduced from reference[116] with permission.

To directly compare the photon helicity dependence of the zero-bias photocurrent and absorption, we measure the change in zero-bias photocurrent for the σ^+ and σ^- laser excitation (ΔI_{ph} [σ^+-σ^-]) as a function of photon energy, as shown in Fig. 5.9. For the ↓↓↓ state, we observe positive and negative change in zero-bias photocurrent as a function of photon energy, and a change in sign at ~2.01 eV. This matches well with the overlaid photon helicity difference of the differential reflectance ($\Delta R/R(\sigma^+)$-$\Delta R/R(\sigma^-)$). In contrast, the photon helicity dependence is reversed for the ↑↑↑ state, since it is the time reversal of the ↓↓↓ state, as shown in Fig. 5.8 and 5.9. All these observations reveal the strong correspondence between the zero-bias photocurrent and the RMCD signal in Fig. 5.6. For a given magnetic state (↑↑↑) and photon energy, the splitting between the σ^+ and σ^- absorption peaks reveals the circular polarization dependence of absorption and reflection, which result in the photon helicity dependence of the zero-bias photocurrent and the RMCD signal, respectively. As the photon energy is tuned, the photon helicity difference of the differential reflectance can be switched, and thus the photon helicity dependence of the zero-bias photocurrent is also reversed.

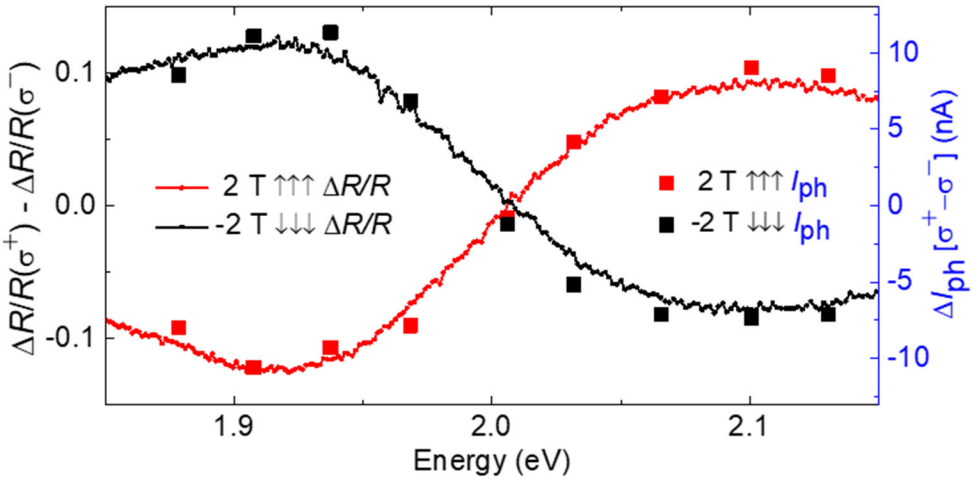

Figure 5. 9. Photon helicity difference of the differential reflectance ($\Delta R/R(\sigma^+)$-$\Delta R/R(\sigma^-)$) and the overlaid change in zero-bias photocurrent (ΔI_{ph} [σ^+-σ^-] = $I_{ph}(\sigma^+)$ - $I_{ph}(\sigma^-)$) as a function of photon

energy for the ↑↑↑ state (2 T, red dots) and the ↓↓↓ state (-2 T, black dots) of trilayer CrI_3. The differential reflectance is measured from the trilayer CrI_3 flake on sapphire substrate at -2 T. The zero-bias photocurrent is measured from the trilayer CrI_3 device with an optical power of 10 μW. Reproduced from reference[116] with permission.

In conclusion, we explore the spin photovoltaic effect in magnetic vdW heterostructures based on atomically thin CrI_3. The photocurrent response of CrI_3 junction devices exhibits distinct dependence on the magnetic states, together with a giant photo-magnetocurrent effect. We also investigate the photon helicity dependence of the photocurrent response, revealing the emergent interplay between the spin photocurrent and the underlying excitons, intrinsic magnetic order, photon energy and helicity. We demonstrate a proof-of-concept spin-optoelectronics device by engineering magnetic vdW heterostructures.

BIBLIOGRAPHY

1. Novoselov, K. S. *et al.* Electric Field Effect in Atomically Thin Carbon Films. *Science* **306**, 666–669 (2004).

2. Neto, A. H. C., Guinea, F., Peres, N. M. R., Novoselov, K. S. & Geim, A. K. The electronic properties of graphene. *Rev Mod Phys* **81**, 109–162 (2009).

3. Zhang, Y., Tan, Y.-W., Stormer, H. L. & Kim, P. Experimental observation of the quantum Hall effect and Berry's phase in graphene. *Nature* **438**, 201–204 (2005).

4. Novoselov, K. S. *et al.* Two-dimensional gas of massless Dirac fermions in graphene. *Nature* **438**, 197–200 (2005).

5. Bolotin, K. I., Ghahari, F., Shulman, M. D., Stormer, H. L. & Kim, P. Observation of the fractional quantum Hall effect in graphene. *Nature* **462**, 196–199 (2009).

6. Mak, K. F., Lee, C., Hone, J., Shan, J. & Heinz, T. F. Atomically Thin MoS2: A New Direct-Gap Semiconductor. *Phys Rev Lett* **105**, 136805 (2010).

7. Splendiani, A. *et al.* Emerging Photoluminescence in Monolayer MoS2. *Nano Lett* **10**, 1271–1275 (2010).

8. Wang, Q. H., Kalantar-Zadeh, K., Kis, A., Coleman, J. N. & Strano, M. S. Electronics and optoelectronics of two-dimensional transition metal dichalcogenides. *Nat Nanotechnol* **7**, 699–712 (2012).

9. Xu, X., Yao, W., Xiao, D. & Heinz, T. F. Spin and pseudospins in layered transition metal dichalcogenides. *Nat Phys* **10**, 343–350 (2014).

10. Mak, K. F. & Shan, J. Photonics and optoelectronics of 2D semiconductor transition metal dichalcogenides. *Nat Photonics* **10**, 216–226 (2016).

11. Dean, C. R. *et al.* Boron nitride substrates for high-quality graphene electronics. *Nat Nanotechnol* **5**, 722–726 (2010).

12. Wang, L. *et al.* One-Dimensional Electrical Contact to a Two-Dimensional Material. *Science* **342**, 614–617 (2013).

13. Xi, X. *et al.* Ising pairing in superconducting NbSe2 atomic layers. *Nat Phys* **12**, 139–143 (2016).

14. Fatemi, V. *et al.* Electrically tunable low-density superconductivity in a monolayer topological insulator. *Science* **362**, eaar4642 (2018).

15. Sajadi, E. *et al.* Gate-induced superconductivity in a monolayer topological insulator. *Science* **362**, eaar4426 (2018).

16. Yu, Y. *et al.* Gate-tunable phase transitions in thin flakes of 1T-TaS2. *Nat Nanotechnol* **10**, 270–276 (2015).

17. Wu, S. *et al.* Observation of the quantum spin Hall effect up to 100 kelvin in a monolayer crystal. *Science* **359**, 76–79 (2018).

18. Fei, Z. *et al.* Edge conduction in monolayer WTe2. *Nat Phys* **13**, 677–682 (2017).

19. Qian, X., Liu, J., Fu, L. & Li, J. Quantum spin Hall effect in two-dimensional transition metal dichalcogenides. *Science* **346**, 1344–1347 (2014).

20. Fei, Z. *et al.* Ferroelectric switching of a two-dimensional metal. *Nature* **560**, 336–339 (2018).

21. Liu, Y. *et al.* Van der Waals heterostructures and devices. *Nat Rev Mater* **1**, 16042 (2016).

22. Geim, A. K. & Grigorieva, I. V. Van der Waals heterostructures. *Nature* **499**, 419–425 (2013).

23. Novoselov, K. S., Mishchenko, A., Carvalho, A. & Neto, A. H. C. 2D materials and van der Waals heterostructures. *Science* **353**, aac9439 (2016).

24. Dean, C. R. *et al.* Hofstadter's butterfly and the fractal quantum Hall effect in moiré superlattices. *Nature* **497**, 598–602 (2013).

25. Hunt, B. *et al.* Massive Dirac Fermions and Hofstadter Butterfly in a van der Waals Heterostructure. *Science* **340**, 1427–1430 (2013).

26. Ponomarenko, L. A. *et al.* Cloning of Dirac fermions in graphene superlattices. *Nature* **497**, 594–597 (2013).

27. Cao, Y. *et al.* Unconventional superconductivity in magic-angle graphene superlattices. *Nature* **556**, 43–50 (2018).

28. Cao, Y. *et al.* Correlated insulator behaviour at half-filling in magic-angle graphene superlattices. *Nature* **556**, 80–84 (2018).

29. Huang, B. *et al.* Layer-dependent ferromagnetism in a van der Waals crystal down to the monolayer limit. *Nature* **546**, 270–273 (2017).

30. Gong, C. *et al.* Discovery of intrinsic ferromagnetism in two-dimensional van der Waals crystals. *Nature* **546**, 265–269 (2017).

31. Mermin, N. D. & Wagner, H. Absence of Ferromagnetism or Antiferromagnetism in One- or Two-Dimensional Isotropic Heisenberg Models. *Phys Rev Lett* **17**, 1133–1136 (1966).

32. Burch, K. S., Mandrus, D. & Park, J.-G. Magnetism in two-dimensional van der Waals materials. *Nature* **563**, 47–52 (2018).

33. Gong, C. & Zhang, X. Two-dimensional magnetic crystals and emergent heterostructure devices. *Science* **363**, eaav4450 (2019).

34. Mak, K. F., Shan, J. & Ralph, D. C. Probing and controlling magnetic states in 2D layered magnetic materials. *Nat Rev Phys* **1**, 646–661 (2019).

35. Gibertini, M., Koperski, M., Morpurgo, A. F. & Novoselov, K. S. Magnetic 2D materials and heterostructures. *Nat Nanotechnol* **14**, 408–419 (2019).

36. Huang, B. *et al.* Emergent phenomena and proximity effects in two-dimensional magnets and heterostructures. *Nat Mater* **19**, 1276–1289 (2020).

37. McGuire, M. A., Dixit, H., Cooper, V. R. & Sales, B. C. Coupling of Crystal Structure and Magnetism in the Layered, Ferromagnetic Insulator CrI3. *Chem Mater* **27**, 612–620 (2015).

38. Shcherbakov, D. *et al.* Raman Spectroscopy, Photocatalytic Degradation, and Stabilization of Atomically Thin Chromium Tri-iodide. *Nano Lett* **18**, 4214–4219 (2018).

39. Sato, K. Measurement of Magneto-Optical Kerr Effect Using Piezo-Birefringent Modulator. *Jpn J Appl Phys* **20**, 2403 (2014).

40. Song, T. *et al.* Giant tunneling magnetoresistance in spin-filter van der Waals heterostructures. *Science* **360**, eaar4851 (2018).

41. Hellwig, O., Kirk, T. L., Kortright, J. B., Berger, A. & Fullerton, E. E. A new phase diagram for layered antiferromagnetic films. *Nat Mater* **2**, 112–116 (2003).

42. Hellwig, O., Berger, A., Kortright, J. B. & Fullerton, E. E. Domain structure and magnetization reversal of antiferromagnetically coupled perpendicular anisotropy films. *J Magn Magn Mater* **319**, 13–55 (2007).

43. Chen, B. *et al.* All-oxide–based synthetic antiferromagnets exhibiting layer-resolved magnetization reversal. *Science* **357**, 191–194 (2017).

44. Charilaou, M., Bordel, C. & Hellman, F. Magnetization switching and inverted hysteresis in perpendicular antiferromagnetic superlattices. *Appl Phys Lett* **104**, 212405 (2014).

45. Baibich, M. N., Broto, J. M., Fert, A., Dau, F. N. V. & Petroff, F. Giant Magnetoresistance of (001)Fe/(001)Cr Magnetic Superlattices. *Phys Rev Lett* **61**, 2472–2475 (1988).

46. Binasch, G., Grünberg, P., Saurenbach, F. & Zinn, W. Enhanced magnetoresistance in layered magnetic structures with antiferromagnetic interlayer exchange. *Phys Rev B* **39**, 4828–4830 (1989).

47. Dieny, B. *et al.* Giant magnetoresistive in soft ferromagnetic multilayers. *Phys Rev B* **43**, 1297–1300 (1991).

48. Julliere, M. Tunneling between ferromagnetic films. *Phys Lett A* **54**, 225–226 (1975).

49. Moodera, J. S., Kinder, L. R., Wong, T. M. & Meservey, R. Large Magnetoresistance at Room Temperature in Ferromagnetic Thin Film Tunnel Junctions. *Phys Rev Lett* **74**, 3273–3276 (1995).

50. Miyazaki, T. & Tezuka, N. Giant magnetic tunneling effect in Fe/Al2O3/Fe junction. *J Magn Magn Mater* **139**, L231–L234 (1995).

51. Yuasa, S., Nagahama, T., Fukushima, A., Suzuki, Y. & Ando, K. Giant room-temperature magnetoresistance in single-crystal Fe/MgO/Fe magnetic tunnel junctions. *Nat Mater* **3**, 868–871 (2004).

52. Parkin, S. S. P. *et al.* Giant tunnelling magnetoresistance at room temperature with MgO (100) tunnel barriers. *Nat Mater* **3**, 862–867 (2004).

53. Ikeda, S. *et al.* Tunnel magnetoresistance of 604% at 300K by suppression of Ta diffusion in CoFeB/MgO/CoFeB pseudo-spin-valves annealed at high temperature. *Appl Phys Lett* **93**, 082508 (2008).

54. Worledge, D. C. & Geballe, T. H. Magnetoresistive double spin filter tunnel junction. *J Appl Phys* **88**, 5277–5279 (2000).

55. Miao, G.-X., Müller, M. & Moodera, J. S. Magnetoresistance in Double Spin Filter Tunnel Junctions with Nonmagnetic Electrodes and its Unconventional Bias Dependence. *Phys Rev Lett* **102**, 076601 (2009).

56. Miao, G.-X., M?nzenberg, M. & Moodera, J. S. Tunneling path toward spintronics. *Rep Prog Phys* **74**, 036501 (2011).

57. Klein, D. R. *et al.* Probing magnetism in 2D van der Waals crystalline insulators via electron tunneling. *Science* **360**, eaar3617 (2018).

58. Wang, Z. *et al.* Very large tunneling magnetoresistance in layered magnetic semiconductor CrI3. *Nat Commun* **9**, 2516 (2018).

59. Kim, H. H. *et al.* One Million Percent Tunnel Magnetoresistance in a Magnetic van der Waals Heterostructure. *Nano Lett* **18**, 4885–4890 (2018).

60. Zhong, D. *et al.* Van der Waals engineering of ferromagnetic semiconductor heterostructures for spin and valleytronics. *Sci Adv* **3**, e1603113 (2017).

61. Britnell, L. *et al.* Field-Effect Tunneling Transistor Based on Vertical Graphene Heterostructures. *Science* **335**, 947–950 (2012).

62. Lee, G.-H. *et al.* Electron tunneling through atomically flat and ultrathin hexagonal boron nitride. *Appl Phys Lett* **99**, 243114 (2011).

63. Georgiou, T. *et al.* Vertical field-effect transistor based on graphene–WS2 heterostructures for flexible and transparent electronics. *Nat Nanotechnol* **8**, 100–103 (2013).

64. McGuire, T. & Potter, R. Anisotropic magnetoresistance in ferromagnetic 3d alloys. *Ieee T Magn* **11**, 1018–1038 (1975).

65. Matsukura, F., Tokura, Y. & Ohno, H. Control of magnetism by electric fields. *Nat Nanotechnol* **10**, 209–220 (2015).

66. Ohno, H. *et al.* Electric-field control of ferromagnetism. *Nature* **408**, 944–946 (2000).

67. Chiba, D., Yamanouchi, M., Matsukura, F. & Ohno, H. Electrical Manipulation of Magnetization Reversal in a Ferromagnetic Semiconductor. *Science* **301**, 943–945 (2003).

68. Weisheit, M. *et al.* Electric Field-Induced Modification of Magnetism in Thin-Film Ferromagnets. *Science* **315**, 349–351 (2007).

69. Maruyama, T. *et al.* Large voltage-induced magnetic anisotropy change in a few atomic layers of iron. *Nat Nanotechnol* **4**, 158–161 (2009).

70. Wang, W.-G., Li, M., Hageman, S. & Chien, C. L. Electric-field-assisted switching in magnetic tunnel junctions. *Nat Mater* **11**, 64–68 (2012).

71. Shiota, Y. *et al.* Induction of coherent magnetization switching in a few atomic layers of FeCo using voltage pulses. *Nat Mater* **11**, 39–43 (2012).

72. Huang, B. *et al.* Electrical control of 2D magnetism in bilayer CrI3. *Nat Nanotechnol* **13**, 544–548 (2018).

73. Jiang, S., Shan, J. & Mak, K. F. Electric-field switching of two-dimensional van der Waals magnets. *Nat Mater* **17**, 406–410 (2018).

74. Jiang, S., Li, L., Wang, Z., Mak, K. F. & Shan, J. Controlling magnetism in 2D CrI3 by electrostatic doping. *Nat Nanotechnol* **13**, 549–553 (2018).

75. Sivadas, N., Okamoto, S. & Xiao, D. Gate-Controllable Magneto-optic Kerr Effect in Layered Collinear Antiferromagnets. *Phys Rev Lett* **117**, 267203 (2016).

76. Song, T. *et al.* Voltage Control of a van der Waals Spin-Filter Magnetic Tunnel Junction. *Nano Lett* **19**, 915–920 (2019).

77. Jiang, P. *et al.* Stacking tunable interlayer magnetism in bilayer CrI3. *Phys Rev B* **99**, 144401 (2019).

78. Soriano, D., Cardoso, C. & Fernández-Rossier, J. Interplay between interlayer exchange and stacking in CrI3 bilayers. *Solid State Commun* **299**, 113662 (2019).

79. Sivadas, N., Okamoto, S., Xu, X., Fennie, C. J. & Xiao, D. Stacking-Dependent Magnetism in Bilayer CrI 3. *Nano Lett* **18**, 7658–7664 (2018).

80. Jang, S. W., Jeong, M. Y., Yoon, H., Ryee, S. & Han, M. J. Microscopic understanding of magnetic interactions in bilayer CrI3. *Phys Rev Mater* **3**, 031001 (2019).

81. Song, T. *et al.* Switching 2D magnetic states via pressure tuning of layer stacking. *Nat Mater* **18**, 1298–1302 (2019).

82. Li, T. *et al.* Pressure-controlled interlayer magnetism in atomically thin CrI3. *Nat Mater* **18**, 1303–1308 (2019).

83. Klein, D. R. *et al.* Enhancement of interlayer exchange in an ultrathin two-dimensional magnet. *Nat Phys* **15**, 1255–1260 (2019).

84. Chen, W. *et al.* Direct observation of van der Waals stacking–dependent interlayer magnetism. *Science* **366**, 983–987 (2019).

85. Sun, Z. *et al.* Giant nonreciprocal second-harmonic generation from antiferromagnetic bilayer CrI3. *Nature* **572**, 497–501 (2019).

86. Yankowitz, M. *et al.* Dynamic band-structure tuning of graphene moiré superlattices with pressure. *Nature* **557**, 404–408 (2018).

87. Ci, P. *et al.* Quantifying van der Waals Interactions in Layered Transition Metal Dichalcogenides from Pressure-Enhanced Valence Band Splitting. *Nano Lett* **17**, 4982–4988 (2017).

88. Zhao, Z. *et al.* Pressure induced metallization with absence of structural transition in layered molybdenum diselenide. *Nat Commun* **6**, 7312 (2015).

89. Yankowitz, M. *et al.* Tuning superconductivity in twisted bilayer graphene. *Science* **363**, eaav1910 (2019).

90. Sun, Y. *et al.* Effects of hydrostatic pressure on spin-lattice coupling in two-dimensional ferromagnetic Cr2Ge2Te6. *Appl Phys Lett* **112**, 072409 (2018).

91. Son, S. *et al.* Bulk properties of the van der Waals hard ferromagnet VI3. *Phys Rev B* **99**, 041402 (2019).

92. Lin, Z. *et al.* Pressure-induced spin reorientation transition in layered ferromagnetic insulator Cr2Ge2Te6. *Phys Rev Mater* **2**, 051004 (2018).

93. Mondal, S. *et al.* Effect of hydrostatic pressure on ferromagnetism in two-dimensional CrI3. *Phys Rev B* **99**, 180407 (2019).

94. Gopinadhan, K. *et al.* Extremely large magnetoresistance in few-layer graphene/boron–nitride heterostructures. *Nat Commun* **6**, 8337 (2015).

95. Djurdjić-Mijin, S. *et al.* Lattice dynamics and phase transition in CrI3 single crystals. *Phys Rev B* **98**, 104307 (2018).

96. Larson, D. T. & Kaxiras, E. Raman spectrum of CrI3: An abinitio study. *Phys Rev B* **98**, 085406 (2018).

97. Webster, L., Liang, L. & Yan, J.-A. Distinct spin–lattice and spin–phonon interactions in monolayer magnetic CrI 3. *Phys Chem Chem Phys* **20**, 23546–23555 (2018).

98. Žutić, I., Fabian, J. & Sarma, S. D. Spintronics: Fundamentals and applications. *Rev Mod Phys* **76**, 323–410 (2004).

99. Ellsworth, D. *et al.* Photo-spin-voltaic effect. *Nat Phys* **12**, 861–866 (2016).

100. Sun, X. *et al.* A molecular spin-photovoltaic device. *Science* **357**, 677–680 (2017).

101. Endres, B. *et al.* Demonstration of the spin solar cell and spin photodiode effect. *Nat Commun* **4**, 2068 (2013).

102. Dediu, V. A., Hueso, L. E., Bergenti, I. & Taliani, C. Spin routes in organic semiconductors. *Nat Mater* **8**, 707–716 (2009).

103. Liao, K. *et al.* Spintronics of Hybrid Organic–Inorganic Perovskites: Miraculous Basis of Integrated Optoelectronic Devices. *Adv Opt Mater* **7**, 1900350 (2019).

104. Ganichev, S. D. *et al.* Spin-galvanic effect. *Nature* **417**, 153–156 (2002).

105. Ganichev, S. D. & Prettl, W. Spin photocurrents in quantum wells. *J Phys Condens Matter* **15**, R935 (2003).

106. Yuan, H. *et al.* Generation and electric control of spin–valley-coupled circular photogalvanic current in WSe2. *Nat Nanotechnol* **9**, 851–857 (2014).

107. Eginligil, M. *et al.* Dichroic spin–valley photocurrent in monolayer molybdenum disulphide. *Nat Commun* **6**, 7636 (2015).

108. Britnell, L. *et al.* Strong Light-Matter Interactions in Heterostructures of Atomically Thin Films. *Science* **340**, 1311–1314 (2013).

109. Yu, W. J. *et al.* Highly efficient gate-tunable photocurrent generation in vertical heterostructures of layered materials. *Nat Nanotechnol* **8**, 952–958 (2013).

110. Mak, K. F., McGill, K. L., Park, J. & McEuen, P. L. The valley Hall effect in MoS_2 transistors. *Science* **344**, 1489–1492 (2014).

111. Xie, L. & Cui, X. Manipulating spin-polarized photocurrents in 2D transition metal dichalcogenides. *Proc National Acad Sci* **113**, 3746–3750 (2016).

112. Zhang, X.-X. *et al.* Zeeman-Induced Valley-Sensitive Photocurrent in Monolayer MoS2. *Phys Rev Lett* **122**, 127401 (2019).

113. Seyler, K. L. *et al.* Ligand-field helical luminescence in a 2D ferromagnetic insulator. *Nat Phys* **14**, 277–281 (2018).

114. Wu, M., Li, Z., Cao, T. & Louie, S. G. Physical origin of giant excitonic and magneto-optical responses in two-dimensional ferromagnetic insulators. *Nat Commun* **10**, 2371 (2019).

115. Zhang, Y. *et al.* Switchable magnetic bulk photovoltaic effect in the two-dimensional magnet CrI3. *Nat Commun* **10**, 3783 (2019).

116. Song, T. *et al.* Spin Photovoltaic Effect in Magnetic van der Waals Heterostructures. *Arxiv* (2021).

117. Yu, W. J. *et al.* Unusually efficient photocurrent extraction in monolayer van der Waals heterostructure by tunnelling through discretized barriers. *Nat Commun* **7**, 13278 (2016).

118. Jiang, P., Li, L., Liao, Z., Zhao, Y. X. & Zhong, Z. Spin Direction-Controlled Electronic Band Structure in Two-Dimensional Ferromagnetic CrI 3. *Nano Lett* **18**, 3844–3849 (2018).

119. Lado, J. L. & Fernández-Rossier, J. On the origin of magnetic anisotropy in two dimensional CrI3. *2d Mater* **4**, 035002 (2017).

APPENDIX A

Device fabrication

The monolayer/few-layer graphene and 5-40 nm hBN flakes were mechanically exfoliated onto either 285 nm or 90 nm SiO_2/Si substrates and examined by optical and atomic force microscopy under ambient conditions. Only atomically clean and smooth flakes were used for making devices. V/Au (5/50 nm) metal electrodes were deposited onto a 285 nm SiO2/Si substrate using standard electron beam lithography with a bilayer resist (A4 495 and A4 950 poly (methyl methacrylate) (PMMA)) and electron beam evaporation. CrI_3 crystals were exfoliated onto 90 nm SiO_2/Si substrates in an inert gas glovebox with water and oxygen concentration less than 0.1 ppm. The CrI_3 flake thickness was identified by optical contrast with respect to the substrate using the established optical contrast model. The layer assembly was performed in the glovebox using a polymer-based dry transfer technique. The flakes were picked up sequentially: top hBN, top graphene contact, CrI_3, bottom graphene contact, bottom hBN. The resulting stacks were then transferred and released on the pre-patterned electrodes. In the resulting heterostructure, the CrI_3 flake is fully encapsulated on both sides, and the top/bottom graphene flakes are connected to the pre-patterned electrodes. Finally, the polymer was dissolved in chloroform for less than one minute to minimize the sample exposure to ambient conditions. For the pressure study, the SiO_2/Si substrates were diced to approximately 1.7 mm by 1.7 mm to fit into the inner bore of the pressure cell.

APPENDIX B

Electrical measurement

The electrical measurements were performed in a PPMS DynaCool cryostat (Quantum Design, Inc.) with a base temperature of 1.7 K and magnetic field up to 9 T. The CrI_3 devices were mounted in a Horizontal Rotator probe, which allows device rotations around an axis perpendicular to the magnetic field of the longitudinal PPMS magnet. For DC measurement, a bias voltage (V) is applied to the top graphene contact with the bottom one grounded. The resulting tunneling current is amplified and measured by a current preamplifier (DL Instruments; Model 1211).

The measurements at high pressure were performed with a piston pressure cell in a VTI insert cryostat under similar experimental conditions. The hydrostatic pressure was applied using a pressure cell. The device was first glued to a metal stage using epoxy, then Pt wires were affixed to the gold contacts using silver paste. A Teflon cup was filled with the pressure medium (oil) and carefully fitted over the device and onto the stage, such that the device is completely encapsulated in oil. The stage/Teflon cup was then fitted into the inner bore of a piston cylinder cell and a hydraulic press was used to compress the top of the Teflon cup which was held in place by a locking nut. The pressure cell was then loaded into a cryostat for electrical measurement. The in-situ pressure was determined by measuring the fluorescence response of a ruby crystal in the cell through a thin optical fiber at both room and low temperature. Increasing or decreasing pressure requires warming the sample to room temperature and re-loading the cell in the hydraulic press before cooling again.

APPENDIX C

Optical measurement

When a sample is magnetized with an out-of-plane magnetization, the material may exhibit both magnetic circular birefringence (MCB) and magnetic circular dichroism (MCD). MCB induces a phase difference between right-circularly polarized (RCP) and left-circularly polarized (LCP) light, while MCD induces an amplitude difference between RCP and LCP light. When linearly polarized light, an equal superposition of RCP and LCP light, is reflected off the surface of the magnetized material, the phase difference between RCP and LCP light causes a rotation in the linear polarization from the magneto-optical Kerr effect (MOKE), while the amplitude difference between RCP and LCP light induces elliptical polarization from reflective magnetic circular dichroism (RMCD).

The reflective magnetic circular dichroism (RMCD) and Kerr rotation measurements were performed in two similar cryostats (attoDRY 2100 and Quantum Design OptiCool) under the same experimental conditions. A 632.8 nm HeNe laser was used to probe the device at normal incidence with a fixed power of ~1 uW. The AC lock-in measurement technique was used to measure the RMCD and Kerr rotation signal from the atomically thin CrI_3.

For the differential reflectance measurements, we spatially filtered a tungsten halogen lamp and focused the beam to a ~3 μm spot size on the CrI_3. The reflected light was deflected with a beamsplitter and detected by a spectrometer and a liquid-nitrogen-cooled charge-coupled device, which enabled signal measurement from 1.4 eV to 3 eV. To obtain the differential reflectance, we subtracted and normalized the CrI_3 reflectance by the reflectance of the sapphire substrate. The

absorbance of CrI_3 is proportional to the differential reflectance, which can be determined as $\frac{1}{4}(n^2-1)\Delta R/R$.

APPENDIX D

Photocurrent measurement

The photocurrent measurements were performed in a closed-cycle cryostat (attoDRY 2100) at a temperature of 2 K and an out-of-plane magnetic field up to 9 T. A 632.8 nm HeNe laser was focused to a ~1 μm spot size at normal incidence to generate photocurrent. For DC measurement, a bias voltage (V) was applied to the top graphene contact with the bottom contact grounded. The resulting photocurrent was amplified and measured by a current preamplifier (DL Instruments; Model 1211). For AC measurement, a standard lock-in technique was used to measure the change in photocurrent with Stanford Research Systems SR830. For the photon energy dependence measurement, a SolsTiS continuous-wave widely tunable laser was used to generate photocurrent. For the photon helicity dependence measurement, a motorized precision rotation mount was used to rotate an achromatic quarter-wave plate with respect to the linear polarized incident laser beam.

VITA

Tiancheng Song was born and raised in Tianjin, China. He was interested in mathematics, physics, chemistry, and biology in high school, and later decided to study physics. He was very lucky to get admitted to the University of Science and Technology of China in 2012, and earned his bachelor's degree in Physics in 2016. He started his Ph.D. study in experimental condensed matter physics in Prof. Xiaodong Xu’s group at the University of Washington in Seattle in 2016.